UNIVERSITY OF TRENTO - Italy

Doctoral Programme in Physics

Cycle XXIX

Synthesis and Characterization of Nanostructured Materials for Hydrogen Storage Applications

PhD candidate:

Loredana Schiavo

Supervisor:

Prof. Antonio Miotello

Co- Supervisor:

Prof. Luigi Ambrosio

November 2017

Synthesis and Characterization of Nanostructured Materials for Hydrogen Storage Applications

by

Loredana Schiavo

Thesis submitted to the Doctoral Programme in Physics
in partial fulfillment of the requirements for the degree of
Doctor of Philosophy in Physics

Committee members:

Prof. Ines Mancini
University of Trento - Department of Physics, Italy.

Prof. Marta Giamberini
Universitat Rovira i Virgili, Tarragona – Department of Chemical Engineering, Spain.

Prof. Raffaele Giuseppe Agostino
University of Calabria – Department of Physics, Italy.

Loredana Schiavo, "*Synthesis and Characterization of Nanostructured Materials for Hydrogen Storage Applications*".

A mio padre

Alla mia famiglia

Ai miei preziosi nipoti Daniele e Federica

Abstract

"Identifying and building a sustainable energy system are two of the most critical issues for any modern society. Ideally, current energy system, based mostly on fossil fuels, which have limited supply and considerable negative environmental impact, would be replaced with a system based on a renewable fuel. Hydrogen, as an energy carrier primarily derived from water, can address the issues of sustainability, environmental emissions, and energy security. Hydrogen is the most abundant element in the universe, burns clean, producing only water and has the highest energy density per unit mass. This is why hydrogen is considered most suitable to replace fossil fuels as the primary energy material for the mobile industry". [1]

Despite its great potential, the storage of hydrogen at reasonable energy densities poses several technical and economic challenges. Current hydrogen storage systems involve compressed hydrogen gas tanks, liquid hydrogen tanks, cryogenic compressed hydrogen, high-surface-area adsorbents, metal hydrides, and chemical hydrogen storage materials. The main differences between these systems are based on hydrogen storage capabilities, on the security of individual systems and on their costs. In recent years, current research efforts are focused on materials and chemical approaches, where the chemical bonding between hydrogen and other elements increases the volumetric density beyond the liquid state. In particular, new nanostructured materials and composites with high hydrogen storage capacity in a reversible way and lower desorption temperature are necessary. Nanostructured palladium is one of the most investigated as a model system for the comprehension of the atoms and molecules interactions with metal surfaces. However, its low hydrogen storage capability represents a strong limitation in onboard applications. In the last few years, particular attention was given to a group of Mg-based metal hydrides, which present a reversible hydrogen capacity up to 7.6wt%. In this context, air-stable magnesium nanocomposites, providing rapid and high-capacity hydrogen storage without using heavy-metal catalysts, are highly desirable.

In this thesis has been proposed an innovative method for the nanocomposites Mg-based materials preparation, which is based on the thermolysis of an organometallic compound, the bis(η5-cyclopentadienyl)magnesium(II) (Cp_2Mg), previously embedded in a soluble polymer matrix.

[1] Extract from "V.A. Blagojević, D.G. Minić, J.G. Novaković, D.M. Minić, ***Hydrogen Economy: Modern Concepts, Challenges and Perspectives***, in: Hydrog. Energy - Challenges Perspect., 2012: pp. 3–28. doi:10.5772/46098."

In *Chapter 1*, an overview of the "*hydrogen storage technologies",* with a particular attention toward the hydrogen storage systems, is reported. Early hydrogen storage systems based on physical approaches, such as compressed gas (CGH2) and liquid (LH2), have been illustrated. Although these systems are the most mature physical storage technologies, and most prototypes of fuel-cell-powered cars use one of them, the presence of some important problems restricts their use. In particular the safety, due to the explosive mixtures of hydrogen with air, and the costs, to compress or liquefy the gas, represents a limit for their large-scale use. For these reasons the hydrogen storage systems material-based have been introduced. After a brief introduction of the hydrogen-material interactions, the physical and chemical hydrogen interactions with solid matters are explained. In addition, the hydrogen storage capacity of such systems material-based has been reported. The hydriding mechanism details, the hydrogen storage capabilities and the literature state of the art of these systems are supplied. A particular attention is devoted to the nanostructured materials for their special properties, linked to their reduced sizes, which results to be better than of the bulk materials.

Chapter 2 focuses on the nanostructured materials (NSMs), especially on the metallic nanopowders class (MNPs), as amazing candidates for hydrogen storage applications. Starting with a brief description of NSMs synthesis strategies has been subsequently introduced an overview of the common synthetic approaches for the MNP production. These approaches are grouped into physical and chemical approaches. Several synthetic techniques are described, with their potential and disadvantages features. It has been explained how, by using chemical approaches, it is possible to obtain a powerful material with tailored properties for specific advanced technological applications. Among the chemical techniques, it is described the colloidal chemistry, which has been extensively used to synthesize metallic nanoclusters with controlled morphology and narrow size distributions. This control takes place thanks to a good control of the nucleation and growth processes, allowed by using this technique. Finally is described the thermal decomposition process (or thermolysis), a technique widely used in several industrial fields.

Chapter 3 concerns the experimental *synthesis and characterization of palladium clusters by polyol reduction of* $[PdCl_4]^{2-}$ *ions*. A very simple synthetic approach has been proposed. The experimental work is divided into three sections. In the first section is described the study of the chemical reduction process of different palladium salts in EG, without the use

of the surface stabilizer. Many investigations have been performed in order to find a suitable precursor, able to completely dissolve in the polyol liquid before its reduction. Among the different salts, the dissolution and reduction processes of potassium tetrachloropalladate (II) K_2PdCl_4 in the alcohol were resulted to be subsequent and non-concomitant phenomena. For these reasons, this salt has been successively used for the palladium nanoparticle production. In the second section, the chemical reduction of K_2PdCl_4 in the ethylene glycol, in the presence of the surface stabilizers, is performed. In particular, the temperature effects on the palladium nanoparticles formation have been evaluated. Extremely small crystals of about 3nm and equally distributed in the polymer have been obtained. In the last section, a deep investigation of palladium nanocomposites with different ex-situ techniques is reported.

In *Chapter 4*, an innovative method for the *synthesis of nanostructured magnesium composites into a poly(methyl methacrylate) (PMMA) matrix* have been presented. The proposed synthetic approach consists of two consecutive stages. The first concerns the precursor/polymer blend preparation by a "*solvent mediated method*", wherein the starting reagents are mixed in solid state by using of a suitable solvent. The second stage involves the thermal decomposition (or thermolysis) of such precursor-embedded into the polymer blend. The most important problems concerning the use of such magnesium compounds are their high air reactivity (spontaneous ignition) and their oxidation phenomena. For this reason, the reactions involving the magnesium compounds, as the Cp_2Mg precursor, have been performed in the inert atmosphere of gas. Several characterization techniques have been exploited to identify the phase produced. Early results obtained from the spectroscopic characterizations (XPS) have allowed to establish that the magnesium produced in PMMA was almost completely oxidized. The morphological (TEM) and structural (STEM) investigations has revealed the presence of magnesium nanocrystals of about 2nm, completely oxidized.

Chapter 5 concerns the *synthesis and characterization of nanostructured magnesium composites into a polyetherimide (PEI) matrix.* The work essentially done in this chapter concerns the improvement of the synthesis proposed in the previous chapter, by changing the polymeric matrix and the thermolysis process. In particular, a new high-performance amorphous thermoplastic polymer, named polyetherimide (PEI), was been used. The thermal annealing has been carried out in a tubular oven, under nitrogen flow. A careful design of a sample transport device has been carried out, in order to guarantee always an

inert nitrogen atmosphere to the sample. The high thermal stability of the matrix, as well as the more homogeneous and controlled heating treatment, has allowed a better control of the new nanocomposite class preparation. The Mg/PEI nanocomposites spectroscopic characterization (XPS) has shown the presence of a metallic and oxidized magnesium mixture on the nanocomposite surface. Very interesting results are supplied by the high-resolution scanning transmission electron microscopy. In particular, the High Angular Annular Dark Field (HAADF) micrographs shows the presences of aggregates of nanoparticles of about 20 nm, made of smaller nanocrystals of about 5 nm sizes. Simulated diffraction analysis performed on a HAADF micrograph (HAADF-STEM) for the single nanocrystal, has allowed to identify a core-shell structure in which a magnesium metallic core was covered by a layer made of oxygen and others impurities, coming from the solvent used. The presence of a metallic core and an oxide shell indicates that magnesium has passed through the metal formation. However, the magnesium is a reactive metal and probably, during the sample preparation for the analysis, oxidation phenomena occurs. It should also be pointed out that the reduced dimensions of the metal produced, and hence the nanostructuring effects, amplify the interface phenomena and therefore the oxidation. However, several surface oxygen removal processes are known, such as hydrogen fluorination or hydrogenation processes. The future research activity, after the final discussion of the thesis, will be about the removal of oxide layer and, if successful, the hydrogenation/dehydrogenation tests.

Concluding remarks and future perspectives are summarized in the Conclusions chapter. In the two following appendixes, a detailed description of the manipulation of air sensitive compounds (Appendix A) and the advanced characterization techniques employed (Appendix B) are given.

Contents

Chapter 1

Hydrogen storage technologies

1.1. Hydrogen as clean and renewable energy carrier

Hydrogen has been identified as an attractive energy carrier for future systems for both transportation and stationary applications and has the potential to reduce greenhouse emission and pollution that have been plaguing mankind since the beginning of the industrial revolution [1]. Hydrogen has fascinated generations of people for centuries like Jules Verne, that in the novel "The Mysterious Island" of 1874 has wrote [2]:

"I believe that water will one day be employed as fuel, that hydrogen and oxygen which constitute it, used singly or together, will furnish an inexhaustible source of heat and light, of an intensity of which coal is not capable."

As already suggested long time ago by Jules Verne, it is clear that hydrogen is not available on Earth as a primary fuel, most of hydrogen exist as H_2O or bounded to C in liquid or gaseous hydrocarbons [1]. Energy is therefore needed to produce hydrogen. In fact it cannot be classified as renewable sources rather as an energy carrier produced from primary sources as fossil fuels and renewable sources. The hydrogen technology and economy are linked to the production, storage and distribution of H_2 fuel. However, it would already be important to implement any of these part without full-blown solutions for the others [3].

1.2. Hydrogen production

The hydrogen can be produced by separation (decomposition) of chemical compound, by electrolysis from water or by chemical processes from hydrocarbons or other hydrogen carriers [4]. The energy of such processes was initially fossil-based: it was mostly produced from non-renewable sources such as oil, natural gas, and coal [5,6]. Many efforts have been done for a complete and progressive shifts toward renewable sources [7], for example trying to produce hydrogen from thermochemical water splitting, high energy nuclear radiation, plasma and solar photovoltaic-water electrolysis [8–10] . At the same time, many efforts have been done to generate energy for the electrolysis and for the other processes from clean renewable sources such as solar radiation, kinetic energy of wind and water or geothermal heat. The energy-chain and technical challenges for creating a viable hydrogen economy is shown in Figure 1.1 [11]. By using renewable resources such as sunlight to split water, hydrogen may be produced cleanly, and can efficiently be stored in metals and other complex host frameworks for use in fuel cells, which could power many automotive and non-automotive applications, including forklifts, wheelchairs, lawn mowers, bicycles, portable power, laptops, stationary and grid applications. The most effective use for hydrogen is conversion of its chemical energy to electrical energy in fuel cells.

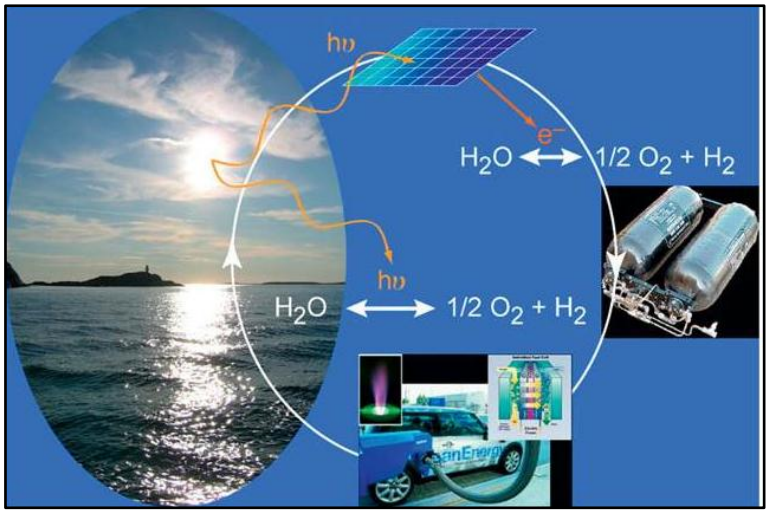

Figure 1.1 The three links of the hydrogen energy chain: production, storage and use in fuel cells

Despite the hydrogen technologies are often associated with vehicle applications in the recent years many research have unveiled a range of new technologies including nickel metal hydride batteries [12], gas separation and purification [13], sensors [14], processing

methods for bulk materials amorphization [15], switchable mirrors [16] and more recently new ionic conductors for batteries [17]. Hydrogen may become an important link between renewable physical energy and chemical energy carriers [4]. For each of these cases, it is very important to choose the hydrogen storage material that must have peculiar characteristics. In the transportation case, for example, a sufficiently high mass and volumetric densities, in a readily accessible state of hydrogen storage systems at reasonably low cost, and with an adequate efficiency, represents a major technological challenge and perhaps the primary barrier to the use of hydrogen as a clean energy carrier. The critical point for the development of all hydrogen technologies is related to the chosen of the appropriate solution for storage systems.

1.3. Hydrogen storage systems

The hydrogen storage constitutes the critical point for the development of the technologies systems H_2-based. The hydrogen energy density is higher than those of the fossil fuels or other non-renewables sources [18]. In Figure 1.2 (taken by https://energy.gov/eere/fuelcells/hydrogen-storage) is shown a scheme of several hydrogen storage technologies. The hydrogen may be stored in physical-based systems as cryogenic liquid (LH2) or compressed gas (CGH2), and in material-based systems as adsorbents materials, organic liquid or hydrides materials (as metals or intermetallic compounds), characteristic for their high gravimetric and volumetric density.

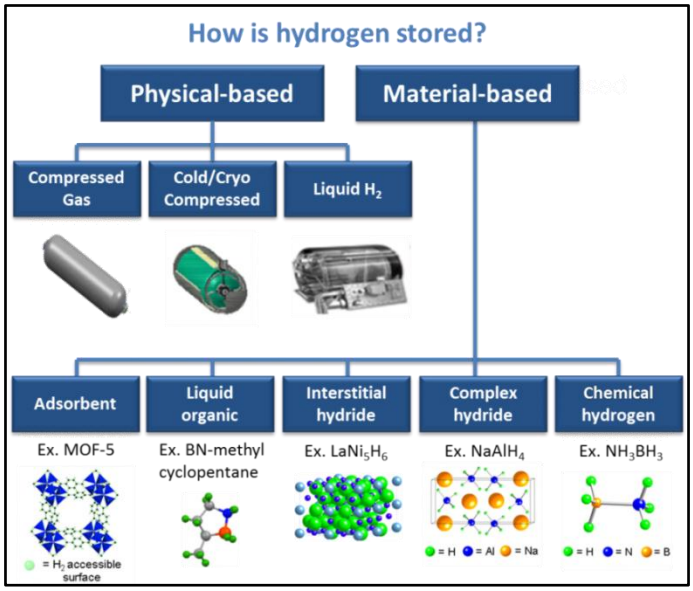

Figure 1.2 Hydrogen technologies

The main differences between these systems are the hydrogen storage capacity, the security of individual systems and their costs. The volumetric hydrogen density on the materials basis is reported in the Figure 1.3 [19]. Several empirical models are developed to estimate the volumetric efficiency of the different systems. It is resulted that the volumetric efficiency of CGH2 and LH2 systems is resulted lower than of the conventional metal hydrides [19]. The maximum amount of hydrogen in the hydride phase is related to the number and size of interstitial sites in the metal host, and to the bonding energy involved. According to the geometrical Westlake criterion, the distance between two hydrogen atoms in the metal interstitial sites [20] is at least 2.1Å. The maximum theoretical hydrogen volumetric density in a metal hydride, assuming a closed packing of the hydrogen, is therefore 254 kg m^{-3}, which is 3.6 times the density of liquid hydrogen [21]. In the metal hydrides the hydrogen is chemically combined with the metal (chemisorptions) to give hydrides [18,22–24]. However, the hydrogen can physically combine with matter (physisorption). The main difference between the physisorption and the chemisorptions is the type of bond.

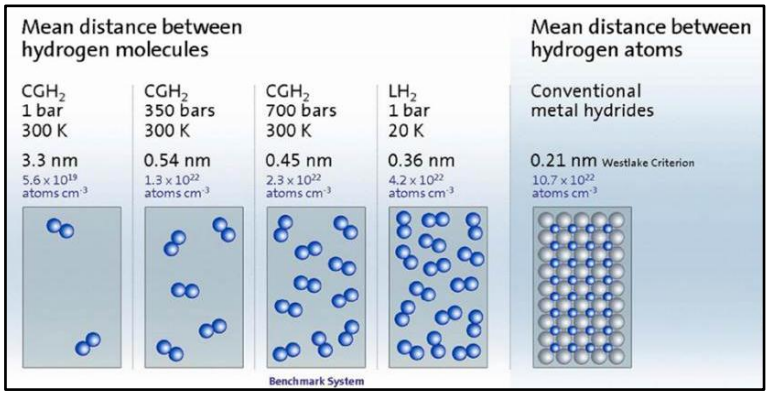

Figure 1.3 Volumetric hydrogen densities on material basis

In the physisorption the hydrogen molecule binds to the adsorbent solid surface (adsorbent materials) with Van der Waals interactions. These weak types of interactions lead, at ambient temperature and pressure, to the formation of hydrogen monolayer on the adsorbent surface. A multi-layer coverage is expected only at lower temperatures and pressure conditions [25]. Since the physisorption is a surface phenomenon, a high surface area is required to obtain a high hydrogen storage capability. In chemisorptions, instead, the H_2 splits into protons, those diffuse into the metal and are adsorbed, forming metal or complex hydrides. Strong bonds are in playing. In the Figure 1.4 a representation of these two adsorbing methods is reported.

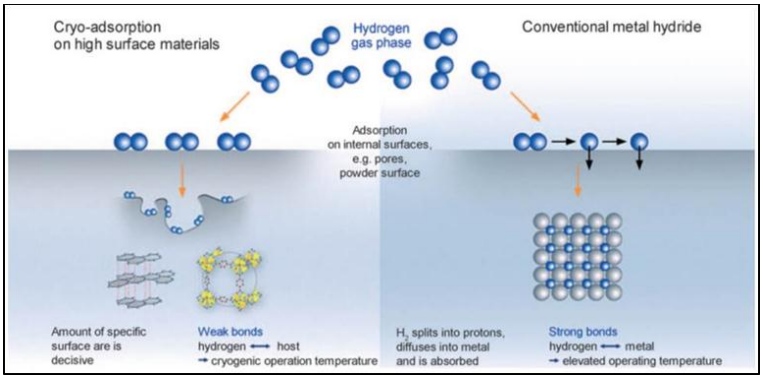

Figure 1.4 Representation of cryo-adsorption and chemical storage in a hydride.

1.3.1. Physical-based storage systems

The hydrogen storage in physical-based systems includes three technologies [22]:

1. compressed gaseous hydrogen (CGH2);
2. liquid hydrogen (LH2), 0.1MPa, about -253°C;
3. cryo-adsorbtion on high surface area materials, 0.2-0.5MPa, about -193°C.

The gas-compression require, at room temperature, high-pressure tanks (35-70MPa) thermally insulated; the storage as a liquid, instead, requires cryogenic temperatures (the boiling point of hydrogen at one atmosphere pressure is −252.8°C) [22,26,27]. Presently available storage options typically require large-volume systems to store the hydrogen, but this is not an issue for stationary applications. Despite these aspects, the CGH2 and LH2 are most mature physical storage technologies and most prototypes of fuel-cell-powered cars use one of these storage systems. In the Figure 1.5 are showed two commercial prototypes of the CGH2 and LH2 systems. These systems, however, present two important drawbacks such as *security*, given by the explosive mixtures of hydrogen with air and *cost*, to compress the gas or liquefy the liquid (are both very expensive). For these reasons recent studies focalized their attention towards solid material-based systems, able of solve both issues (see Figure 1.2).

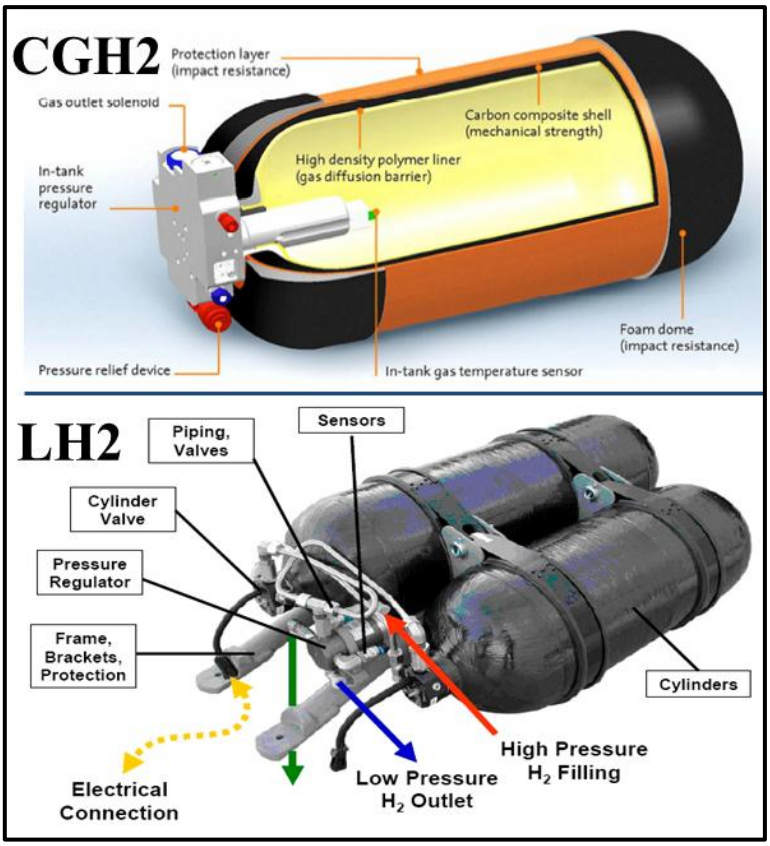

Figure 1.5 Compressed gaseous hydrogen (CGH2) and liquid hydrogen (LH2) vessel

1.3.2. Material-based systems: physically storage

Physisorption is a surface phenomenon, thus a high surface area is required. Molecular hydrogen physisorbs onto a surface through weak Van der Waals interactions. The strength of these interactions is very weak, with an enthalpy of adsorption ΔHa between 4 and 10 KJ/mol. Since the physisorption is an exothermic process and the bonding is very weak, low temperatures, normally at the boiling point of liquid nitrogen (-196,8°C), are necessary to effectively physisorb hydrogen [28]. For this materials the hydrogen adsorbed at solid surfaces depends both on the applied pressure and temperature, and by on the pore structure and pore sizes of the adsorbents materials [18,22,24]. The most studied adsorbing materials can be classified in:

1. **zeolites;**
2. **carbon materials**;
3. **metal organic frameworks (MOFs)**;
4. **polymers of intrinsic porosity (PIMs)**.

The **zeolites** and related compounds are crystalline microporous structures of aluminosilicates. A typical composition of aluminosilicates is Al_2SiO_5, as visible in Figure 1.6. Their microporous framework seemed to be highly suitable for hydrogen storage adsorption.

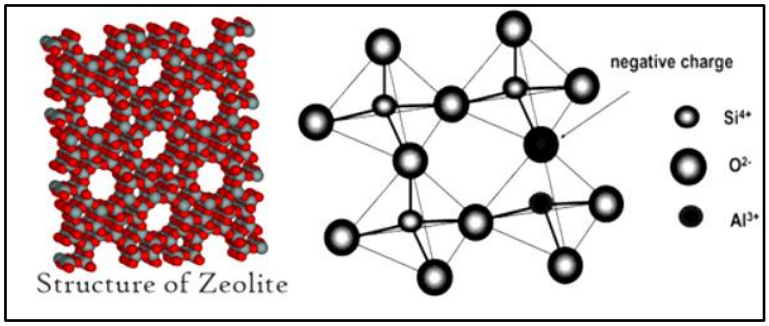

Figure 1.6 Structure of zeolite

However the hydrogen uptake capability may vary from less of 0.1% at STP (standard conditions for temperature and pressure) conditions to 2.86% at 77 K and 15 bar of pressure, and so this materials needs of cryogenic temperature conditions for storing lower hydrogen amounts than of other systems. For this reason they will be not suitable for hydrogen storage in technical applications.

There are numerous studies on the use of different **carbon materials** as media for hydrogen storage. Solid state carbon may exist under different crystalline forms named allotropes. Diamond and graphene are the two well-known allotropes. In Figure 1.7 are represented some of the carbon material systems deeply investigated as carbon nanotubes (CNT), fullerene, graphite and graphene.

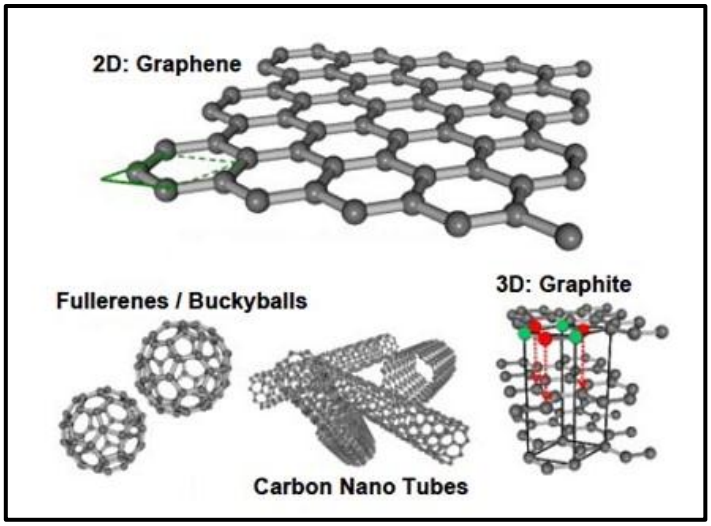

Figure 1.7 Graphene, fullerene, carbon nanotubes and graphite structures

Graphene presents a high hydrogen storage density which can be exploited to store hydrogen. It is found that graphene can be converted in graphane using a steam of hydrogen atoms on its surface, and that the hydrogen stored can be also easily released by heating at 450 °C [23] (see Figure 1.8). Fullerene is formed by a spherical or cylindrical wrapping of graphene sheets. Nanotubes are fullerenes formed by graphene sheets wrapped, as shown in Figure 1.9. The diameter of those tubes can be as small as 1 nm. The porosity of nanotubes is large so the adsorption of various gases including hydrogen is enabled.

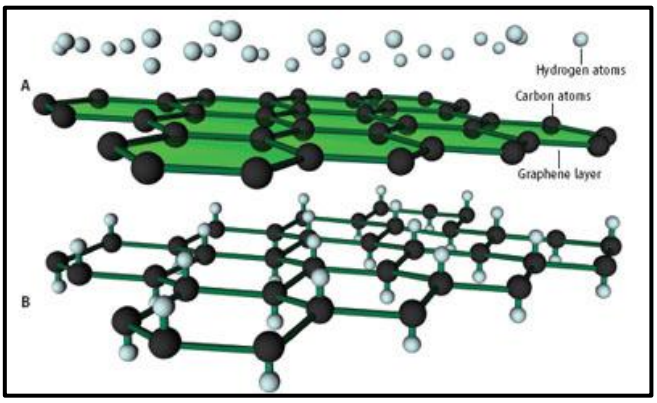

Figure 1.8 Hydrogen addition converting graphene (top) into graphane (bottom)

In the Figure 1.9 are reported a carbon nanotube structures and a simulation of hydrogen-nanotubes interactions as function of the number of shells (Ns), representing the calculated storage density in weight %. The hydrogen condenses as a monolayer at the surface of the nanotube or condenses in the cavity of the tubes. The condensed hydrogen has the same density as liquid hydrogen at –253°C [18].

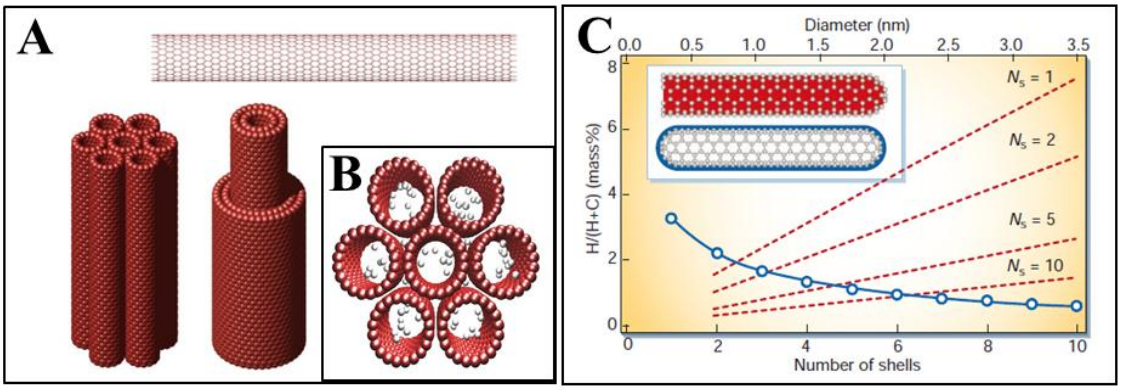

Figure 1.9 Representation of the carbon nanotube structures (A), simulation of the interaction between nanotubes and hydrogen (B) and calculated storage density in mass% as a function of the number of shells Ns (blue) and as a function of the tube diameter (red).

The carbon materials present a low storage capability at STP conditions. Unlike theoretical basic calculations that claim that carbon materials can store up to 6,7 wt% of hydrogen [29,30], it was be found that the hydrogen storage capacity may vary from 5% at 77 K and 20-30 bar of pressure [31] to 8.25% at 80K and 70bar pressure [32]. Many experimental results are reported in the literature and none of the results are consistent with others. This may be due to the variety of procedures available for synthesis of carbon structures. Thus although the reversibility and fast kinetics make these materials attractive options, low hydrogen storage capacity at ambient conditions makes these carbon structures unsuitable for practical application. Another carbon material deeply investigated is the **activated carbon**, which is a carbon-form processed to have small pores and low-volume. This process increases the surface area available for adsorption or chemical reactions. The activated carbon has a high porosity, and has been considered as a potential candidate for hydrogen storage purposes because it is relatively cheap and accessible on a commercial scale. Experimental results show that products with micropore volumes greater than 1mL/g are able to physisorb ca. 2.2 wt% of hydrogen. It is expected that optimizing the adsorbent material properties and the absorption conditions, a storage capacity up to 4.5 to 5.3% can be achieved [23].

The **MOFs** are the youngest class of porous materials and are made of metal ions as vertices that are connected by organic molecules. The most important feature is their exceeding high surface area (5000 m^2g^{-1}). So far the MOFs (MOF-177) have shown the highest hydrogen storage capacity of 7.5 wt% at 77 K [33,34], but these results are strictly pressure-dependent, and are in disagreement in the literature. The MOF-177 molecular structure is reported in Figure 1.10. Furthermore, the sensitivity of the synthesis process, the controlled atmosphere and the necessity of cryogenic temperature make these materials unsuitable for their use as a practical material for hydrogen storage.

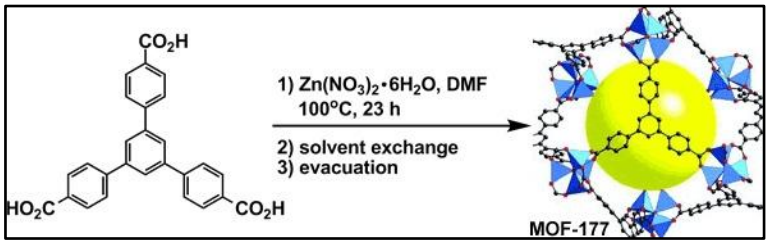

Figure 1.10 Chemical reaction for the MOF-177 production

The polymers with intrinsic microporosity (PIMs) have been also widely studied as potential hydrogen storage materials. The intrinsic microporosity can be defined as a

continuous network of interconnected intermolecular voids, which forms as a direct consequence of the shape and rigidity of the component macromolecules. In Figure 1.11 are reported both the PIM-1 (a tetrazole-containing polymer) chemical structure than its molecular model. PIMs can be prepared either as insoluble networks or soluble polymers. Such materials exhibit analogous behavior of that of the conventional microporous materials, such as activated carbons.

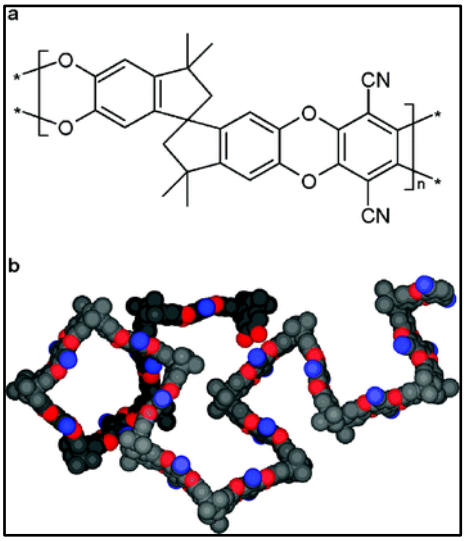

Figure 1.11 (a) Chemical structure of PIM-1. (b) Molecular model of PIM-1 showing its highly contorted, rigid structure.

Although the structure of these polymers seems to be very interesting, such as to make these materials as promising candidates for hydrogen storage materials, their hydrogen storage capability up to 2.7 wt % [35], resulted to be still too low, like that of the other physically storage systems. As the physisorption has the advantages of higher energy efficiency and faster adsorption/desorption cycles than the chemisorption, extensive efforts have been done to find new hydrogen-storage systems as metal nitrides, metal imides, doped polymers, clathrate hydrates, hollow glass microspheres and capillary arrays able to store a large quantities of hydrogen. The absorbing materials previously examined have been shown a low hydrogen storage capability at extreme temperatures and pressures conditions. Many efforts have be done for improving the surface properties, like for example by using the mechanical milling for the nanostructured materials production and the defects creation, or by using the catalysts (as Pd, Pt, etc.) for the adsorption capacity increasing. However, until now, nothing solid physical storage system was found as suitable for hydrogen storage technology.

1.3.3. Material-based systems: chemical storage

The metals can chemically combine with hydrogen atoms through a chemisorptions phenomenon, to give hydrides. The hydrogen molecule comes in contact with the surface and dissociates into two hydrogen atoms that diffuse into the solid. The hydrogen atoms chemically bond with the solid materials, forming hydride. The most studied metals hydrides are shown in Figure 1.4. The metals and intermetallic compound are able to form hydride phase adsorbing reversibly large amounts of hydrogen, in some cases under moderate temperature and pressure conditions, which give them important safety advantages than the gaseous and liquid storage systems. Their inherently high gravimetric and volumetric density make them a very interesting platform for hydrogen storage both for mobile applications and for others various applications (for e.g. stationary power, portable power, laptop, phone,) according with the power requirements [36].

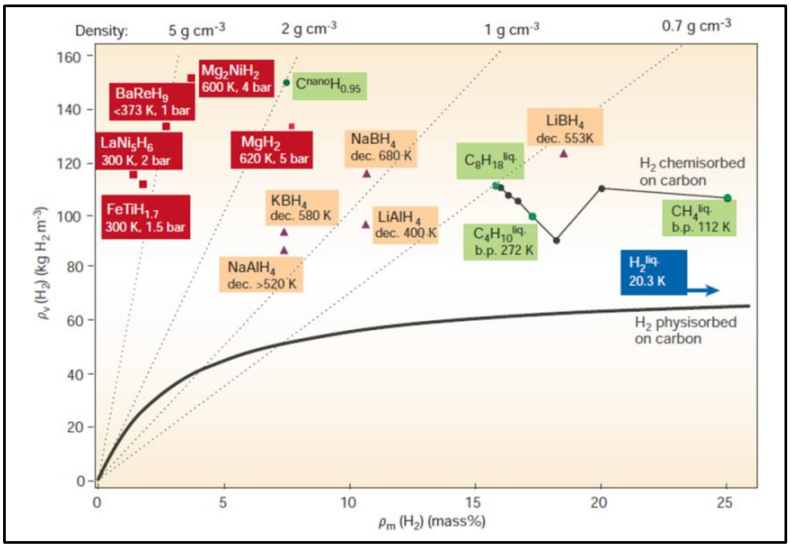

Figure 1.12 Stored hydrogen per mass and per volume. Comparisons between the metal hydrides, petrol and other hydrocarbons.

The hydrogen-storage density of metal hydrides, in fact, is higher (6.5 H atoms/cm^3 for MgH_2) than hydrogen gas (0.99 H atoms/cm^3) or liquid hydrogen (4.2 H atoms/cm^3). The volumetric hydrogen density for different materials is shown in Figure 1.3 [19]. As it is visible in Figure 1.12 the mass density of the intermetallic compounds and alloys vary as a function of pressure and temperature. A low mass density is a general disadvantage of all known metal hydrides working near room temperature. Of course, many intermetallic compounds and alloys are able to form hydrides with up to 9 mass% of hydrogen, such as $Li_3Be_2H_7$, and 4.5 H atoms per metal atom as $BaReH_9$. However the hydrogen desorption

of such hydrides is not reversible within the required range of temperature and pressure [18]. The performance and cost requirements of these storage technologies represent the key for the success of a hydrogen economy.

An optimum solid storage materials-based have to satisfy some requirements:

1. **high hydrogen capacity** per unit mass and unit volume, which determines the amount of available energy;
2. **reversibility** of the release/charge cycle at low temperatures in the range of 30–100°C and moderate pressures in the range of 1 - 10atm;
3. **low heat of formation** in order to minimize the energy necessary for hydrogen release;
4. **low heat dissipation** during the exothermic hydride formation;
5. **limited energy loss** during charge and discharge of hydrogen;
6. **fast release/charge kinetics** with minimum energy barriers to hydrogen release and charge;
7. **high stability against O_2** and moisture for long cycle life;
8. **unchanged characteristics** of properties after release/charge cycles of the gas;
9. **limited costs**.

Several metal hydrides are studied and their hydrogen storage properties investigated. An exhaustive database containing all the information about metal hydrides and intermetallic compounds is available on website *http://www.sandia.gov/news/publications/annual_report/* [37]. The most commonly hydrides studied can be classified into three classes:

1. **Metal hydrides**
2. **Intermetallic compounds**
3. **Complex hydrides**

The metal hydrides can be defined as hydrides of elementary metals; the intermetallic compounds are typically formed by alloying two metallic components, (A) and (B) in which (A) is a metal that can easily form stable hydrides, and (B) is another element which does not form stable hydrides. The components A and B can generally be fully or partially substituted by other elements of relatively similar size or chemistry. The intermetallics thus formed could then be grouped according to their stoichiometry such as AB_5, AB_2, AB and

others [38]. In the metal hydrides, alloys and intermetallic compounds the interstitial lattice sites are occupied by hydrogen atoms, while in the complex hydrides of metals or metal–nonmetal compounds, the hydrogen is covalently bound to the a metal (or, in the case of boron, a non-metal) atom to form complex anion.

1.4. Hydrate forming mechanism

1.4.1. Hydrogen interaction with metals

As previously reported the hydrogen interaction with metals can be classified into three processes: a) physisorption, b) chemisorption and c) quasi-molecular interaction (well known as Kubas interaction). A schematic representation of the energies involved in each process is reported in Figure 1.13. The physisorption was previously discussed.

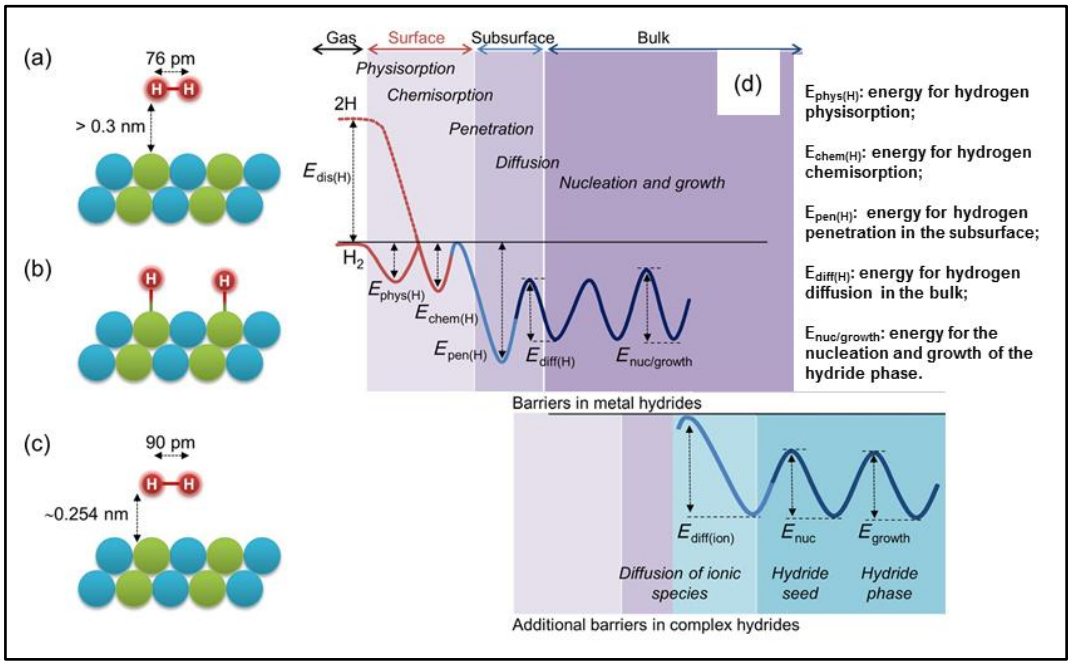

Figure 1.13 Schematic illustration of physisorbed (a), chemisorbed (b) and weakly bonded hydrogen (c), and postulated energy barriers for the hydrogenation of metal complex hydrides (d). In complex hydrides, additional barriers due to intrinsic mass transport also need to overcome.

The chemisorption is a stronger perturbation of the molecular electronic structure with formation of chemical bonds with the substrate. The energies are typically of several eV. (Figure 1.13, b). In chemisorption the hydrogen molecule dissociates into individual atoms that spread into the material and then bind with it. This hydride bonding is quite strong,

with an enthalpy of formation (ΔH_f) of 100–200 kJ/mol$_{H2}$ and a binding energy in the range of 2–4eV [28]. The mechanism of hydrogen ab(de)sorption process has to go through a range of activation barriers (Figure 1.13, d), and it occurs only when the energy supplied is higher than the activation energy barrier ($E_{chem(H)}$). Far from the metal surface, the potential of a hydrogen molecule and of two hydrogen atoms are separated by the dissociation energy ($H_2 \rightarrow 2H$, E_D = 435.99 kJ mol^{-1}). The first attractive interaction of the hydrogen molecule approaching the metal surface is the Van der Waals force leading to the physisorbed state ($E_{phys(H)} \approx 10$ kJ·mol^{-1}) approximately one hydrogen molecule radius (≈ 0.2 nm) from the metal surface. Closer to the surface, the hydrogen has to overcome an activation barrier for dissociation and formation of the hydrogen metal bond. The molecular dissociation will only occur when the energy supplied (depending on the temperature and pressure in the system) is higher than the activation energy barrier ($E_{chem(H)}$). The height of the activation barrier depends on the surface elements involved. Then bonding takes place by electron sharing between dissociated hydrogen atoms and metal atoms on the host surface. At the same time, hydrogen atoms begin to penetrate the subsurface of the host material ($E_{pen(H)}$). These atoms can populate the interstitial sites of the host material through surface diffusion ($E_{diff(H)}$). As a consequence, a stable metallic hydride phase is formed, if the hydrogen concentration is very high. When considering complex hydrides, the hydrogen (ab)desorption process will also depend upon ionic diffusion, and the subsequent growth of the hydride phase through the reaction of various ionic species with hydrogen, and thus, additional activation barriers have to be considered ($E_{diff(ion)}$, E_{nuc}, and E_{growth}). Desorption of hydrogen mainly occurs though the reverse process by breaking hydrogen bonds, either weak van der Waals or strong chemical bonds.

1.4.2. Thermodynamic and kinetics aspects

The gravimetric and volumetric storage capabilities are the most important parameters to determine the potential of materials as hydrogen storage system. These parameters are strictly dependent from the physical conditions in which a material adsorb/desorb the hydrogen (see Figure 1.12), but also by the physical properties of the material. The surface area, the pore structure and volume, the particle size, the atomic structure and chemical factors, such as the affinity for hydrogen, the surface reactivity and bond strength determine the thermodynamics and kinetics of ab(de)sorption. Since the chemisorption follows the physisorption, all the prerequisite for material-based systems that physically stored are required. In chemisorption, strong chemical bonds are involved, and therefore,

high temperatures are required to break these bonds and release hydrogen. The thermodynamic aspects of hydride formation from gaseous hydrogen are described by pressure-composition isotherms (PCI) (Figure 1.14). The ideal PCI plot shows that hydrogen uptake increases with increasing pressure to form a solid solution of hydrogen in the metal (α phase), but at the equilibrium plateau pressure (Peq) the metal starts to "lock" hydrogen within its structure and form a hydride (β phase). If the applied pressure is below the plateau, the stored hydrogen is released, because it is kinetically favorable. The plateau-length determines the amounts of hydrogen stored. In the pure β-phase, the hydrogen pressure rises with the concentration. The two-phase region ends in a critical point T_C, above which the transition from the α- to β-phase is continuous.

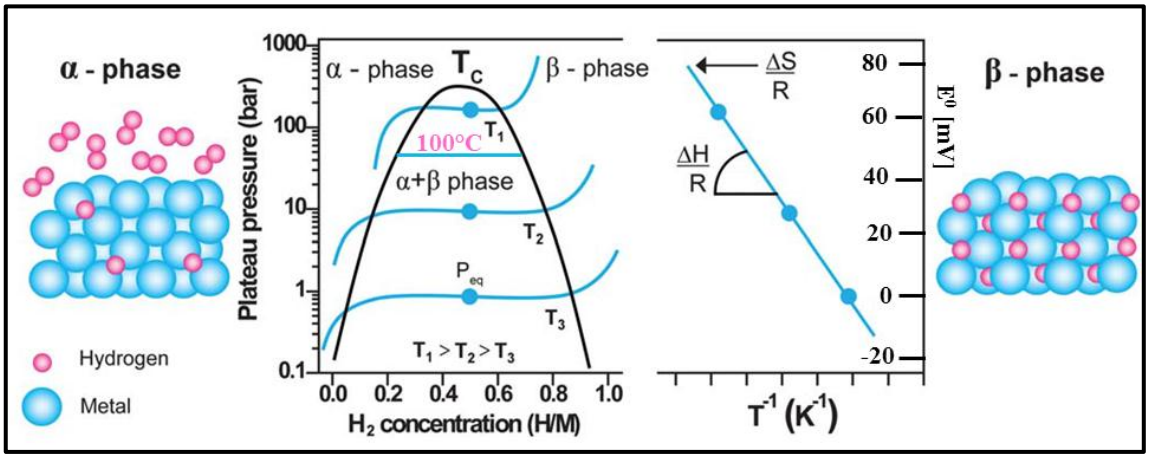

Figure 1.14 PCI plot of hydrogen metal-systems on the left hand side. The construction of the Van't Hoff plot is shown on the right hand side. The slope of the line is equal to the enthalpy of formation divided by the gas constant and the intercept is equal to the entropy of formation divided by the gas constant. 2D-illustration of hydrogen adsorption.

The equilibrium pressure, P_{eq}, is related to the changes ΔH and ΔS in enthalpy and entropy respectively, as a function of temperature by the Van't Hoff equation:

$$ln\frac{Peq}{PH2} = \frac{\Delta H°}{RT} - \frac{\Delta S°}{R} \quad (1)$$

To decompose a hydride, the temperature has to be increased to a level at which P_{eq} is higher than the system pressure. As the entropy change corresponds mostly to the change from molecular hydrogen gas to dissolved solid hydrogen, it is approximately the standard entropy of hydrogen (S_0 = 130 $J \cdot K^{-1}mol^{-1}$) and it is, therefore, $\Delta S_f \approx$ -130 $J \cdot K^{-1}mol^{-1}{}_{H2}$ for all metal-hydrogen systems [26]. The enthalpy term characterizes the stability of the metal

hydrogen bond. To reach an equilibrium pressure of 1 bar at 300 K, ΔH should amount to 39.2kJ $mol^{-1}H_2$. The hydrogen absorption (hydrides formation) is an exothermal reaction that leads to a notable heat evolution; the same heat has to be provided to the metal hydride to desorb the hydrogen (endothermal reaction for the decomposition of hydrides). The gas–solid equilibrium given by the Van't Hoff equation is the basis for designing a hydride storage system [39]. The Van't Hoff plot for an array of metal hydrides, as shown in Figure 1.15, allows researchers to identify a design specific material [40].

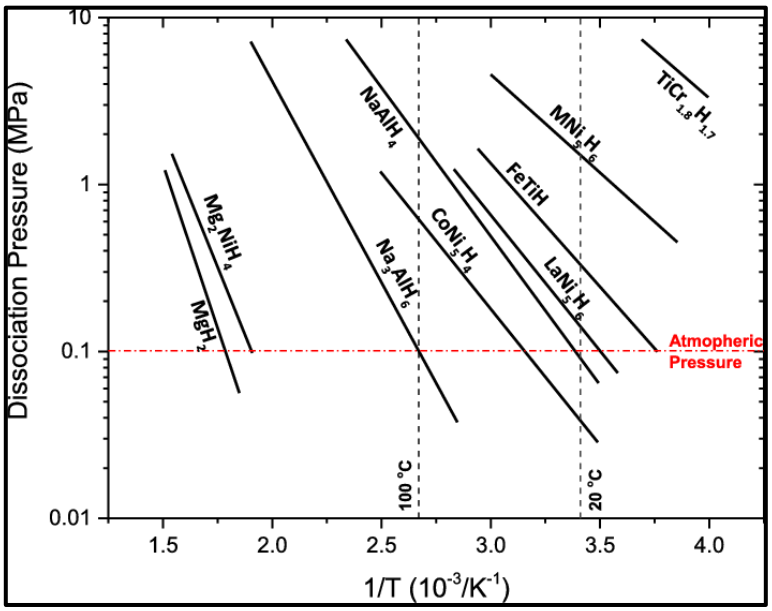

Figure 1.15 Van't Hoff's plot for different metal hydrides

The selection of the storage material is governed by the applicable operating temperature and pressure ranges for a desired application. For example the LaNi5, FeTi and NaAl alloys falls in a window of temperatures ranging from 20°C to 100°C, and of pressure above atmospheric pressure. The operating temperature for MgH_2 and its complex hydrides, at the same pressure condition, follow in higher temperature windows. The dehydrogenation temperature can be as high as 280°C in the case of MgH_2. Hence, Van't Hoff plot plays a vital role in the design of metal hydride integrated devices. Other important properties which govern the choice of materials are the reaction kinetics and cyclic stability of hydrides. The challenge is to find a material able to satisfy the storage cycle. A scheme of storage cycle is shown in Figure 1.16.

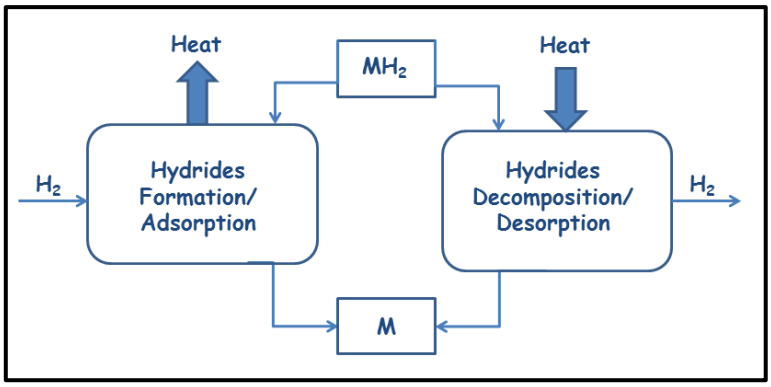

Figure 1.16 Storage cycle for hydrogen storage by formation of metal hydrides

1.5. Metal Hydrides

1.5.1. Electronic structure and hydriding energy

The metal hydrides are hydrides of elementary metals, alloys and intermetallic compounds in which the interstitial lattice sites are occupied by hydrogen atoms. The hydrogen and dihydrogen bonds in the formation reactions of metal hydride constitute a crucial point to the development of the hydrides technology. The metal hydrides reactions usually take place at elevated temperatures and get involving hydrogen and many transition metals and their alloys [26]. The hydriding energy supply important information about the materials tendency to form hydrides. The early transition metals are found to have a strong tendency for hydride formation which decreases as one goes to the right in the transition-metal series. The hydriding **energy** is based on three contributions: the first is given to the energy needed to convert the crystal structure of the metal to the structure formed by the metal ions in the hydride. In general, metals are crystallized in one of the following structures in near ambient conditions (Figure 1.17):

- Body Centred Cubic (BCC)
- Face Centred Cubic (FCC)
- Hexagonal Closed Packed (HCP)

The most common crystal system found for metal hydrides is "face-centered cubic" (*fcc*), except for some metals as V or Cr that generally prefer a strong “body-centered cubic” (*bcc*). It is clear in this case a significant lowers of the driving force for hydride formation. A second contribution, which for some materials is dominant, is the loss of cohesive energy when the metal structure is expanded to form the hydride. This expansion lowers

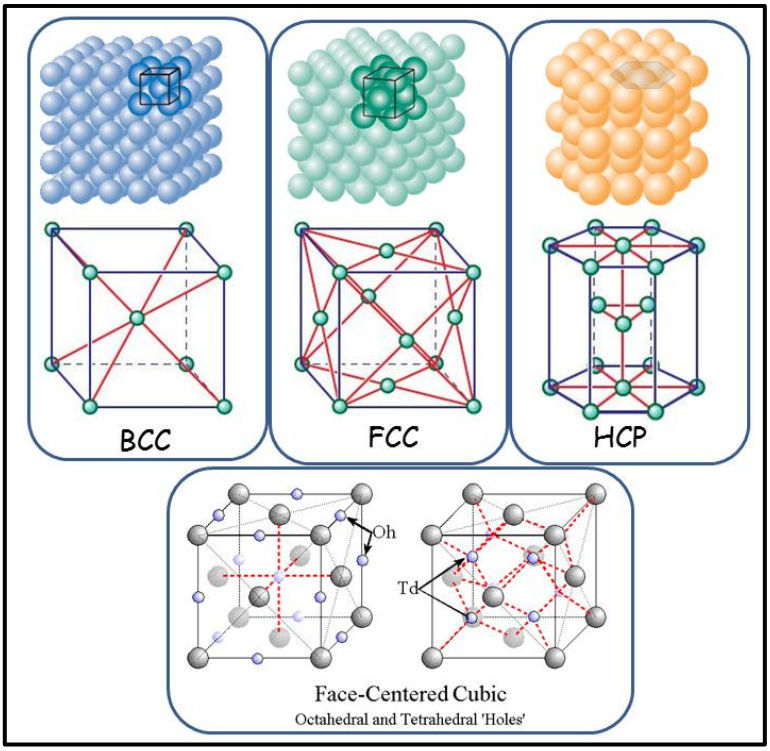

Figure 1.17 Schematic representation of common metallic crystal structure: body center cubic (BCC), faced centred cubic (FCC), hexagonal closed packed (HCP) and interstitial octahedral (Oh) and tetrahedral (Td) site in FCC crystal structure

the cohesive energy of the metal and is a significant impediment to form stable hydrides for the middle to late transition metals, as they have high cohesive energies. The final contribution to the hydride formation energy is the chemical bonding between the hydrogen and metal host [41]. The hydride stability is linked to electronic structure of metal hydrides. It is showed that hydrogen not only contributes electrons to the system, but also states below the bottom of the metal *d*-band. It has been demonstrated, by using the electronic structure calculations, the stability of the monohydrides by the hybridization of the H 1*s* state with the *s* and *p* states of the metal, with no particular role for the metal *d* states. The two hydrogen atoms of the dihydrides, instead, with two atoms per unit cell, would form both their bonding and antibonding band below the bottom of the *d* band. Hence, by contributing states below the Fermi level, the electrons of the host can lower their energy by transferring to these new levels. As the hydride contracts, the antibonding band moves up. It was suggested that when this band moves above the top of the *d* band the dihydride is not stable anymore. This has been used to explain why hydrides with small lattice parameter, such as PdH_2, are not stable as dihydrides. The first metallic hydride discovered in 1866 was right the PdH_2, that can be considered as the first hydrogen storage

material. Under a hydrogen atmosphere, however, the palladium metal converts into the thermodynamically stable $PdH_{0.7}$ (β-phase) with an increasing in the lattice volume of 3.5% at 25 °C with 1.0atm H_2. The maximum palladium hydrogen-to-metal ratio at STP conditions is of about 0.7 [42], due to its solubility in that temperature and pressure conditions [43]. For this reason the metallic hydrides exist with a variety of M:H compositions, typically in fractional concentrations, in contrast to both ionic and covalent hydrides, which have fixed M:H compositions. Hydrogen is dissolved in the metal and the structural symmetry of the metal is often preserved in the hydride phase; however, the unit cell volume may increase considerably, in some cases >20% [44]. The metals may be hydride by direct dissociative chemisorption and electrochemical water splitting. These reaction equations are:

$$M + \frac{x}{2} H_2 \leftrightarrow MH_X \quad (2)$$

$$M + \frac{X}{2} H20 + \frac{X}{2} e^- \leftrightarrow MH_X + \frac{X}{2} OH^- \quad (3)$$

where M represents the metal. The hydrogen atoms are fitting into octahedral or tetrahedral holes in the metal lattice, or in a combination of the two. The stability of a hydride depends on its formation energy through the reaction (2).The hydriding energy is a measure of the H_2 chemical potential in equilibrium with the metal and hydride [41]. The study hydride stability across the periodic table allows to confirm that the metallic bonds are mainly observed for the early d-block and f-block metals. All the alkali metals form a monohydrides with the rocksalt structure. The platinum (Pt) and the ruthenium (Ru) are able to adsorb large quantities of hydrogen, which becomes activated. These two elements, together with palladium (Pd) and nickel (Ni) are extremely good hydrogenation catalysts, although they do not form hydrides.

1.5.2. Hydrides capability

The amount of hydrogen stored in the different metal hydrides, complex hydrides and intermetallic compound are briefly discussed. In classical metal hydrides the hydrogen uptake is limited to roughly 2 wt%, which is due to the fact that most of the typical metal hydrides are intermetallic transition metal compounds in which the hydrogen atoms can be stored per metal atoms. The different families of intermetallic compounds can be classified on the basis of their crystal structures, such as AB_2 type (Laves phase), AB_5 type phases

and Ti-based body centered cubic (*bbc*) alloys [45]. Below are shortly listed the hydrogen capability for the most studied metal hydrides:

1) **magnesium hydride (MgH_2)** is a classical metal hydride and most widely studied material as it combines a high H_2 storage capacity of 7.6 wt%, with the benefit of the low cost of the abundantly available magnesium [46–49] with good adsorption/desorption reversibility. Although MgH_2 has high hydrogen storage capacity, an high decomposition temperature of 300℃ at 1bar of pressure and poor sorption and desorption kinetics are main drawbacks of this material [45];
2) **lanthanum-nickel alloy** (**$LaNi_5$**) is another popular material widely studied. Compared to MgH_2, this intermetallic compound shows better hydrogen storage characteristics in terms of kinetics and temperature requirements. But the amount of hydrogen stored is significantly low. At moderate temperature the hydrogen storage capacity of $LaNi_5$ does not exceed 1.4 wt%.
3) hydrogen storage properties of **FeTi** have been extensively studied too. FeTi is a well-known hydrogen storage compound with a total hydrogen storage capacity of around 1.90 wt%. In addition both Fe and Ti are inexpensive elements. Hydrogen capacity of FeTi can reach over to 1.90 wt% by addition of 1 wt% Pd as a catalyst.

Another class of hydrogen storage materials is that of the complex hydrides. In contrast to the classical metal hydrides, in which interstitial sites are occupied with hydrogen atoms, in complex metal hydrides, hydrogen is covalently bound to a metal (or, as in the case of boron, a non-metal) atom to form a complex anion. The best known are:

1) the sodium alanates hydrides of aluminum as thetetrahydroaluminate–**$NaAlH_4$** and trisodium hexahydroaluminate–**Na_3AlH_6**. Theoretically, $NaAlH_4$ and Na_3AlH_6 contain large amounts of hydrogen, 7.4 and 5.9 wt%, respectively. The weight percent of hydrogen stored in solid compounds as $NaAlH_4$ result more than twice then of the $LaNi_5H_6$ (1.6 wt%). However, the release of hydrogen does not occur in a single-step reaction, so the reversibility of these two reactions is a critical factor for the practical applications;
2) the boron hydrides as **$LiBH_4$** and the **$NaBH_4$.** Although the $LiBH_4$ hydrogen density is theoretically of 18 wt%, its synthesis requires high temperature and expensive compounds. However the boron hydrides suffer of the disadvantage that can form some possible decomposition products as volatile boranes. Even if these

boranes are only formed at trace levels, their formation could lead to substantial loss of storage capacity over many cycles and to damage to the fuel cell;

3) other complex hydrides with high hydrogen capacities are some alkaline earth compounds as **$Mg(AlH_4)_2$** and **$Ca(AlH_4)_2$**, containing respectively 9.3 wt% and 7.9 wt%. The biggest disadvantage of these magnesium and calcium hydrides complexes is that both alanates do not react reversibly under technologically relevant conditions [50,51].
4) also **the amine–borane adducts** as ammonia–borane BH_3NH_3 or ammonia triborane $NH_3B_3H_7$ can be reach a hydrogen content of 19.6 wt% and 17.8 wt% H_2, respectively [22]. The hydrogen contents in ammonia–borane can be partially delivered at temperatures of about 130°C in a multisteps decomposition process, that are exothermic steps unuseful for reversible on-board hydrogen storage. Instead the main disadvantages for the triborane are linked of the possible breakthrough of ammonia which require additional safety precautions for regenerations of borates and gas clean-up, which are expensive process.

1.6. Improvement on hydrides properties: state of the art

1.6.1. Improvements of the surface properties

A critical factor for hydrogen absorption by metals is the metal surface, which activates dissociation of hydrogen molecules in hydrogen atoms that can easy diffuse into the metal host. Most of the known metal hydrides exhibit unsatisfactory charge/discharge kinetics. Different factors can improve the hydrogenation properties, as the **use of catalysts** (like Pd), that promotes the molecular hydrogen dissociation by spillover mechanism of hydrogen absorption (see Figure 1.18) [52]. This mechanism includes adsorption and subsequent dissociation of hydrogen molecule on surface catalyst, and migration and subsequent diffusion of adsorbed hydrogen atoms from the catalyst surface into the metal. Thanks to the spillover the diffusion process of hydrogen atoms inside the metals is enhanced. The induced lattice defects, also, may aid the diffusion of hydrogen in materials by providing many sites with low activation energy of diffusion [43]. The induced microstrain assists diffusion by reducing the hysteresis of hydrogen absorption and desorption.

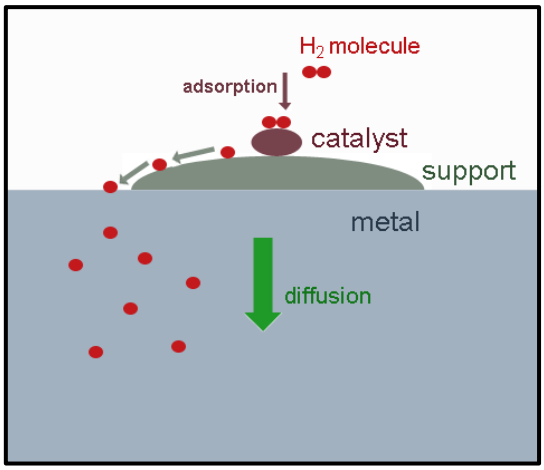

Figure 1.18 Illustration of spillover mechanism of absorption of hydrogen into a metal using a catalyst

In the Figure 1.19 is reported a scheme of defects in a nano-scaled film and their H-solubility in the low concentration range. Besides the conventional H-solubility in the lattice matrix (a) the surface acts as H-trap with its surface (b) and sub-surface (c) sites. At the edge of dislocation (e), often present to account for the mismatch between film and substrate, a cylindrical H-segregation volume is expected. Also grain boundaries (d) solve hydrogen differently to the matrix. The local concentration at a grain boundary is expected that of the solid solution and the hydride-phase.

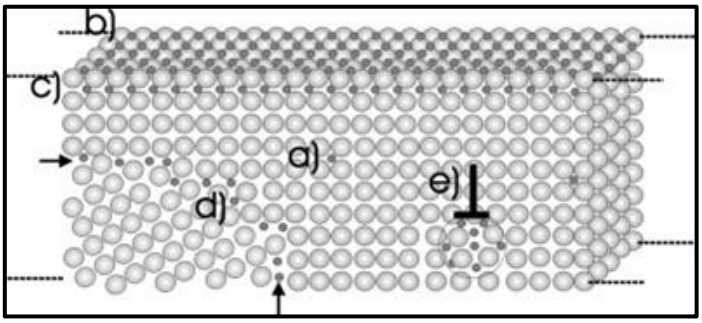

Figure 1.19 Scheme of defects in a nanoscaled film and their H-solubility in the low concentration range.

Recently the nanostructured materials research is widely increased cause their unique properties. The hydrogen solubility in nano-sized metals is better than to the corresponding bulk materials, thanks to their great surface area that provides an high hydrogen absorption [53,54]. The production of nano-sized materials with better powders morphology, gives remarkable improvement on the kinetics and surface activity for hydrogenation.

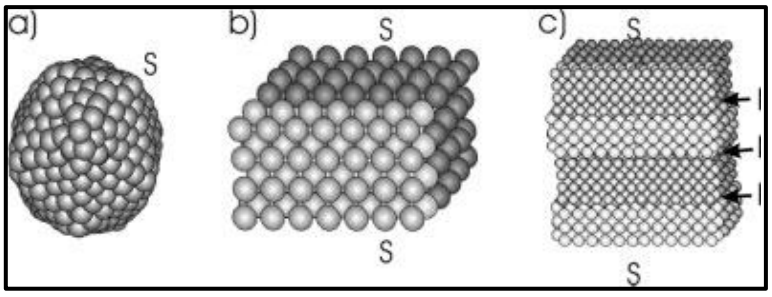

Figure 1.20 Nano-sized metal systems often appear as a) clusters, b) as thin films or c) as multi-layers stacked films with a high amount of surface (S) and interface volume (I)

Nano-sized metal systems are mostly found in the shape of thin films, rods or clusters. Also stacking of nano-sized systems in so-called multi-layers causes interesting sample morphologies with a high density of interface volume (Figure 1.20). Mechanical milling result a simple technique to obtain nanostructured materials. The ball milling, termed mechanical alloying, is a process in which a powder mixture placed in the ball mill is subjected to high-energy collision from the balls allowing to obtain fine powders with uniform dispersion usually of oxide particles. The main effects of ball-milling are increased surface area, formation of micro/nanostructures and creation of defects on the surface and in the interior of the material. The ball milling technique has been widely used for the preparation of nanostructured materials. Typically small amounts of catalysts are added for surface activation enhancements and hence for hydrogenation. In order to avoid the formation of a surface layer of oxygen (especially for some metals air-sensitive, as Mg), the ball-milling of alloys was performed under inert atmosphere. The presence of oxidized layer on the surface represents the most important disadvantage for the use of this technique. In order to avoid the oxidation phenomena the solid material is hydrogenated during milling. It was shown that this approach allow the simultaneous hydrogen uptake also during the mechanical deformation resulting from ball-milling. This technique is the most commonly used for metal-hydrides production, as it is a simple an inexpensive technique. An interesting surface treatment is based on fluorination of metal surface, which both removes the existing oxide layer as a result of a chemical reaction, and also prohibits further oxidation by formation of a special catalytic structure on the surface. The fluorination method involves treatment of the hydride with an aqueous solution of F^-, resulting in much better activity for hydrogenation and easier activation [18,55,56].

1.7. Magnesium hydride materials

1.7.1. Preparation method by physical-approach

A group of Mg-based hydrides stand as promising candidate for competitive hydrogen storage with reversible hydrogen capacity up to 7.6 wt% for on-board applications [57,58]. Efforts have been devoted to these materials to decrease their desorption temperature, enhance the kinetics and cycle life. As previously reported the kinetics and thermodynamic parameters can be improved both by adding an appropriate catalyst into the solid-system material and by using ball-milling method to improve surface properties [59]. In the Figure 1.21 a mechano-chmemical milling effects on commercial MgH_2 prepared in the presence of a nanocatalyst as a dopant is reported [53]. The combined effects of the ball-milling and the use of nanocatalyst-doped material produce improvements both on kinetics (increasing surface area and introducing defects) and also on thermodynamics.

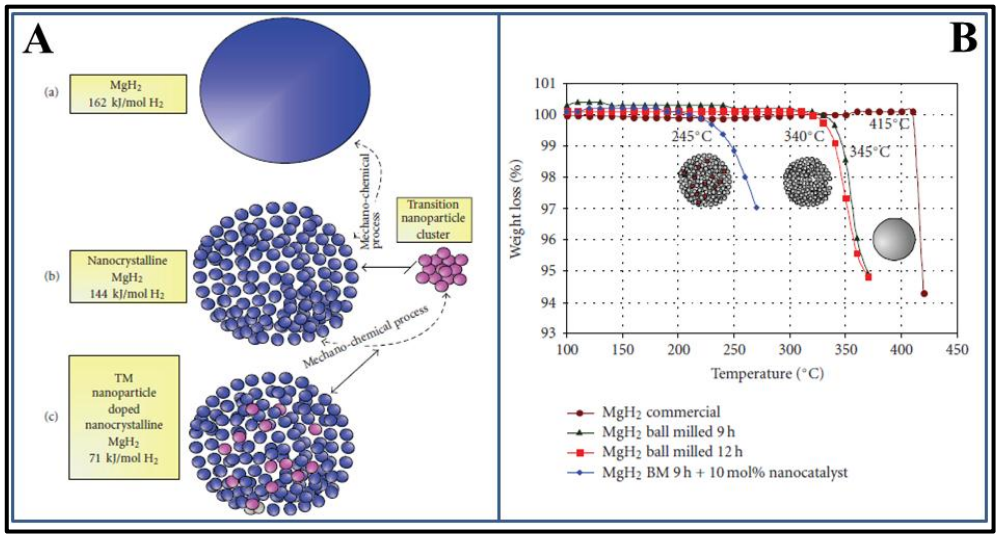

Figure 1.21 (A) Conceptual model of MgH_2 particle (a), nanocrystalline (b) and nanocatalyst-doped materials. (B) TGA curves for the commercial (a), micro/nanocrystalline (b) and 10%mol nanocatalyst-doped nanocrystalline MgH_2.

As it is visible in Figure 1.21, the obtained micro/nanocrystalline MgH_2 grains show endothermic hydrogen decomposition at a lower of temperature of 340°C than to the commercial MgH_2 (e.g., 415°C). In addition to the nanoscale formation, the doping caused by using a nanocatalyst certainly decreases the onset transition temperature by as much as 100°C. Although these studies have yielded promising results, the main disadvantage in

using this mechanical alloy process for Mg-based hydride materials is related to the formation of oxidized layer on the magnesium surface, which inhibits hydrogenation.

1.7.2. Preparation method by chemical-approach

Recently, an air-stable composite material that consists of metallic Mg nanocrystals in a gas-selective polymer, poly(methyl methacrylate) (PMMA) is developed (Figure 1.22) [53,60–62]. The use of polymer matrix, as PMMA, offers different advantages: first of all it is used as surface capping agent and stabilizing ligand, which gives the possibility to obtain a tailored material by modifying the precursor/polymer concentration and the synthesis parameters (as temperature and pressure). Different nucleation process occurs varying these parameters, and crystals of different sizes can be obtained. In addition, the use of a gas-selective polymer allows to mitigate the oxygen and the humidity diffusion inside the polymer matrix and so towards nano-crystals embedded in it, and enhances the hydrogen permeability.

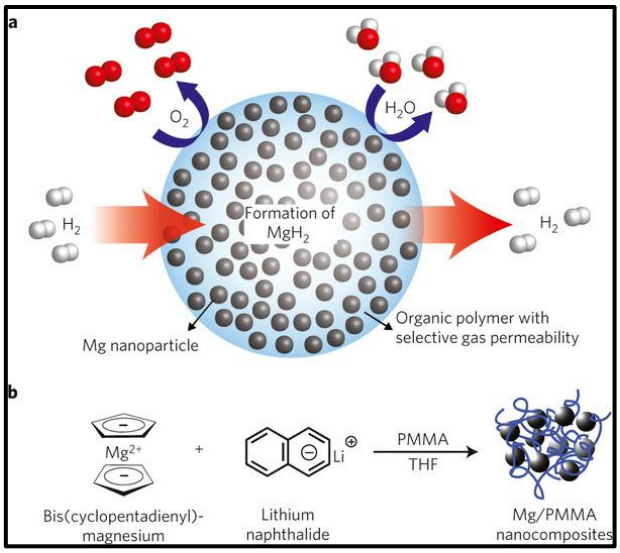

Figure 1.22 Mg NCs in a gas-barrier polymer matrix. Schematic of hydrogen storage composite material: high-capacity Mg NCs are encapsulated by a selectively gas-permeable polymer (a). Synthetic approach for the Mg NCs/PMMA nanocomposites formations (b).

Finally the PMMA makes the composite material more flexible to withstand the volume expansion during phase transition between Mg and MgH_2. Impressively, the Mg/PMMA nanocomposites show stability after two weeks of air exposure. The novel nanocomposites enable hydrogen storage with both high density (up to 6 wt% of Mg, 4 wt% for the composite) and rapid kinetics (uptake <30 min at 200°C) without using heavy metal

catalysts. The remarkable uptake capacity and kinetics can be sustained for a few adsorptions and desorption cycles, with only slightly decrease of dehydrating rate. This interesting polymer-based nanocomposite material certainly deserves further attention, such as investigating the optimization of Mg loading and the polymer/metal nanocrystal interfacial properties.

1.8. References

[1] J. Baxter, Z. Bian, G. Chen, D. Danielson, M.S. Dresselhaus, A.G. Fedorov, T.S. Fisher, C.W. Jones, E. Maginn, U. Kortshagen, A. Manthiram, A. Nozik, D.R. Rolison, T. Sands, L. Shi, D. Sholl, Y. Wu, Nanoscale design to enable the revolution in renewable energy, Energy Environ. Sci. 2 (2009) 559. doi:10.1039/b821698c.

[2] A.W.C. van den Berg, C.O. Areán, Materials for hydrogenstorage: current research trends and perspectives, Chem. Commun. (2008) 668–681. doi:10.1039/B712576N.

[3] G.W. Crabtree, M.S. Dresselhaus, The Hydrogen Fuel Alternative, MRS Bull. 33 (2008) 421–428. doi:10.1557/mrs2008.84.

[4] N.L. Panwar, S.C. Kaushik, S. Kothari, Role of renewable energy sources in environmental protection: A review, Renew. Sustain. Energy Rev. 15 (2011) 1513–1524. doi:10.1016/j.rser.2010.11.037.

[5] M. Steinberg, H.C. Cheng, Modern and prospective technologies for hydrogen production from fossil fuels, Int. J. Hydrogen Energy. 14 (1989) 797–820. doi:10.1016/0360-3199(89)90018-9.

[6] U. Bossel, B. Eliasson, G. Taylor, The Future of the Hydrogen Economy: Bright or Bleak?, Cogener. Distrib. Gener. J. 18 (2003) 29–70. doi:10.1080/15453660309509023.

[7] L. Barreto, A. Makihira, K. Riahi, The hydrogen economy in the 21st century: A sustainable development scenario, Int. J. Hydrogen Energy. 28 (2003) 267–284. doi:10.1016/S0360-3199(02)00074-5.

[8] F.F. Abdi, L. Han, A.H.M. Smets, M. Zeman, B. Dam, R. van de Krol, Efficient solar water splitting by enhanced charge separation in a bismuth vanadate-silicon tandem photoelectrode, Nat. Commun. 4 (2013) 17594–17598. doi:10.1038/ncomms3195.

[9] M. Orlandi, S. Caramori, F. Ronconi, C.A. Bignozzi, Z. El Koura, N. Bazzanella, L. Meda, A. Miotello, Pulsed-Laser Deposition of Nanostructured Iron Oxide Catalysts for Efficient Water Oxidation, ACS Appl. Mater. Interfaces. 6 (2014) 6186–6190. doi:10.1021/am501021e.

[10] A. Steinfeld, Solar hydrogen production via a two-step water-splitting thermochemical cycle based on Zn=ZnO redox reactions, Int. J. Hydrogen Energy. 27 (2002) 611–619.

[11] E.C.E. Rönnebro, E.H. Majzoub, Recent advances in metal hydrides for clean energy applications, MRS Bull. 38 (2013) 452–458. doi:10.1557/mrs.2013.132.

[12] J.-M. Joubert, M. Latroche, A. Percheron-Guégan, Metallic Hydrides II: Materials for Electrochemical Storage, MRS Bull. 27 (2002) 694–698. doi:10.1557/mrs2002.224.

[13] R.C. Bowman, B. Fultz, Metallic Hydrides I: Hydrogen Storage and Other Gas-Phase Applications, MRS Bull. 27 (2002) 688–693. doi:10.1557/mrs2002.223.

[14] C. Wadell, S. Syrenova, C. Langhammer, Plasmonic Hydrogen Sensing with

Nanostructured Metal Hydrides, ACS Nano. 8 (2014) 11925–11940. doi:10.1021/nn505804f.

[15] K. Samwer, Early and late stages of solid state amorphization reactions, J. Less Common Met. 140 (1988) 25–31. doi:10.1016/0022-5088(88)90364-5.

[16] J.N. Huiberts, R. Griessen, J.H. Rector, R.J. Wijngaarden, J.P. Dekker, D.G. de Groot, N.J. Koeman, Yttrium and lanthanum hydride films with switchable optical properties, Nature. 380 (1996) 231–234. doi:10.1038/380231a0.

[17] A. Unemoto, M. Matsuo, S. Orimo, Complex Hydrides for Electrochemical Energy Storage, Adv. Funct. Mater. 24 (2014) 2267–2279. doi:10.1002/adfm.201303147.

[18] L. Schlapbach, a Züttel, Hydrogen-storage materials for mobile applications., Nature. 414 (2001) 353–358. doi:10.1038/35104634.

[19] U. Eberle, R. von Helmolt, U. Eberle, Fuel cell vehicles : Status 2007 Fuel cell vehicles : Status 2007, J. Power Sources. 165 (2007) 833–843. doi:10.1016/j.jpowsour.2006.12.073.

[20] B. Panella, M. Hirscher, Physisorption in Porous Materials, in: Handb. Hydrog. Storage New Mater. Futur. Energy Storage, Wiley-VCH Verlag & Co, 2010: pp. 39–62. doi:10.1002/9783527629800.ch2.

[21] P. Chen, E. Akiba, S. Orimo, A. Zuettel, L. Schlapbach, Hydrogen Storage by Reversible Metal Hydride Formation, in: Hydrog. Sci. Eng. Mater. Process. Syst. Technol., Wiley-VCH Verlag GmbH & Co. KGaA, Weinheim, Germany, 2016: pp. 763–790. doi:10.1002/9783527674268.ch31.

[22] U. Eberle, M. Felderhoff, F. Schüth, Chemical and physical solutions for hydrogen storage, Angew. Chemie - Int. Ed. 48 (2009) 6608–6630. doi:10.1002/anie.200806293.

[23] K.L. Lim, H. Kazemian, Z. Yaakob, W.R.W. Daud, Solid-state materials and methods for hydrogen storage: A critical review, Chem. Eng. Technol. 33 (2010) 213–226. doi:10.1002/ceat.200900376.

[24] P. Prachi, M.M. Wagh, G. Aneesh, A Review on Solid State Hydrogen Storage Material, Adv. Energy Power. 4 (2016) 11–22. doi:10.13189/aep.2016.040202.

[25] M. Felderhoff, C. Weidenthaler, R. von Helmolt, U. Eberle, Hydrogen storage: the remaining scientific and technological challenges, Phys. Chem. Chem. Phys. 9 (2007) 2643. doi:10.1039/b701563c.

[26] A. Zutttel, Materials for hydrogen storage, Mater. Today. 6 (2003) 24–33. doi:10.1016/S1369-7021(03)00922-2.

[27] B.P. Tarasov, M. V. Lototskii, V. a. Yartys', Problem of hydrogen storage and prospective uses of hydrides for hydrogen accumulation, Russ. J. Gen. Chem. 77 (2007) 694–711. doi:10.1134/S1070363207040329.

[28] Q. Lai, M. Paskevicius, D.A. Sheppard, C.E. Buckley, A.W. Thornton, M.R. Hill, Q. Gu, J. Mao, Z. Huang, H.K. Liu, Z. Guo, A. Banerjee, S. Chakraborty, R. Ahuja, K.F. Aguey-

Zinsou, Hydrogen Storage Materials for Mobile and Stationary Applications: Current State of the Art, ChemSusChem. 8 (2015) 2789–2825. doi:10.1002/cssc.201500231.

[29] A. Chambers, C. Park, R.T.K. Baker, N.M. Rodriguez, Hydrogen storage in graphite nanofibers, J. Phys. Chem. B. 102 (1998) 4253–4256. doi:10.1021/jp980114l.

[30] A.C. Dillon, K.M. Jones, T.A. Bekkedahl, C.H. Kiang, D.S. Bethune, M.J. Heben, Storage of hydrogen in single-walled carbon nanotubes, Nature. 386 (1997) 377–379. doi:10.1038/386377a0.

[31] H. Kabbour, T.F. Baumann, J.H. Satcher, A. Saulnier, C.C. Ahn, Toward new candidates for hydrogen storage: High-surface-area carbon aerogels, Chem. Mater. 18 (2006) 6085–6087. doi:10.1021/cm062329a.

[32] S.. Ye, X.. Gao, J. Liu, W.. Wang, H.. Yuan, D.. Song, Y.. Zhang, Characteristics of mixed hydrogen storage electrode, J. Alloys Compd. 292 (1999) 191–193. doi:10.1016/S0925-8388(99)00174-7.

[33] H. Furukawa, M.A. Miller, O.M. Yaghi, M. Heuchel, P. Harting, K. Quitzsch, M. Jaroniec, I. Gameson, P.A. Anderson, I.R. Harris, Independent verification of the saturation hydrogen uptake in MOF-177 and establishment of a benchmark for hydrogen adsorption in metal–organic frameworks, J. Mater. Chem. 17 (2007) 3197–3204. doi:10.1039/b703608f.

[34] A.G. Wong-Foy, A.J. Matzger, O.M. Yaghi, Exceptional H2 saturation uptake in microporous metal-organic frameworks, J. Am. Chem. Soc. 128 (2006) 3494–3495. doi:10.1021/ja058213h.

[35] P.M. Budd, A. Butler, J. Selbie, K. Mahmood, N.B. McKeown, B. Ghanem, K. Msayib, D. Book, A. Walton, A. Walton, The potential of organic polymer-based hydrogen storage materials, Phys. Chem. Chem. Phys. 9 (2007) 1802. doi:10.1039/b618053a.

[36] G. (Gavin) Walker, M. Institute of Materials, Solid state hydrogen storage : materials and chemistry, Woodhead Pub., 2008.

[37] L. Klebanoff, J. Keller, Final Report for the DOE Metal Hydride Center of Excellence, (2012) 1–163. https://www1.eere.energy.gov/hydrogenandfuelcells/pdfs/metal_hydride_coe_final_report.pdf (accessed May 13, 2017).

[38] S.S. Makridis, Hydrogen storage and compression, MRS Bull. 33 (2008) 421–428. doi:10.1557/mrs2008.84.

[39] P. Adametz, K. Müller, W. Arlt, Energetic evaluation of hydrogen storage in metal hydrides, Int. J. Energy Res. 40 (2016) 1820–1831. doi:10.1002/er.3563.

[40] M.M.H. Bhuiya, A. Kumar, K.J. Kim, Metal hydrides in engineering systems, processes, and devices: A review of non-storage applications, Int. J. Hydrogen Energy. 40 (2015) 2231–2247. doi:10.1016/j.ijhydene.2014.12.009.

[41] H. Smithson, C.A. Marianetti, D. Morgan, A. Van der Ven, A. Predith, G. Ceder, First-

principles study of the stability and electronic structure of metal hydrides, Phys. Rev. B. 66 (2002) 144107. doi:10.1103/PhysRevB.66.144107.

[42] J.E. Schirber, Effect of hydriding pressure on the superconducting transition temperature of palladium hydride and palladium rhodium hydride, Phys. Lett. A. 45 (1973) 141–142. doi:10.1016/0375-9601(73)90461-1.

[43] A. Pundt, Hydrogen in Nano-sized Metals, Adv. Eng. Mater. 6 (2004) 11–21. doi:10.1002/adem.200300557.

[44] L.H. Jepsen, M. Paskevicius, T.R. Jensen, Nanostructured and Complex Hydrides for Hydrogen Storage, in: Nanotechnol. Energy Sustain., Wiley-VCH Verlag GmbH & Co. KGaA, Weinheim, Germany, 2017: pp. 415–432. doi:10.1002/9783527696109.ch18.

[45] B. Sakintuna, F. Lamari-Darkrim, M. Hirscher, Metal hydride materials for solid hydrogen storage: A review, Int. J. Hydrog. Energy. 32 (2007) 1121–1140. doi:10.1016/j.ijhydene.2006.11.022.

[46] M. Zhu, H. Wang, L.Z. Ouyang, M.Q. Zeng, Composite structure and hydrogen storage properties in Mg-base alloys, in: Int. J. Hydrogen Energy, 2006: pp. 251–257. doi:10.1016/j.ijhydene.2005.04.030.

[47] L. Zaluski, A. Zaluska, J.. Ström-Olsen, Nanocrystalline metal hydrides, J. Alloys Compd. 253 (1997) 70–79. doi:10.1016/S0925-8388(96)02985-4.

[48] H. Imamura, K. Masanari, M. Kusuhara, H. Katsumoto, T. Sumi, Y. Sakata, High hydrogen storage capacity of nanosized magnesium synthesized by high energy ball-milling, Elsevier Science Pub. Co, 2005. doi:https://doi.org/10.1016/j.jallcom.2004.04.145.

[49] A. Zaluska, L. Zaluski, J.O. Ström-Olsen, Structure, catalysis and atomic reactions on the nano-scale: a systematic approach to metal hydrides for hydrogen storage, Appl. Phys. A Mater. Sci. Process. 72 (2001) 157–165. doi:10.1007/s003390100783.

[50] M. Mamatha, B. Bogdanović, M. Felderhoff, A. Pommerin, W. Schmidt, F. Schüth, C. Weidenthaler, Mechanochemical preparation and investigation of properties of magnesium, calcium and lithium–magnesium alanates, J. Alloys Compd. 407 (2006) 78–86. doi:10.1016/j.jallcom.2005.06.069.

[51] Y. Kim, E.-K. Lee, J.-H. Shim, Y.W. Cho, K.B. Yoon, Mechanochemical synthesis and thermal decomposition of Mg(AlH4)2, J. Alloys Compd. 422 (2006) 283–287. doi:10.1016/j.jallcom.2005.11.063.

[52] V. A., D. G., J. Grbovic, D. M., Hydrogen Economy: Modern Concepts, Challenges and Perspectives, in: Hydrog. Energy - Challenges Perspect., InTech, 2012: pp. 3–28. doi:10.5772/46098.

[53] M.U. Niemann, S.S. Srinivasan, A.R. Phani, A. Kumar, D.Y. Goswami, E.K. Stefanakos, Nanomaterials for hydrogen storage applications: A review, J. Nanomater. 2008 (2008) 1–9. doi:10.1155/2008/950967.

[54] X. Chen, C. Li, M. Grätzel, R. Kostecki, S.S. Mao, Nanomaterials for renewable energy production and storage, Chem. Soc. Rev. 41 (2012) 7909. doi:10.1039/c2cs35230c.

[55] X.-L. Wang, S. Suda, Surface characteristics of fluorinated hydriding alloys, J. Alloys Compd. 231 (1995) 380–386. doi:10.1016/0925-8388(95)01851-4.

[56] A. Zaluska, L. Zaluski, J.. Ström–Olsen, Nanocrystalline magnesium for hydrogen storage, J. Alloys Compd. 288 (1999) 217–225. doi:10.1016/S0925-8388(99)00073-0.

[57] I.P. Jain, C. Lal, A. Jain, Hydrogen storage in Mg: A most promising material, Int. J. Hydrogen Energy. 35 (2010) 5133–5144. doi:10.1016/j.ijhydene.2009.08.088.

[58] K.-F. Aguey-Zinsou, J.-R. Ares-Fernández, Synthesis of Colloidal Magnesium: A Near Room Temperature Store for Hydrogen, Chem. Mater. 20 (2008) 376–378. doi:10.1021/cm702897f.

[59] R.A. Varin, L. Zbroniec, M. Polanski, J. Bystrzycki, A review of recent advances on the effects of microstructural refinement and nano-catalytic additives on the hydrogen storage properties of metal and complex hydrides, Energies. 4 (2011) 1–25. doi:10.3390/en4010001.

[60] K.-J. Jeon, H.R. Moon, A.M. Ruminski, B. Jiang, C. Kisielowski, R. Bardhan, J.J. Urban, Air-stable magnesium nanocomposites provide rapid and high-capacity hydrogen storage without using heavy-metal catalysts, Nat. Mater. 10 (2011) 286–290. doi:10.1038/nmat2978.

[61] F. Cheng, Z. Tao, J. Liang, J. Chen, Efficient hydrogen storage with the combination of lightweight Mg/MgH2 and nanostructures, Chem. Commun. 48 (2012) 7334. doi:10.1039/c2cc30740e.

[62] R. Bardhan, A.M. Ruminski, A. Brand, J.J. Urban, Magnesium nanocrystal-polymer composites: A new platform for designer hydrogen storage materials, Energy Environ. Sci. 4 (2011) 4882–4895. doi:10.1039/c1ee02258j.

Chapter 2

Synthesis of metallic nanopowders (MNPs)

2. Introduction to the metallic nanopowders (MNPs)

In nanotechnology the particles can be defined as small localized objects with several physical or chemical properties [1]. According to their dimensions particles can be divided in different categories: the "coarse particles" are particles with a size over 2500nm, the "fine particles" are particles with a size in the range of 100 – 2500nm; the particles in the size range of 1 – 100nm are addressed as nanoparticles (NPs) [2]. Fragments of solid with nucleating ranging between a few atoms and thousands of atoms are known as nano-clusters or nano-crystals**.** The nanostructured materials (NSMs) may be defined as ultrafine nanostructures whose structural elements — clusters, crystallites or molecules — have dimensions in the 1 to 100 nm range [3,4]. When the dimensions of a system are reduced to the nanoscale domain, the number of atoms at the surface significantly increases with increasing of the surface area per unit volume. The reduction of particles size leads to a high surface-to-volume ratio and consequentially to an high surface area provided of an high free energies and cluster reactivities. Hence when the dimensions decrease from micron level to nano-level the specific surface area increases by 3 orders of magnitude [1]. In such a case, large portions of atoms will either be at or near the grain boundaries [5]. Their properties falls in between of those of the isolated atoms and of the bulk macroscopic materials [6]. Owing to these surface contributions, the structure and the total energy of the systems change, providing improvements in some of NSMs properties such as electrical [7,8], mechanical [9], optical [10], magnetic [11,12] and hydrogen sorption properties [13–15], that are shown to be powerfully higher than the corresponding bulk materials. The size

and shape effects play an important role on the materials properties. They result to be affected by a "quantum size effects" or "quantum confinement" phenomenon, which is an effect observed when the size of the particle is too small to be comparable to the wavelength of the electrons. These effect is caused by the spatial confinement of delocalized electrons in confined grain sizes [5], and it is essentially due to the changes in the atomic structure as result of the direct influence of the ultra-small length scale on the energy band structure. This effect will be better explained for the nanosized metals. The metallic nanopowders (MNPs) can be described as nanosized metals with dimensions within the NPs size range. The existence of metallic NPs in solution was first recognized by Faraday in 1857 [16] and a quantitative explanation of their color was given by Mie in 1908 [17]. When metal particle having bulk properties are reduced to a few hundred atoms, the density of states in the conduction band (the top band containing electrons) changes dramatically. With the decreasing of the dimensions the continuous density of states in the conduction band is replaced by a set of discrete energy levels, which may have energy level spacing larger than the thermal energy, k_BT, and a gap opens up [18]. The transition between molecular and metallic states provide a specific electronic structure (local density of states LDOS). The changes in the electronic structure during the transition of a bulk metal to a large cluster, and then down to a small cluster of less than 15 atoms [19], are illustrated in Figure 2.1.

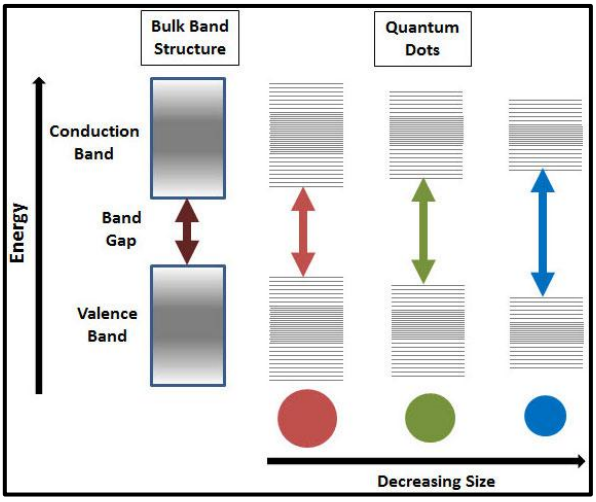

Figure 2.1 Splitting of energy levels in quantum dots due to the quantum confinement effect, semiconductor band gap increases with decrease in size of the nanocrystal.

The small cluster is analogous to a molecule having discrete energy levels with bonding and antibonding orbitals. Finally a size is reached where the surfaces of the particles are

separated by distances which are in the order of the wavelengths of the electrons. In this situation the energy levels can be described by the quantum-mechanical treatment of a particle in a box. This is referred to as the quantum size effect. The average energy will not be determined so much by the chemical nature of the atoms, but mainly by the particle dimensions. Another important effect that characterizes the nano-sized metals is the "surface plasmon resonance" effect. The surface plasmon resonance (SPR) is an effect arising from the interaction of light with mobile surface chargers in a metal [20], and it is strictly dependent on the surface and interface properties. This effect modifies the optical properties of the metals. The color of a material is determined by the wavelength of light that it absorbs. The absorption occurs because electrons are induced by the photons of the incident light to make transitions between the lower-lying occupied levels and higher unoccupied energy levels of the materials. Clusters of different sizes will have different electronic structures, and different energy-level separations. Light-induced transitions between these levels determine the color of the materials. This means that clusters of different sizes can have different colors, and the size of the cluster can be used to engineer the color of a material [18]. The benefits of nanostructuring effects mainly for the MNPs in a large number of technological applications have been reported in many literature works. About the hydrogen storage applications, the study of the relationship between structure and absorption properties of materials plays an important role for their potential storage capabilities improvements. Therefore, materials scientists are focusing their efforts to develop simple and effective approaches for fabricating nanometals with desired size and morphology for the specific technological applications.

2.1. Brief description of synthesis strategies

There are two main approaches to synthesize the nanomaterials: one is the "top-down" approach and another one is the "bottom-up" approach. In Figure 2.2 a schematic representation of both approaches is reported.

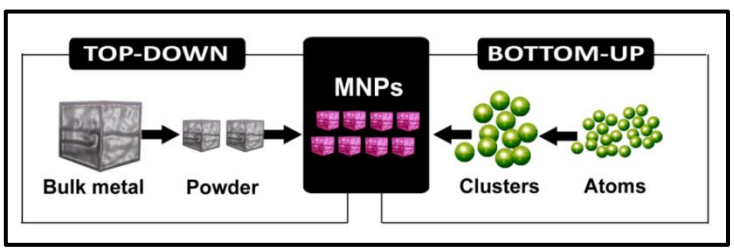

Figure 2.2 Schematic of variety of nanostructure synthesis and assembly approaches.

2.1.1. Top-down approach

The top-down approach consists of building nanomaterials moving from top (larger) to bottom (smaller). NPs are synthesized by breaking down bulk materials gradually into smaller sizes, e.g. by using high-energy ball milling (mechanical milling). Different kinds of techniques as lithographic techniques (such as electron beam, photo ion beam or X-ray lithography cutting), etching, grinding, ball milling and sol gel technique make use of this approach. This method is advantageous as it is easy and simple to perform and avoid the use of volatile and toxic compounds often used in bottom-up techniques. However, by using this approach there is a not good control on the nucleation and growth of the NPs produced. In fact the NPs produced are of very low dimensions, but without well-defined characteristics or uniform shape and of a narrow size distribution. In addition contamination effects can occur coming out from the apparatus as, in the ball milling case, from the grinding media. Nevertheless, many top-down techniques have been developed on the industrial scale, due to the simplicity of these processes, and an optimization of these processes can produce well-defined structures on scales previously forbidden. The use of these approaches has a limit on reaching very small dimensions, which can be solved by the bottom-up approach. Thus, to produce devices with extremely fine details (on the molecular level), self-assembly and directed assembly approaches must be integrated into the industrial process. It is expected that NPs prepared by chemical synthesis and self-assembly will play a critical role in in the research fields [21].

2.1.2. Bottom-up approach

As the name suggest, the bottom-up is an approach to build nanomaterials by going from bottom (smaller) to the top (larger). The bottom up approach starts with atoms, ions or molecules as "*building block*s" and assembles nanoscale clusters or bulk material from them [21,22]. This method implies that the nanostructures are synthesized onto the substrate by stacking atoms onto each other, which gives rise to crystal planes, crystal planes further stack onto each other, resulting in the synthesis of the nanostructures. A fine control on the nucleation and growth of the particles, by changing the physiochemical parameters, allow to obtain self-assembled materials with a fine structure highly controlled. Some physical techniques using this approach are the chemical vapor reactions, laser or plasma treatment, aerosol pyrolysis (spray pyrolysis, vapor pyrolysis). Instead the most common chemical techniques are synthetic process as colloidal synthesis, thermal

decomposition, sol-gel, microwave heating, synthesis in microemulsions or reverse micelles and sonochemical synthesis. Using these chemical approaches a really tailored material can be achieved for advanced technology applications. Countless bottoms up synthetic strategies of NPs are being developed.

2.2. Overview to the (MNPs) synthesis techniques

Although many techniques used for the MNPs synthesis have been employed, the synthetic techniques can be grouped in two broad classes known as "physical and chemical methods". Several options for these processes have been developed to generate compounds or alloys with specific compositions and properties by optimizing the synthesis approaches.

2.2.1. Physical synthesis techniques

About the physical methods, the most common used for the MNPs production are the vapor-phase synthesis. One useful way to classify such methods is by starting from the phase of the precursor and from the source of energy used. Starting by a solid precursor, one general class of methods for achieving the supersaturation necessary to induce an homogeneous nucleation of MNPs is to vaporize the material into a background gas and then cooling down the gas [23]. The most known methods for the vapor-phase synthesis are the inert gas condensation [24], the pulsed laser ablation (PLA) [25,26], the spark discharge generation [27], the ion sputtering [28] and the physical vapor deposition (PVD) [29]. An alternative way of achieving the supersaturation necessary to induce homogeneous nucleation of NPs is by the chemical reaction. In this case a liquid or vapor precursor is used. Chemical precursors are heated and/or mixed to induce gas-phase reactions that produce a state of supersaturation in the gas phase. Starting by a chemical precursors other methods for the vapor-phase synthesis are the chemical vapor deposition (CVD) [30–32], the spray pyrolysis [33], the laser pyrolysis/photothermal synthesis, the thermal plasma synthesis, the flame synthesis, the flame spray pyrolysis and the low-temperature reactive synthesis. However, the synthesis of nano-metals via these physical approaches generally involves complex procedures and equipments, relatively high pressures and temperatures. Hence, nano-metals clusters prepared in these conditions will readily oxidize if exposed to the atmosphere. This generally degrades some of clusters properties. In particular, the metallic clusters can be dramatically affected by contamination (oxidation and aggregation phenomena) if are exposed at ambient

atmosphere after the synthesis, losing their functional properties. During the last decades the interest for other physical synthetic approach, e.g. the ball milling, is increased. It has been widely used for brittle metal and alloy metal nanoparticle production, mainly for hydrogen storage applications [13,14,22,34]. The success of this technique is mainly due to its scalability and easy of use. In addition, the ball milling is an inexpensive method. Ball milling is a mechanical process in which the structural and chemical changes are produced by mechanical energy. A graphic representation of the working principle of a planetary ball mill is reported in Figure 2.3. The metal is placed in a rotating cylinder or conical mill partially filled with inert grinding media that causes fracturing and cold welding of the elemental constituent particles.

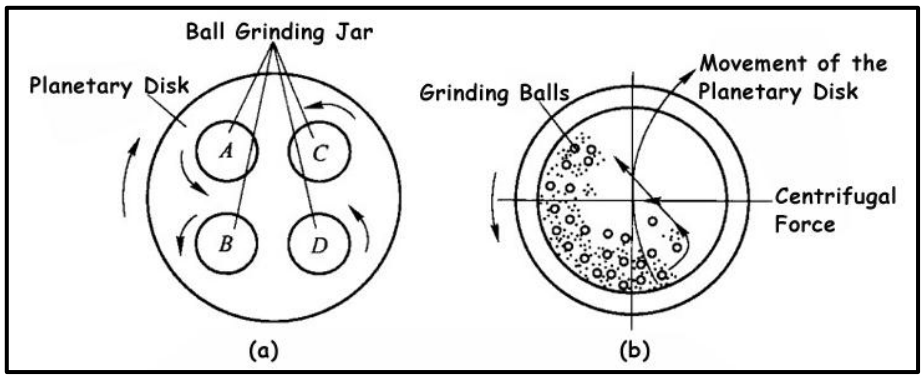

Figure 2.3 Graphic representation of working principle of Planetary Ball Mill (a) overall layout of planetary ball mill end (b) horizontal section of grinding jar

The final result is a powder made of nanocrystals of a few tens of nanometers. The technique has the benefits to reduce the grain size, to promote the formation of micro/nanostructures and to create defects on the surface and inner the materials. The result is an increasing of the surface area. The induced lattice defects and in general of the defects concentration may aid a shortening the diffusion path of hydrogen in materials by providing many sites with low activation energies. It is possible to obtain a tailored material with specific properties by checking the milling parameters. It is possible to obtain a powder with superior morphology by using some improvements as the use of catalysts during the milling process. It is able to give remarkable improvements to the kinetic of the process and to the surface activity for hydrogenation [34]. Many works have been done describing this technique, especially for the metal hydrides production for hydrogen storage applications [35–38]. However, the most important disadvantage in the use of this

technique consist in the passivation effects by oxygen which occur during the synthesis, with formation of an oxygen layer on the metal surface that inhibits the hydrogen diffusion inside the metal [39,40]. Fluorination treatments of metals are proposed to re-active the metals surface [39,41]: this chemical treatments not only removes the existing oxide layer but also prohibits further oxidation phenomena thanks to the formation of a special catalytic structure on the surface. The fluorination method involves chemical treatment of the hydride with an aqueous solution of F^- ions, resulting in much better activity for hydrogenation and easier activation. Nevertheless, the use of these enhancements treatments involves complex procedures, and therefore it is not recommended, especially for air-sensitive materials as magnesium.

2.2.2. Chemical synthesis techniques

Therefore, further research work has been done to develop new synthetic approaches to produce MNPs by using chemical methods. The physicochemical properties strictly depend on size, thus chemical methods are required to achieve tailored NPs. These methods provide a simple and versatile option for the MNPs preparation, due to mild synthesis conditions and higher product uniformity. Among them the colloidal chemistry has been extensively used to synthesize nanoclusters with controllable morphology and narrow size distributions, enabling to obtain tailored properties [42–44]. A colloid is a suspension of particles with sizes ranging from 1 nm to 1μm (i.e., 1000 nm), larger than most ordinary molecules, but still too small to be seen by the naked eyes. Many colloidal particles can, however, be detected by the way in which they scatter the light, such as dust particles in air. These particles are in a state of constant random movement, called *Brownian motion,* arising from collisions with solvent molecules, which themselves are in motion. Particles are kept in suspension by repulsive electrostatic forces existing between them. The addition of salt to a colloid can weaken these forces and can lead to the formation of aggregates of suspended particles, which can be collected as sediment at the bottom of the solvent. This process of the settling out of a colloid is called *flocculation* [18]. The polyol process is a chemical reduction of the ionic precursors (organic and inorganic salts) which occurs in presence of a mild reducing agents as the alcohols, to produce fine particles. Modulating the synthesis parameters, as temperature, pressure, time, reaction environment, and also reagents and the polyol liquid or other additive chosen, it is possible to obtain a good control on nucleation and growth of the MNPs. Another easy and useful approach widely used for the nano-sized metals preparation is the thermolysis, or

thermal decomposition [18]. This technique is a chemical reaction process caused by heating. The decomposition temperature of a substance is the temperature at which the substance chemically decomposes. The reaction is usually endothermic, since heat is required to break the chemical bonds in the compound, undergoing the decomposition. A suitable compound, usually an organometallic substance of the metal chosen, is used for the MNPs preparation [45,46].

2.3. Chemical reduction: the polyol process

Many fine metallic powders can be prepared by reduction of a suitable precursor using a mild reducing agent, as the alcohols that can be easily oxidized to aldehydes or ketones, according to their nature. The metal ions, coming by the dissolution of precursors in the alcoholic liquid, are reduced to a zero-valence state atom. The primary alcohols ($R\text{-}CH_2\text{-}OH$) can be oxidized either to aldehydes (R-CHO) or to carboxylic acids ($R\text{-}CO_2H$), while the oxidation of secondary alcohols ($R^1R^2CH\text{-}OH$) normally give a ketone ($R^1R^2C{=}O$). In any case, the oxidation occurs on the α-carbon. Tertiary alcohols ($R^1R^2R^3C\text{-}OH$) are resistant to oxidation, due to the absence of hydrogen on α-carbon [47]. The scheme of the oxidation reaction mechanism of alcohols is reported in Figure 2.4. Liquid α-diols, such as 1,2-ethane diol (ethylene glycol, EG) or 1,2-propanediol (propylene glycol, PEG) are generally preferred because presents an higher reducing power than the primary alcohols. However, also the diol ethers resulting from the condensation of α-diols, such as diethylene glycol (DEG), triethylene glycol (TEG) or tertaethylene glycol (TTEG) have been used as well [48]. The starting compound may be rather soluble (nitrate, chloride, acetate) or it may be only slightly soluble (oxide, hydroxide) in the polyol. The solution or the suspension is stirred and heated to a given temperature, which can reach the boiling point of the polyol for less reducible metals; conversely, for easily reducible metals (e.g. Pd) the reaction can be carried out at temperatures as low as 0°C from a suitable precursor. The polyol acts, at the same time, as a solvent, reducing agent, crystal growth medium for the metal particles and, in some cases, as a complexing agent for the metallic cations. The mechanism of formation and growth of metal NPs involves three steps:

1. the dissolution of the precursor;
2. the polyol reduction of the dissolved species;
3. the nucleation and growth of the metal particles from the saturated solution.

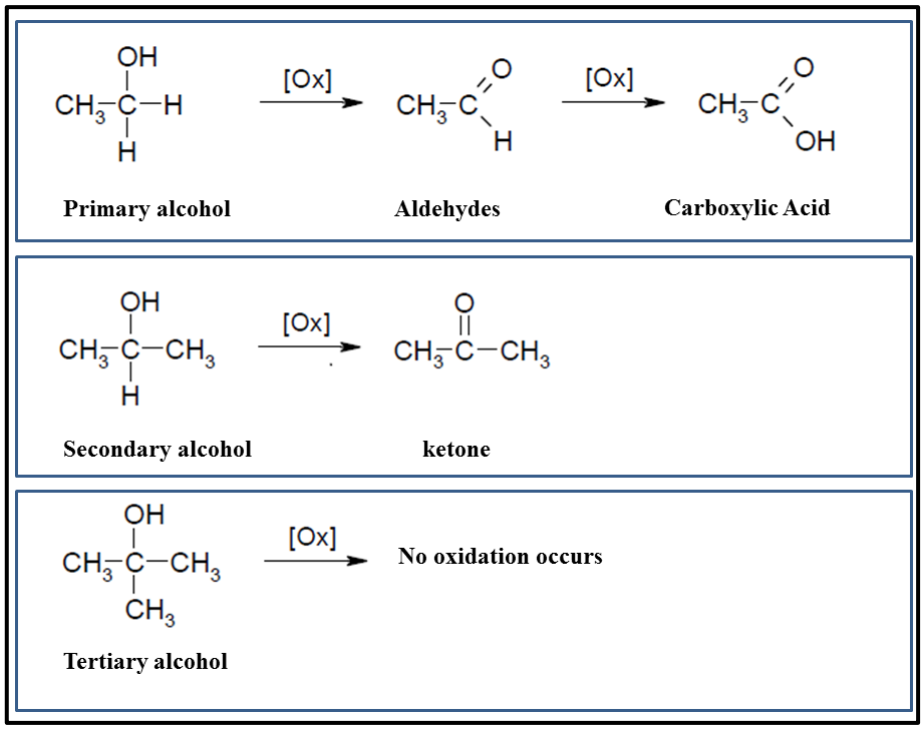

Figure 2.4 Scheme of the oxidation reaction mechanism of alcohols

The main features of this process is that it is possible, by acting upon the experimental conditions, to control the kinetics of the precipitation, and thus to obtain nonagglomerated metal particles with well-defined shape, a controlled average size from micrometer to nanometer size range, and a narrow size distribution. In order to obtain particles with such well-defined morphological characteristics it is necessary to maintain separated the "nucleation" and "growth" steps.

2.3.1. Control of the nucleation step

Nucleation is a purely thermodynamic model which describes the process of the first step in a first order phase transition. It describes the appearance of a new phase – the nucleus – in the metastable primary phase [49]. Spontaneous nucleation occurs when the concentration of the metal generated by the reduction reaches a critical supersaturation level. This is on the base of the classical nucleation theory (CNT) developed by LaMer's and his colleagues back in the 1950s, in which the concept of "*burst"* nucleation has been introduce.

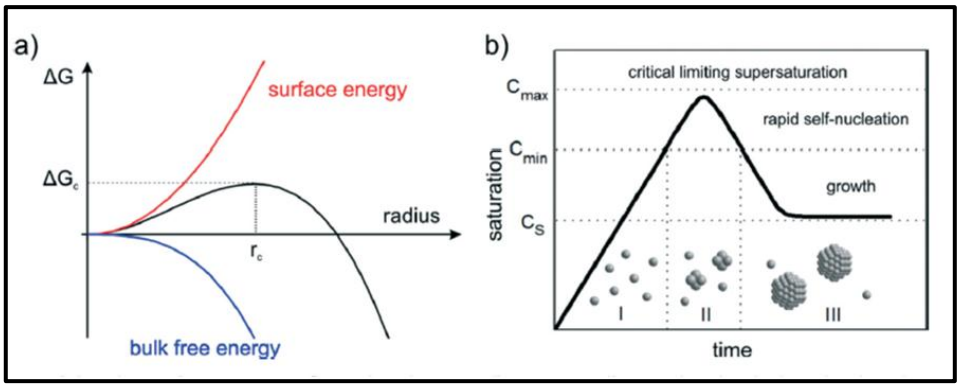

Figure 2.5 Nucleation and growth according to LaMer's model

The pioneering concept was developed from their research on various oil aerosols and sulfur hydrosols. In the burst nucleation process, the nuclei are generated in the homogeneous phase (homogeneous nucleation) and subsequently grow without additional nucleation. The basic idea of that MNPs formation concept is to separate nucleation and growth. It can be interpreted as a separation of a homogeneous from a heterogeneous phase. Such a process enables control of the particle size distribution during growth. The mechanism, displayed in Figure 2.5 , is as follows:

I. the concentration of monomers is increasing (in the case of metallic NPs most likely due to reduction) and it reaches, at a certain time, a critical supersaturation level (CS) at which homogeneous nucleation occurs;
II. the saturation increases and reaches a level (C_{min}) at which the energy barrier (activation energy) for nucleation can be exceeded, leading to a rapid self-nucleation – the burst nucleation;
III. and due to the burst nucleation, the supersaturation level lowers immediately below this self-nucleation level ending the nucleation period; growth then occurs by diffusion of further monomers in solution towards particle surfaces which can be seen as heterogeneous nucleation/growth.

The expected corresponding particle concentration with respect to time would increase fast at the self-nucleation stage (II) and a more or less constant value during the final growth stage (III). To prevent further nucleation during the growth step, supersaturation must remain at a low level. This can be achieved by different methods. Starting from a very soluble precursor, the reaction of formation of the final solid compound from the solution has to be carried out at a sufficiently low temperature. When various soluble precursors may be used, one can select the most suitable one. In other cases it is possible to control

the concentration of the precursor species in solution. These species being provided by the progressive dissolution of a sparingly solid phase (starting compound or intermediate solid phase) acting as a kind of reservoir. The dissolution equilibrium regulates the release of these species, controls the supersaturation ratio, and then allows having a very brief nucleation step [48]. The LaMer's model and its modifications are still the only commonly accepted models describing the general mechanism of the MNP formation process. In principle, the model explains also conventional strategies for size adjustment of colloidal NPs, i.e. fast reduction to induce a rapid build-up of supersaturation. As a consequence, many nucleation events lead to many small NPs, and few events to less and bigger particles. Moreover, the principles of "seeded-growth" are derived from the concept of classical nucleation, i.e. suppressing further nucleation by slow reduction to use reduced monomers exclusively for growth on already formed particles. However, the LaMer model is not able to predict or characterize the evolution of NP size distributions; it only describes the process of nucleation followed by a growth of the stable nuclei, but the characteristics of the growth remain more or less unspecific.

2.3.2. Growth and stabilization of NPs

The particles growth may proceed by diffusion of the solute species toward the surface of the particles and stepwise addition of atoms or ions to form the clusters. Secondary larger particles can be formed by coalescence of primary particles. The mechanism is reported in Figure 2.6 [49]. In general, particles at the nanoscale are unstable and tend to agglomerate because at short interparticle distances they are attracted to each other by Van der Waals, electrostatic or magnetic forces. Without any counteractive repulsive forces NPs aggregate, agglomerate or undergo coalescent processes. Such repulsive forces can be achieved by electrostatic or steric stabilization, or a combination of these two (electrosteric forces) [50].

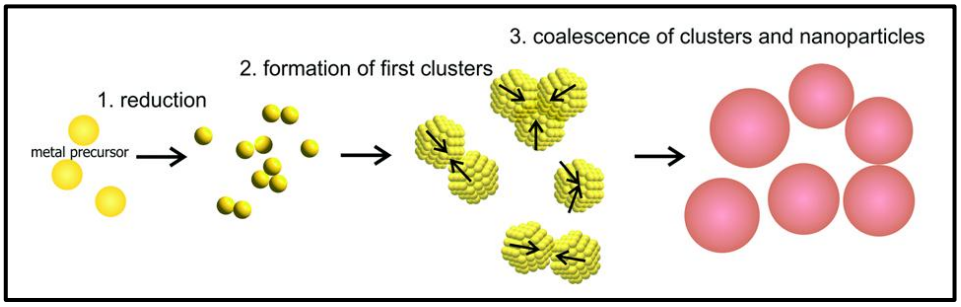

Figure 2.6 Schematic of the generalized 3-step mechanism of nanoparticle growth.

Electrostatically stabilized NPs are described to have at least one electrical double layer due to a surface charging. The resulting Coulomb repulsion forces between the particles decay exponentially with particle to particle distance. If the electrostatic repulsion is sufficiently high, it prevents the particles from any kind of coagulation. The stabilizer is typically introduced during the formation of the NPs, and this is achieved via the chemical or electrochemical reduction or thermal decomposition of metallic precursors. The interaction between the stabilizers and the surface of the nanoparticle can take many forms, such as a strong covalent linkage (as in the case of a thiol), a chemisorbed atom or an electrostatic interaction with a layer of anions (within a double layer structure of a surfactant). The formation of NPs, in this particular case of MNPs of palladium, stabilized by the most common stabilizers (organic ligands, surfactants, polymers and dendrimers) is shown in Figure 2.7.

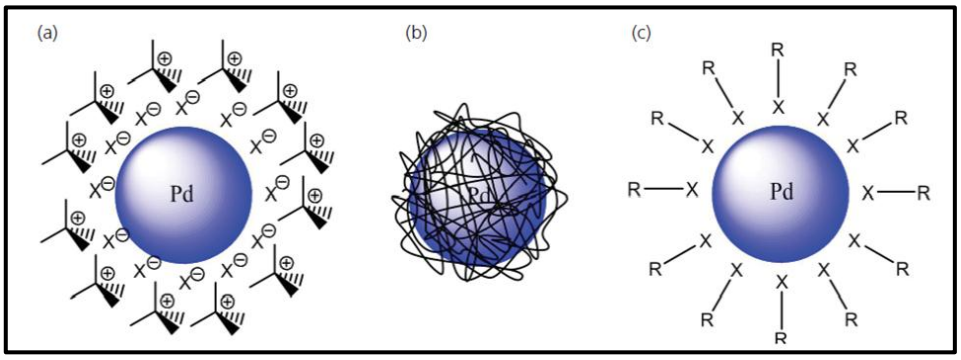

Figure 2.7 Schematic representing the stabilization of palladium nanoparticles using different protecting groups: (a) surfactants; (b) polymers; and (c) ligands

Steric stabilization can be provided by the polyol itself or by adding long-chain molecules, as polymeric matrixes. The adsorption of such protective agents can also be used to limit the growth if necessary in order to obtain MNPs. Polymers, such as poly(N-vinyl-2-pyrrolidone) (PVP) and poly(vinyl alcohol) (PVA), are widely used to protect NPs because of their commercial availability at relatively low cost and their solubility in a range of solvents, including water [51]. The use of polymers is often associated with the polyol method, in which a metal precursor is dissolved and reduced at high temperatures by an alcohol. The stabilizer performs the important role of nucleating agent for the metal atoms with a fast phase separation, since metal atoms coordinated to the polymer side-groups are forced at short distances during nucleation [52]. In the Figure 2.8 a schematic representation of the reduction process of metal salts in the presence of a stabilizing polymer is reported.

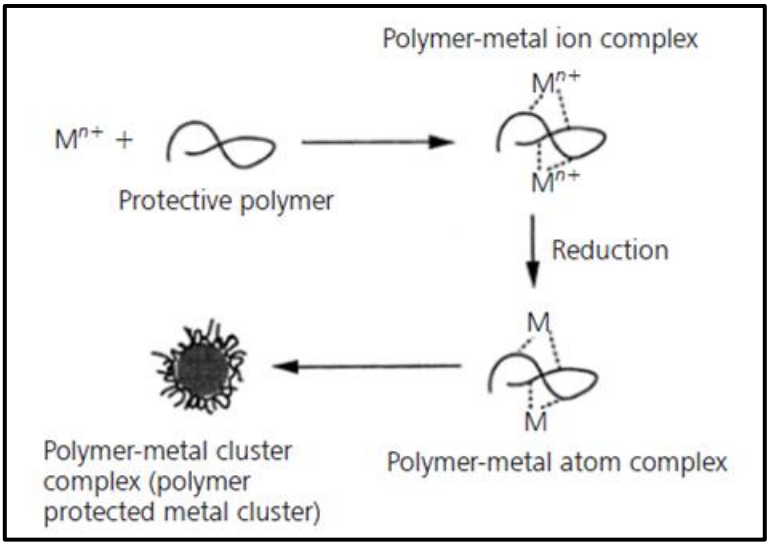

Figure 2.8 Schematic representation of the reduction process of metal salts in the presence of a stabilizing polymer

Nevertheless, it must be pointed out that in some particular cases the formation of quasi-spherical secondary metal particles. These small crystals or particles can be re-deposited on the on the surfaces of the dissolved species obtained in the early stages of precipitation, through a coalescence mechanism. This phenomenon known as "Ostwald ripening" is a common phenomenon taking place in solid solutions or liquid sols.

2.4. Thermal decomposition

The thermal decomposition processes (or thermolysis) play an important role in various practical fields including metallurgy, mineral conversion processes, pyrogenic chemical technology, pyrolysis and thermal treatment of wood and coal, combustion of natural and synthetic fuels, coal carbonization and so on. There is still need for scientifically well-founded approaches to control the thermal decomposition of materials. Many researchers are studying the chemical decomposition of complex substances to develop the mathematical models for such processes. Nevertheless, the thermolysis process is widely used in the synthesis of nano-sized metal-polymer composites, and the bottom-up approaches result to be the most developed [53]. Between the thermochemical decomposition processes, the pyrolysis represents a new and rapid method for the nanocomposites preparation. Pyrolysis is a thermo-chemical decomposition process involving organometallic compounds, organic and inorganic salts and inorganic compounds at elevated temperatures, in the absence of oxygen. This process is most

commonly used for the nanostructured metals production [45,54–56]. It involves the simultaneous change of chemical composition and physical phase, and it is not reversible. Pyrolysis differs from other processes like combustion and hydrolysis because it usually does not involve reaction with oxygen, water, or any other reagents. In practice, it is not possible to achieve a completely oxygen-free atmosphere, because some oxygen is present in the pyrolysis system, so a small amount of oxidation also occurs.

2.4.1. Brief introduction to suitable precursors for the thermolysis

The most suitable compounds for the preparation of metal-polymer nanocomposites are:

1. metal salts;
2. organometallic compounds.

2.4.2. Metal salts

Many literature works report that a lot of metal-polymer nanocomposites have been prepared starting by inorganic salts of metals, such as metal nitrates like $AgNO_3$ [57–59] or salts of metals as $HAuCl_4$ [60], by dissolution into a polymer matrix. The advantage in the use of this kind of precursors is that they are commercially available products, so preliminary synthesis is not needed. It is possible to achieve the desired metal-polymer nanocomposites by thermal decomposition "*in situ*" of the inorganic salt, in a fast and scalable way. One disadvantage is that a good control on the morphology (shape and size distribution) is not guaranteed. In fact, only nanocrystals of irregular morphology embedded into the polymer are obtained with this kind of precursors. Also, the major disadvantage is the trapping of the by-products into the polymer. The organometallic compounds are the compounds most widely used in the thermolysis process.

2.4.3. Organometallic Compounds

An organometallic compound is a compound that must contain at least one metal atom and at least one organic portion bound to it; this classification criterion involves the existence of a particular bond between the atoms of the metal and the carbon atoms [61]. The

particular nature of organometallic compounds depends essentially on the fact that the type of bond between the atoms of the metal and the carbon atoms generally makes the molecules extraordinarily reactive. The simplest case is that of non-polar σ-bond between metal and carbon, which is preferably formed when the difference of electronegativity (or electron affinity) between the metal atoms and the carbon atoms is small. Examples of this type of bond can be found in the metal compounds of the groups IlIa and IVa, which may be very reactive, such as borotrimethyl ($B(CH_3)_3$), or relatively inert, such as silicon tetramethyl ($Si(CH_3)_4$) and tetramethyl lead ($Pb(CH_3)_4$). When the electronegativity difference between the metal and the carbon increases, the metal-carbon bond, which can still be formally described as a single σ bond, has a polar character, which we express here by means of the symbols δ^+ and δ^-. In this case the binding electrons are predominantly located on the carbon atom, and he resulting system is a dipole; molecules containing such binding tend to associate because of dipole-dipole interactions. A very special position in the knowledge of the organometallic chemistry of transition metals is occupied by metal-carbonyls, which are extremely stable compounds. The most important metal-carbonyls are hexacarbonylchromium ($Cr(CO)_6$), pentacarbonyliron ($Fe(CO)_5$), cobalt tetracarbonyl hydride ($Co(CO)_4H$) and tetracarbonilnichel ($Ni(CO)_4$). A class of organometallic compounds most commonly used in the thermolysis process, and then in other techniques a CVD, PVD and so on, are the cyclopentadienyl derivatives. The first example is the "ferrocene" which is stable up to 400°C. The molecule is a sandwich complex containing two co-planar and perfectly symmetrical cyclopentadienyl rings [62], as is shown in Figure 2.9; its extraordinary stability stems from the fact that the bonding system has the configuration of an inert gas, with 8 electrons of iron(0) and 10π-electron by two cyclopentadienyl radicals. It is interesting to note that the molecule can be formally represented as an iron (II) and two cyclopentadiene anions.

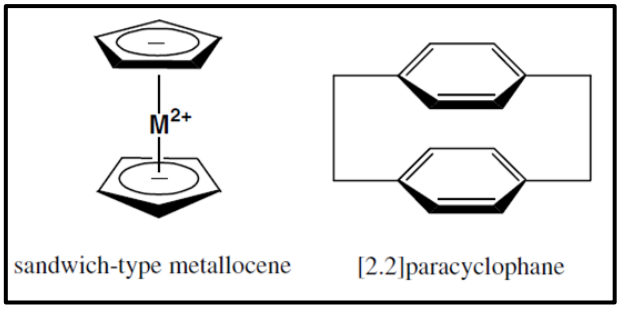

Figure 2.9 Typical sandwich-type metallocene and paracyclophane

The cyclopentadienyl anion ($C_5H_5^-$ = Cp^-) is an aromatic 6π-electron system. The interaction of both Cp^- rings of sandwich-type metallocenes may be compared with that which takes place between benzene rings in simple paracyclophanes [62]. One of the important features of organometallic compounds is that they are generally sensitive to oxygen and water, usually it is necessary to treat them in an inert atmosphere of argon or nitrogen. For example the bis(cyclopentadienyl)magnesium (Cp_2Mg), that is nowadays very much used for the synthesis nanostructured magnesium-based materials for hydrogen storage applications [63], is manipulated in an inert atmosphere.

2.4.4. Introduction to the thermal decomposition mechanism

Thermal decomposition is an exothermic process, so when the reaction occur, a certain amount of heat is released. This amount is usually directly proportional to the standard enthalpy of reaction of the corresponding compound. Different precursors can be used to generate the metallic nanoparticles; among them the metal acetylacetonates are most well-known. Selections of the suitable precursors for the thermolysis process have been previously discussed. The study of the thermal behavior of a substance helps to determine the temperature at which the substance decomposes and the zero-valence state metal is formed. A scheme of the chemical reaction for a generic metal compound is the following:

$$M\text{-}R_{2\,(s)} \rightarrow M_{(s)} + R\text{-}R_{(g)}$$

in which M is a metal and R is an alkyl group. Thermal decomposition occurs in close proximity to the decomposition temperature of the precursor chosen. At the end of the heating treatment the organic part of the compound is removed by evaporation, and the solid metal is formed. As in the polyol process, and in general in the chemical reaction, the control on the thermal decomposition process can be performed by choosing the physiochemical parameters like temperature, pressure, concentration of reagents, and so on. The additives used like a polymer as stabilizers, allows to obtain a perfect control of the morphology and the dimensions of the nano-sized metal formed [56,63].

2.4.5. Thermal decomposition of organometallic compounds embedded into the polymer matrix

An inorganic phase (metal, metal oxide, metallic sulphide, etc.) finely divided (submicron or nanoscopic) can be uniformly generated within a polymer matrix by adding to it a thermolable organometallic precursor during processing. The characteristics required for the organometallic precursor are: (i) high solubility in the polymer, (ii) thermolysis at temperatures close to those of processing or otherwise compatible with the thermal stability of the polymer, (iii) generation of a volatile organic by-product that is completely eliminated during the process and (iv) reduced vapor pressure of the precursor which must decompose in solid or liquid phase but not in the gaseous state. It should also be pointed out that the use of polyolefin matrices (e.g. polyethylene, polypropylene, etc.) in the field of preparation of polymeric nanoparticles is the most complex situation, mainly for the difficulty of finding organometallic precursors soluble in these polymers. However, some organic salts and thermolable organometallic compounds possess such nonpolar nature to be similar to polyolefins and therefore be able to be dissolved in them in a large amount. A class of materials that has all the requirements to be used as precursor to generate metallic oxide and noble metal in polyolefins is represented by acetylacetonates (acac). Some of their coordinates complex as $Me(acac)_2$ e $Me(acac)_3$ are completely nonpolar and thus able to interact through non-binding interactions similar to those playing in the polyolefin polymers. These compounds can therefore be dissolved into the polyolefins and other apolar polymers even in high concentrations, leading to perfect solid solutions [64–66]. Many precursors commonly used in chemical vapor deposition (CVD) and epitaxial growth of atomic layers (ALE) are used in thermal decomposition processes. For example, the cyclopentadienyl derivatives are widely used because the organic part is sufficiently volatile at sufficiently low temperatures and therefore often decompose in vapor phase [45,62,63]. Many of these compounds are currently commercially available (e.g. many are supplied by Aldrich), so their use represents a virtually universal approach to the preparation of polymeric nanocomposites. The functional properties of the materials produced will depend of course on the type of charge generated in the polymer matrix.

2.4.6. Preparation method

The preparation of these polymeric nanocomposites involves two stages: the first is to provide the solid solution of the polymer precursor (blend precursor/polymer) by a wet-

way, and the second concern is the thermal treatment of this solid solution used to promote the decomposition of the organic part of the precursor for the inorganic phase production. The blend precursor/polymer is generally prepared by dissolving the thermoplastic polymer and precursor in a suitable solvent which is then removed by evaporation at room temperature (casting from solution). This approach is known as **"solvent mediated method"**, and it is one of the easiest techniques for the preparing blends. Organic solvents such as tetrahydrofuran (THF), methyl ethyl ketone (MEK), chloroform ($CHCl_3$), acetone ($(CH_3)_2CO$) are usually used since both precursor and the polymer dissolves in them. The solution containing the precursor is rapidly added to that of the polymer to form a mixture. After casting, the solvent has to be removed and the achieved blend is thermally treated. During the thermal treatment, the organic compound is decomposed and the inorganic phase embedded into the polymer matrix is formed. The poor mobility of metallic clusters into the polymer matrix reduces the possibility of aggregates formation, while the low diffusion value of atomic and molecular species and the high temperature used respectively, reduce the growth rate of the clusters and significantly increase the nucleation rate leading to the achievement of an nanoscopic phase uniformly dispersed and in an non-aggregated form.

2.5. References

[1] Satyanarayana V N T Kuchibhatla, A.S. Karakoti, D. Bera, S. Seal, One dimensional nanostructured materials, Prog. Mater. Sci. 52 (2007) 699–913. doi:10.1016/j.pmatsci.2006.08.001.

[2] S.M.H. Abtahi, Synthesis and characterization of metallic nanoparticles with photoactivated surface chemistries, 2013.

[3] H.S. Nalwa, Handbook of nanostructured materials and nanotechnology, Academic Press, 2000.

[4] P. Moriarty, Nanostructured materials, Rep. Prog. Phys. 64 (2001) 297–381. www.iop.org/Journals/rp (accessed June 24, 2017).

[5] Y. Wang, N. Herron, Nanometer-sized semiconductor clusters: materials synthesis, quantum size effects, and photophysical properties, J. Phys. Chem. 95 (1991) 525–532. doi:10.1021/j100155a009.

[6] C. Suryanarayana, Nanocrystalline materials, Int. Mater. Rev. 40 (1995) 41–64. doi:10.1179/imr.1995.40.2.41.

[7] S.C. Ray, J.W. Chiou, W.F. Pong, M.-H. Tsai, The Electronic Properties of Nanomaterials Elucidated by Synchrotron Radiation–Based Spectroscopy, Crit. Rev. Solid State Mater. Sci. 31 (2006) 91–110. doi:10.1080/10408430601044775.

[8] H.S. Nalwa, Handbook of nanostructured Materials and Nanotechnology - Electrical Properties, Academic Press, 2013. doi:10.1017/CBO9781107415324.004.

[9] S. Cuenot, C. Frétigny, S. Demoustier-Champagne, B. Nysten, Surface tension effect on the mechanical properties of nanomaterials measured by atomic force microscopy, Phys. Rev. B. 69 (2004) 1–5. doi:10.1103/PhysRevB.69.165410.

[10] P.C. Ray, Size and shape dependent second order nonlinear optical properties of nanomaterials and their application in biological and chemical sensing, Chem. Rev. 110 (2010) 5332–5365. doi:10.1021/cr900335q.

[11] H.T. Yang, C.M. Shen, Y.K. Su, T.Z. Yang, H.J. Gao, Y.G. Wang, Self-assembly and magnetic properties of cobalt nanoparticles, Appl. Phys. Lett. 82 (2003) 4729–4731. doi:10.1063/1.1586481.

[12] G.Y. Yurkov, A.S. Fionov, Y.A. Koksharov, V. V Koleso, S.P. Gubin, Electrical and magnetic properties of nanomaterials containing iron or cobalt nanoparticles, Inorg. Mater. 43 (2007) 834–844. doi:10.1134/S0020168507080055.

[13] V. Bérubé, G. Radtke, M. Dresselhaus, G. Chen, Size effects on the hydrogen

storage properties of nanostructured metal hydrides: A review, Int. J. Energy Res. 31 (2007) 637–663. doi:10.1002/er.1284.

[14] M.U. Niemann, S.S. Srinivasan, A.R. Phani, A. Kumar, D.Y. Goswami, E.K. Stefanakos, Nanomaterials for hydrogen storage applications: A review, J. Nanomater. 2008 (2008) 1–9. doi:10.1155/2008/950967.

[15] X. Chen, C. Li, M. Grätzel, R. Kostecki, S.S. Mao, Nanomaterials for renewable energy production and storage, Chem. Soc. Rev. 41 (2012) 7909. doi:10.1039/c2cs35230c.

[16] M. Faraday, Michael, The Bakerian Lecture: Experimental Relations of Gold (and Other Metals) to Light, Philos. Trans. R. Soc. London, Vol. 147, Pp. 145-181. 147 (1857) 145–181.

[17] H. Horvath, Gustav Mie and the scattering and absorption of light by particles: Historic developments and basics, J. Quant. Spectrosc. Radiat. Transf. 110 (2009) 787–799. doi:10.1016/j.jqsrt.2009.02.022.

[18] C.P. Poole, F.J. Owens, Introduction to nanotechnology, J. Wiley, 2003.

[19] S.M. Reimann, M. Manninen, Electronic structure of quantum dots, Rev. Mod. Phys. 74 (2002) 1283–1342. doi:10.1103/RevModPhys.74.1283.

[20] H.N. Daghestani, B.W. Day, Theory and applications of surface plasmon resonance, resonant mirror, resonant waveguide grating, and dual polarization interferometry biosensors, Sensors. 10 (2010) 9630–9646. doi:10.3390/s101109630.

[21] V.M. Rotello, Nanoparticles : building blocks for nanotechnology, Kluwer Academic/Plenum Publishers, 2004.

[22] C.C. Koch, Top-Down synthesis of nanoestructured materialas, mechanical and thermal processing methods., Rev. Adv. Mater. Sci. 5 (2003) 91–99.

[23] M.T. Swihart, Vapor-phase synthesis of nanoparticles, Curr. Opin. Colloid Interface Sci. 8 (2003) 127–133. doi:10.1016/S1359-0294(03)00007-4.

[24] T.Y. Shahid Pirzada, Method of producing nanoscale powders by quenching of vapors, 1996.

[25] C.M. Morales, A.M and Lieber, A laser ablation method for the synthesis of crystalline semiconductor nanowires, Science. 279 (1998) 208–11. doi:10.1126/science.279.5348.208.

[26] S.S. Makridis, E.I. Gkanas, G. Panagakos, E.S. Kikkinides, A.K. Stubos, P. Wagener, S. Barcikowski, Polymer-stable magnesium nanocomposites prepared by laser ablation for efficient hydrogen storage, Int. J. Hydrogen Energy. 38 (2013)

11530–11535. doi:10.1016/j.ijhydene.2013.04.031.

[27] M.E. Messing, K.A. Dick, L.R. Wallenberg, K. Deppert, Generation of size-selected gold nanoparticles by spark discharge — for growth of epitaxial nanowires, Gold Bull. 42 (2009) 20–26. doi:10.1007/BF03214902.

[28] N. Bazzanella, R. Checchetto, A. Miotello, Atoms and nanoparticles of transition metals as catalysts for hydrogen desorption from magnesium hydride, J. Nanomater. 2011 (2011) 1–11. doi:10.1155/2011/865969.

[29] W. Ouyang, J. Zhu, Catalyst-free synthesis of macro-scale ZnO nanonail arrays on Si substrate by simple physical vapor deposition, Mater. Lett. 62 (2008) 2557–2560. doi:10.1016/j.matlet.2007.12.051.

[30] Z. Yang, Y. Xia, X. Sun, R. Mokaya, Preparation and hydrogen storage properties of zeolite-templated carbon materials nanocast via chemical vapor deposition: Effect of the zeolite template and nitrogen doping, J. Phys. Chem. B. 110 (2006) 18424–18431. doi:10.1021/jp0639849.

[31] H.O. Pierson, Handbook of Chemical Vapor Deposition, Noyes Publications, 1999.

[32] Y. Guo, M. Wang, G. Xia, X. Ma, F. Fang, Y. Deng, L. Zhang, C. Wang, B. Tu, P.A. Webley, H. Wang, D. Zhao, Advanced H 2 - storage system fabricated through chemical layer deposition in a well-designed porous carbon scaffold, J. Mater. Chem. A. 2 (2014) 15168–15174. doi:10.1039/C4TA02917H.

[33] C.R. Bickmore, K.F. Waldner, D.R. Treadwell, R.M. Laine, Ultrafine Spinel Powders by Flame Spray Pyrolysis of a Magnesium Aluminum Double Alkoxide, J. Am. Ceram. Soc. 79 (1996) 1419–1423. doi:10.1111/j.1151-2916.1996.tb08608.x.

[34] B. Sakintuna, F. Lamari-Darkrim, M. Hirscher, Metal hydride materials for solid hydrogen storage: A review, Int. J. Hydrog. Energy. 32 (2007) 1121–1140. doi:10.1016/j.ijhydene.2006.11.022.

[35] M.Y. Song, S.H. Baek, J.L. Bobet, S.H. Hong, Hydrogen storage properties of a Mg-Ni-Fe mixture prepared via planetary ball milling in a H2 atmosphere, Int. J. Hydrogen Energy. 35 (2010) 10366–10372. doi:10.1016/j.ijhydene.2010.07.161.

[36] P. Palade, S. Sartori, A. Maddalena, G. Principi, S. Lo Russo, M. Lazarescu, G. Schinteie, V. Kuncser, G. Filoti, Hydrogen storage in Mg-Ni-Fe compounds prepared by melt spinning and ball milling, J. Alloys Compd. 415 (2006) 170–176. doi:10.1016/j.jallcom.2005.08.017.

[37] A. Zaluska, L. Zaluski, J.O. Ström-Olsen, Structure, catalysis and atomic reactions on the nano-scale: a systematic approach to metal hydrides for hydrogen storage,

Appl. Phys. A Mater. Sci. Process. 72 (2001) 157–165. doi:10.1007/s003390100783.

[38] T. Ichikawa, S. Isobe, N. Hanada, H. Fujii, Lithium nitride for reversible hydrogen storage, J. Alloys Compd. 365 (2004) 271–276. doi:10.1016/S0925-8388(03)00637-6.

[39] L. Schlapbach, a Züttel, Hydrogen-storage materials for mobile applications., Nature. 414 (2001) 353–358. doi:10.1038/35104634.

[40] I.P. Jain, C. Lal, A. Jain, Hydrogen storage in Mg: A most promising material, Int. J. Hydrogen Energy. 35 (2010) 5133–5144. doi:10.1016/j.ijhydene.2009.08.088.

[41] A. Zaluska, L. Zaluski, J.. Ström–Olsen, Nanocrystalline magnesium for hydrogen storage, J. Alloys Compd. 288 (1999) 217–225. doi:10.1016/S0925-8388(99)00073-0.

[42] B. Lim, M. Jiang, J. Tao, P.H.C. Camargo, Y. Zhu, Y. Xia, Shape-Controlled Synthesis of Pd Nanocrystals in Aqueous Solutions, Adv. Funct. Mater. 19 (2009) 189–200. doi:10.1002/adfm.200801439.

[43] Y. Yu, Y. Zhao, T. Huang, H. Liu, Shape-controlled synthesis of palladium nanocrystals by microwave irradiation, Pure Appl. Chem. 81 (2009) 2377–2385. doi:10.1351/PAC-CON-08-11-22.

[44] Y. Xiong, Y. Xia, Shape-Controlled Synthesis of Metal Nanostructures: The Case of Palladium, Adv. Mater. 19 (2007) 3385–3391. doi:10.1002/adma.200701301.

[45] D.-W. Lim, J.W. Yoon, K.Y. Ryu, M.P. Suh, Magnesium Nanocrystals Embedded in a Metal-Organic Framework: Hybrid Hydrogen Storage with Synergistic Effect on Physi- and Chemisorption, Angew. Chemie. 124 (2012) 9952–9955. doi:10.1002/ange.201206055.

[46] N. Bao, L. Shen, Y. Wang, P. Padhan, A. Gupta, A facile thermolysis route to monodisperse ferrite nanocrystals, J. Am. Chem. Soc. 129 (2007) 12374–12375. doi:10.1021/ja074458d.

[47] J. March, Advanced organic chemistry : reactions, mechanisms, and structure, Wiley, 1992.

[48] T. Sugimoto, Fine particles : synthesis, characterization, and mechanisms of growth, Marcel Dekker, 2000.

[49] J. Polte, Fundamental growth principles of colloidal metal nanoparticles – a new perspective, CrystEngComm. 17 (2015) 6809–6830. doi:10.1039/C5CE01014D.

[50] J. Cookson, The preparation of palladium nanoparticles, Platin. Met. Rev. 56 (2012)

83–98. doi:10.1595/147106712X632415.

[51] N. Toshima, T. Yonezawa, K.J. Klabunde, T. Ueda, H. Tsubomura, P. Stenius, A.I. Kirkland, D.J. Smith, M.D. Musick, M.J. Natan, Bimetallic nanoparticles—novel materials for chemical and physical applications, New J. Chem. 22 (1998) 1179–1201. doi:10.1039/a805753b.

[52] F. Kettemann, M. Wuithschick, G. Caputo, R. Kraehnert, N. Pinna, K. Rademann, J. Polte, Reliable palladium nanoparticle syntheses in aqueous solution: the importance of understanding precursor chemistry and growth mechanism, CrystEngComm. 17 (2015) 1865–1870. doi:10.1039/C4CE01025F.

[53] L. Nicolais, G. Carotenuto, Metal-Polymer Nanocomposites, 2005. doi:10.1002/0471695432.

[54] Y. Chen, D.-L. Peng, D. Lin, X. Luo, Preparation and magnetic properties of nickel nanoparticles via the thermal decomposition of nickel organometallic precursor in alkylamines, Nanotechnology. 18 (2007) 505703. doi:10.1088/0957-4484/18/50/505703.

[55] F. Rataboul, C. Nayral, M.-J. Casanove, A. Maisonnat, B. Chaudret, Synthesis and characterization of monodisperse zinc and zinc oxide nanoparticles from the organometallic precursor [Zn (C 6 H 11) 2] in recognition of his pioneering work in main group and organometallic chemistry, J. Organomet. Chem. 643 (2002) 307–312. doi:10.1016/S0022-328X(01)01378-X.

[56] G. Carotenuto, C.L. Hison, F. Capezzuto, M. Palomba, P. Perlo, P. Conte, Synthesis and thermoelectric characterisation of bismuth nanoparticles, J. Nanoparticle Res. 11 (2009) 1729–1738. doi:10.1007/s11051-008-9541-6.

[57] S. Matsuda, S. Ando, T. Sawada, Thin flexible polariser of Ag-nanoparticle-dispersed fluorinated polyimide, Electron. Lett. 37 (2001) 706. doi:10.1049/el:20010473.

[58] S. Porel, S. Singh, S.S. Harsha, D.N. Rao, T.P. Radhakrishnan, Nanoparticle-embedded polymer: In situ synthesis, free-standing films with highly monodisperse silver nanoparticles and optical limiting, Chem. Mater. 17 (2005) 9–12. doi:10.1021/cm0485963.

[59] S. Matsuda, S. Ando, Generation Behaviors of Optical Anisotropy Caused by Silver Nanoparticles Precipitated in Uniaxially Drawn Polyimide Films, Jpn. J. Appl. Phys. 44 (2005) 187–192. doi:10.1143/JJAP.44.187.

[60] S. Koizumi, S. Matsuda, S. Ando, Synthesis, Characterization, and Optical

Properties of Uniaxially Drawn and Gold Nanoparticle Dispersed Fluorinated Polyimide Films., J. Photopolym. Sci. Technol. 15 (2002) 231–236. doi:10.2494/photopolymer.15.231.

[61] G. Wilke, Organo transition metal compounds as intermediates in homogeneous catalytic reactions, Pure Appl. Chem. 50 (1978) 677–690. doi:10.1351/pac197850080677.

[62] H. Kunkely, A. Vogler, Optical properties of bis(cyclopentadienyl)magnesium: excimer-type luminescence of the bis(cyclopentadienyl) ligand frame, J. Organomet. Chem. 689 (2004) 2940–2943. doi:10.1016/j.jorganchem.2004.05.048.

[63] K.-J. Jeon, H.R. Moon, A.M. Ruminski, B. Jiang, C. Kisielowski, R. Bardhan, J.J. Urban, Air-stable magnesium nanocomposites provide rapid and high-capacity hydrogen storage without using heavy-metal catalysts, Nat. Mater. 10 (2011) 286–290. doi:10.1038/nmat2978.

[64] B. Jankoviç, S. Mentus, A kinetic study of the nonisothermal decomposition of palladium acetylacetonate investigated by thermogravimetric and x-ray diffraction analysis determination of distributed reactivity model, Metall. Mater. Trans. A Phys. Metall. Mater. Sci. 40 (2009) 609–624. doi:10.1007/s11661-008-9754-4.

[65] B. Janković, S. Mentus, Model-fitting and model-free analysis of thermal decomposition of palladium acetylacetonate [Pd(acac)2], J. Therm. Anal. Calorim. 94 (2008) 395–403. doi:10.1007/s10973-008-9118-8.

[66] A.L. Willis, Z. Chen, J. He, Y. Zhu, N.J. Turro, S. O'Brien, Metal acetylacetonates as general precursors for the synthesis of early transition metal oxide nanomaterials, J. Nanomater. 2007 (2007). doi:10.1155/2007/14858.

Chapter 3

Synthesis and Characterization of Palladium Clusters by Polyol Reduction of $[PdCl_4]^{2-}$ Ions[2]

3.1. Introduction

Palladium nanoparticles have important applications in different industrial fields (for example, catalysts, electrically conductive inks, materials for hydrogen-storage, sensors, etc.) [1–4]. In particular, the nanostructured palladium is one of the most investigated model system for understanding the hydrogen interaction with metal surfaces. Despite the low hydrogen storage capacity of palladium (the highest observed hydrogen uptake was ca. 0.7 wt%), the study of the processes involved in the nanoclusters production allowed to understand the general approach to be used for the nanostructured H_2-storage materials preparation. In addition, the palladium plays an important role in the H_2-dissociative adsorption on its surface, followed by H atoms diffusion to the support on which it is deposited ("spillover mechanism", see Figure 1.18). Their physicochemical properties strictly depend on their size. For that reason, chemical methods aimed at achieving tailored nanoparticles are required. Many studies on the preparation of palladium particles, nanoparticles, and clusters (i.e., nanoparticles with a size of few nanometers) are available in the literature [5–15]. Under uncontrolled conditions "palladium black", which is

[2] This chapter is based on the results published in**:** L.Schiavo et al; *"**Synthesis of Palladium Clusters by Reduction of K_2PdCl_4 with Ethylene Glycols**"*. IEEE NANO 2015, Proceedings of the 15th International Conference On Nanotechnology**,** 27-30 July 2015, Roma, Italy. DOI 10.1109/NANO.2015.7388979

L. Schiavo et al; *"**Structural Characterizations of Palladium Clusters Prepared by Polyol Reduction of $[PdCl_4]^{2-}$ Ions**.J. Anal Methods Chem.*Vol.2016 (2016), Article ID 9073594, 6 pages

agglomerated of fine palladium particles (average size less than 0.1μm), is produced by using the "**polyol-process**" approach. This method involves the chemical reduction of a metal salt by refluxing it in a liquid polyol. Among the others, ethylene glycol (EG), glycerol (GLY), diethylene glycol (DEG), and triethylene glycol (TEG) are at the same time discrete solvents for the precursor and good dispersing medium for the resulting nanoparticles [5–7]. Palladium particles in the submicrometer range were synthetized at low temperature (below 0°C) by using palladium(II) tetrammine complex as precursor and hydrazine hydrate as auxiliary reducing agent [6]. In the same conditions, submicrometer-sized monodisperse and quasi-spherical palladium particles with an average diameter of ca. 0.15μm were obtained by changing the type of polyol [7]. It was also noted that the use of stabilizers makes possible to obtain shape-controlled palladium particles on a nanoscopic scale [5–8]. The chemical synthesis of palladium nanoparticles with different stabilizers as, for example, organic ligands, salt/surfactants, polymers, and dendrimers allows to obtain monodispersed nanosized palladium with well-controlled particle size and shape in the 1-100nm range [13]. Poly-(N-vinyl-2-pyrrolidone) (PVP) is one of the most investigated polymers for stabilize metal nanoparticles [11–16]. It is very interesting as achelating agent able to leads to very small particles. The morphology of the palladium nanoparticles obtained in presence of PVP can be finely tuned by changing the reaction conditions like temperature, reaction time, metallic precursor type, etc. [11].

In this chapter is described the palladium clusters preparation with a very simple synthesis technique based on the polyol reduction of K_2PdCl_4 in ethylene glycol and in air at mild temperature conditions, using PVP as polymeric surface stabilizer. The reaction mechanism involved in the palladium ions reduction is reported in Figure 3.1.

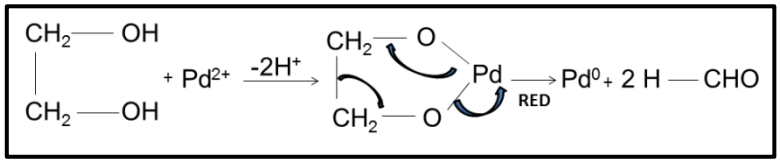

Figure 3.1 Palladium reduction mechanism

From this synthesis, polymer-embedded palladium clusters of quasi-spherical shape have been obtained. The experimental conditions (the temperature, the type/amount of salt, the concentrations, etc.) have been selected to reduce completely the precursor and get extremely small clusters. The structure and the surface oxidation state of palladium clusters

were characterized in order to evaluate the effects of a non-inert atmosphere on their synthesis. The techniques used for the palladium clusters characterization are described in the Appendix B.

3.2. Experimental details

The experimental section consists of three parts: the first part concern the study of the chemical reduction process of different palladium salts in EG, without the use of the surface stabilizer. This study is necessary to find a suitable precursor able to completely dissolve in the polyol liquid before its reduction. In this way, the dissolution and the reduction processes can be consequential and not concomitant. The choice of a suitable salt allows to have a good control on nucleation and growth steps. The dissolution of palladium salts like palladium (II) nitrate hydrate $Pd(NO_3)_2$ x H_2O (Aldrich), Palladium(II) chloride $PdCl_2$(Aldrich, 99%), Palladium(II) acetyl-acetonate $Pd(acac)_2$ (Aldrich, 99.0%) and Potassium tetrachloropalladate(II) K_2PdCl_4 (Aldrich, 99.99%) in EG was investigated. Every salt has been used without any purification. A solution of every salt was prepared. Every solution was stirred and heated at given temperature, ranging from room temperature to 90°C, in any case lower than the boiling point of the polyol. During the process, the solution color changed from yellow or light-brown to black, it was an indication of the palladium ions transformation into palladium clusters.

The second part of the experimental section concerns the preparation and the characterization of nanocomposites palladium-based by polyol reduction of $[PdCl_4]^{2-}$ ions in PVP. The schematic representation of nanocomposite sample preparation process is shown in Figure 3.2. The preparation of palladium nanocomposites involve the dissolution of the poly(N-vinyl-2-pyrrolidone) (Aldrich, $\overline{Mw}$ =10,000 $gmol^{-1}$) in EG (Aldrich, 99.0%) (Figure 3.2, 1°step). The polymeric solution was placed in a thermostatic bath at temperatures ranging from 70°C to 90°C for 120 minutes in air. Separately, a small volume of a concentrated K_2PdCl_4 (Aldrich, 99.99 %) solution in EG was prepared (Figure 3.2, 2°step) and it was quickly added to the PVP/EG solution at chosen temperature and room atmosphere under vigorous stirring. The PVP concentration in ethylene glycol was of 30mM and the molar ratio Pd(II):PVP (the repeating unit) was 1:10 [7]. During the reaction time, the solution color changed from light-brown to black (Figure 3.2) while the palladium clusters formed [14]. After a thermal annealing of 120 minutes the solution was cast into a large amount of pure acetone (Aldrich) and the system was left at room

temperature for 12h. Subsequently, the acetone supernatant was removed and replaced with fresh acetone (100mL), and the system was treated in bath-sonication for 30 minutes. This washing procedure was repeated three times. The PVP completely flocculated from this non-solvent liquid (ethylene glycol/acetone mixture), co-precipitating the coordinated palladium clusters. Different reaction temperatures have been investigated (70°C, 80°C and 90°C). The palladium clusters obtained by reduction at 90°C for 120 minutes were quite monodispersed and had an average diameter of ca.2.8 nm. The nano-sized palladium particles (free from aggregates and with a polyhedral shape) were isolated in a polymer-embedded form.

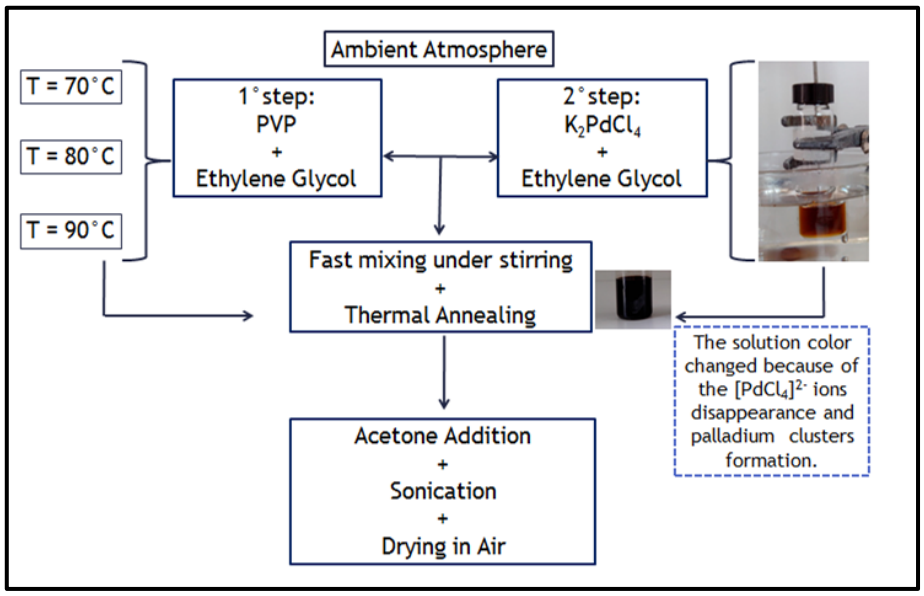

Figure 3.2 Schematic representation of nanocomposite preparation process by polyol reduction of $[PdCl_4]^{2-}$ ions in PVP

The third part of this chapter concerns the complete characterization of the palladium nanocomposites prepared at 90°C for 2h. The structural analysis of PVP-embedded palladium clusters was performed by using different microscopy and spectroscopy techniques, such as the transmission electron microscopy (TEM), the scanning electron microscopy (SEM) and the X-ray powder diffraction (XRD). The characterization of the elements and their distribution was performed by using both the energy dispersive X-ray microanalysis (EDS-SEM) and X-ray Photoelectron Spectroscopy (XPS) analysis. The last analysis was used also to identify the chemical state of the palladium nanocrystals produced. Other techniques, such as the thermogravimetric analysis (TGA) or UV-Vis spectroscopy (UV) for the phase characterization, were used. The aforementioned techniques are described in the Appendix B.

3.3. Experimental results

3.3.1. Chemical reduction without surface stabilizers

The study of the chemical reduction process of different palladium salts in EG, without the use of the surface stabilizer, has been performed. The starting salts used were: palladium(II) nitrate hydrate ($Pd(NO_3)_2 \cdot xH_2O$, Aldrich), palladium(II) chloride ($PdCl_2$, Aldrich, 99%), palladium(II) acetyl-acetonate ($Pd(acac)_2$, Aldrich, 99.0%) and potassium tetrachloropalladate(II) (K_2PdCl_4 , Aldrich, 99.99%). The salts were used without any purification. Every salt have been dissolved separately in ethylene glycol (Aldrich, 99.8%).

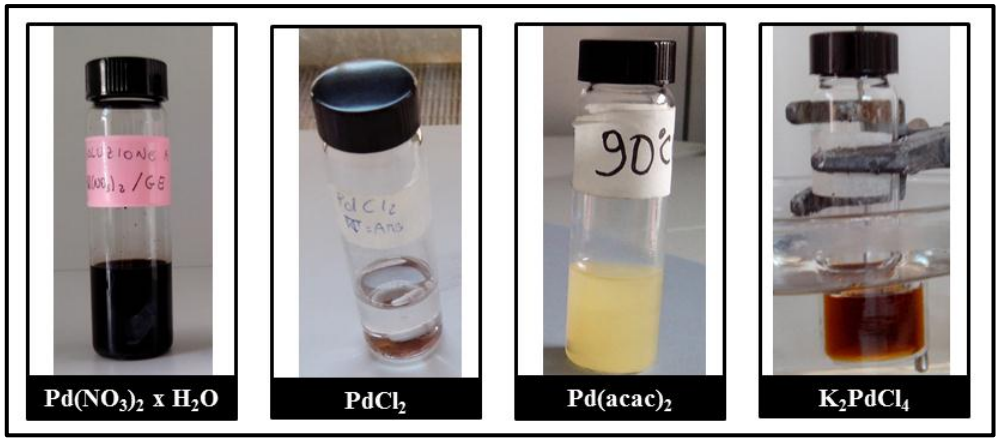

Figure 3.3 Solubility tests on different palladium salts

The $Pd(NO_3)_2xH_2O$ (Figure 3.3) was the first precursor studied. The alcoholic solution was stirred at room temperature for few minutes, while nothing happened. Only when the solution was heated at a temperature ranging from 40°C to 60°C, the reduction quickly happened. At this point, a black solution with a powder on the bottom of the bottle appeared. The fast reduction suggests that the dissolution and reduction processes were occurred at the same time, making difficult the control on the nucleation and growth of the nanoparticles produced. For this reason, another salt, the $PdCl_2$, was investigated. Unlike was been happened for $Pd(NO_3)_2$ x H_2O, the palladium(II)chloride was resulted completely insoluble in EG, both at room or at a higher temperature (Figure 3.3). In order to improve the dissolution process, the $PdCl_2$/EG solution was treated in a bath-sonication for 30 minutes. However, also in this case the $PdCl_2$ non-polar nature avoids its complete dissolution in EG. Successively, an organic salt of palladium, the $Pd(acac)_2$, was tested. The photographic images related to the temporary evolution process of $Pd(acac)_2$ dissolution in EG at 90°C during the time, is reported in Figure 3.4. Such salt was

completely and quickly dissolved at low temperature (60°C) in the EG, giving a light yellow solution (Figure 3.4, 1). After formation, the color of the solution remained stable, at room temperature. This solution was then heated at different temperature (70°C, 80°C and 90°C) for different times (60, 120 and 180 minutes). The reduction at 90°C for 120 minutes led to a gradual changing of the salt color during the time up to become black. It meaning that a complete reduction was occurred (Figure 3.4, 4). After a thermal annealing of 120 minutes, the solution was washed three times with acetone and dried at room temperature. Palladium powders have been obtained.

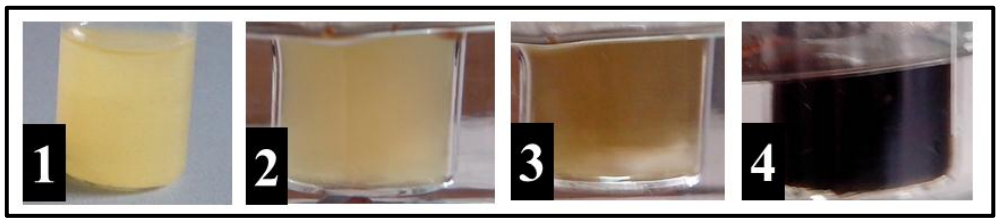

Figure 3.4 Photographic images of the temporary evolution process of the $Pd(acac)_2$ dissolution in EG performed at 90°C at different reaction times: t = 0s (1), t = 600s (2), t = 1800s (3) and t= 3600s (4)

The SEM micrographs of palladium powder are shown in Figure 3.5. The palladium powder obtained by chemical reduction of $Pd(acac)_2$ in EG at 90°C have shown the formation of a Pd spongy structure (Figure 3.5), made of smaller palladium nanoparticles of about 5nm (Figure 3.5, D) tightly sintered together (Figure 3.5, A-D). This sintering process was probably driven by a minimization of surface area that leads to a decreasing in surface energy. This happens when two particles coalesce [17]. The chemical composition evaluated by using EDS-SEM measurements has revealed that the powder was mainly composed of palladium (42 wt%), carbon (39 wt%), oxygen (7 wt%) and traces of other elements, coming from the reagents. The micrographs images obtained by overlapping the signals coming out from back-scattered electrons (BS - yellow) and secondary electrons (SE - green) (Figure 3.5, E and F) underline the presence of two different phases. In particular, it is quite evident the presence of a phase, probably an organic phase, that covers the palladium sponge. The organic phase was probably due to the presence of a monoalkoxide specie ($-OCH_2CH_2OH$) formed on Pd [18], coming out from the precursor. The presence of this unremoved organic phase was strongly unsuitable for the nanoparticles preparation. For that reason, a complex salt of palladium, the potassium tetrachloropalladate(II) K_2PdCl_4 was investigated. This salt was completely and fastly

dissolved in EG at room temperature (Figure 3.3). The solution becomes brown and its color, at room temperature, unchanged with time. This solution was heated at 90°C and a gradual color changing was observed. After 120 minutes the black color was stable, meaning that a complete reduction was occurred. The morphology of palladium powders is shown in Figure 3.6.

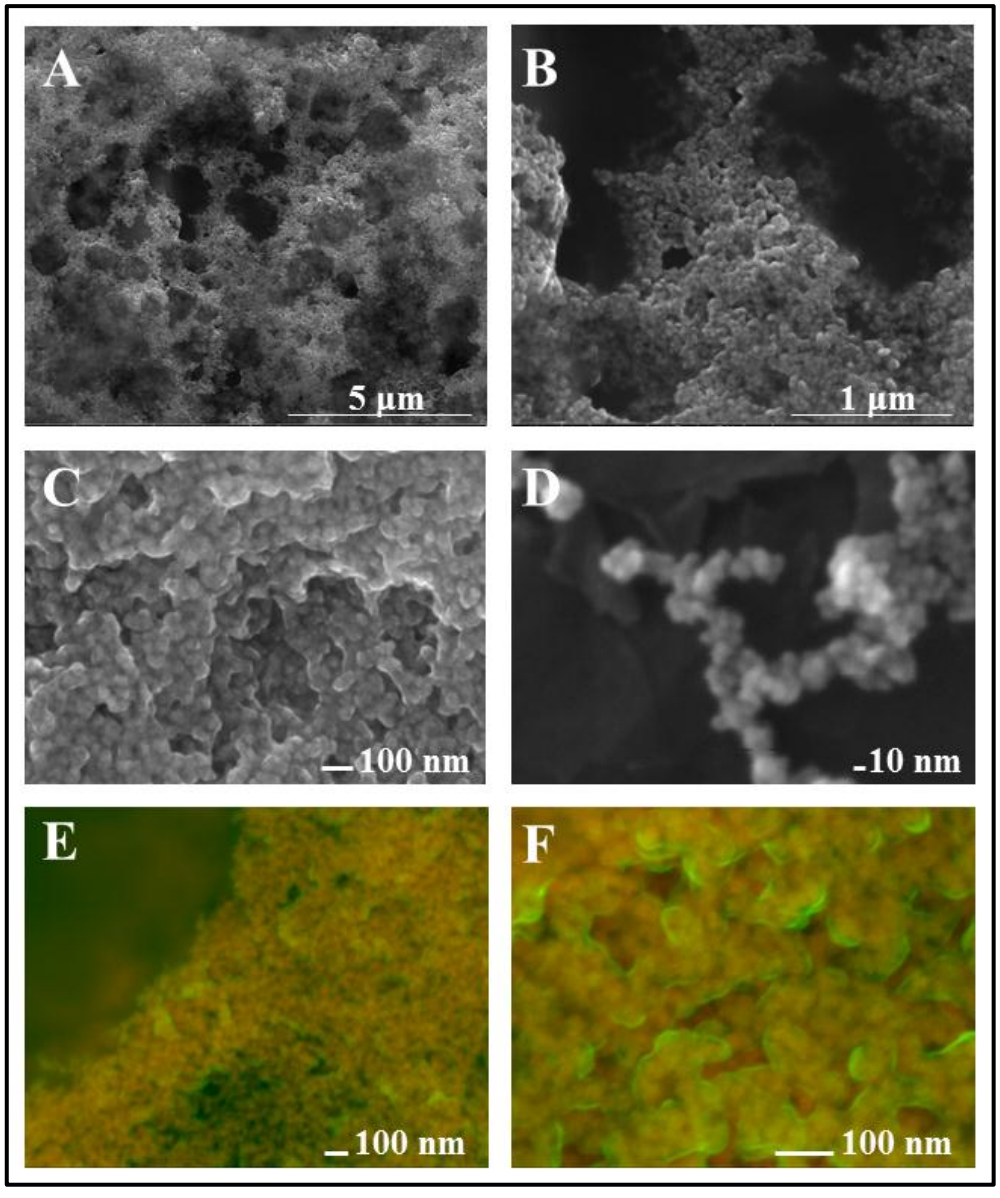

Figure 3.5 SEM micrographs of palladium powder obtained by chemical reduction of $Pd(acac)_2$ in EG at 90°C (A-D) and micrographs images obtained by collecting back-scattered electrons (yellow) and secondary electrons (green) (E,F).

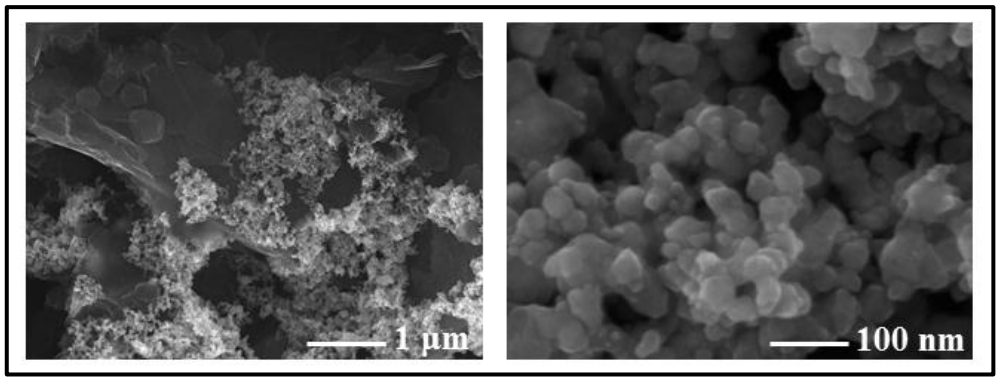

Figure 3.6 SEM micrographs of palladium powder obtained by chemical reduction of K_2PdCl_4 in EG at 90°C

Like in the $Pd(acac)_2$ case, a high palladium spongy structure was obtained, but with a composition made mainly of nanostructured palladium (90 wt%) of a size ranging between 30-40 µm. The nanoparticles synthesis was probably due to mechanisms of atomic diffusion in the solid phase. The thermal stability of K_2PdCl_4 salt was evaluated by thermogravimetric analysis (TGA), heating the sample under fluxing air and nitrogen atmosphere at a rate of 10°C/min. The TGA thermogram was reported in Figure 3.7.

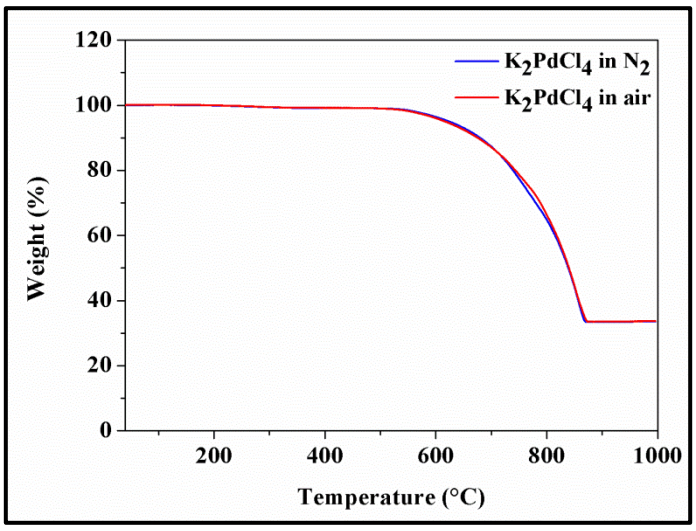

Figure 3.7 TGA thermogram of K_2PdCl_4 salt performed at rate of 10K/min in air and nitrogen atmosphere

The TGA supplied important information about the decomposition temperature, which resulted to be about 530°C both in air and under nitrogen atmosphere. The decomposition temperature was much higher than the reaction temperature (90°C). This suggests that for the palladium powder formation a redox process was involved. The residual weight at the

end of TGA tests was of 32.60 wt%, which exactly corresponds to the Pd weight percentage contained in a K_2PdCl_4 stoichiometric salt (e.g. salt does not contain impurities). The amount of Pd wt% in K_2PdCl_4 palladium salt is calculated by the ratio of the Pd atomic weight (m_a = 106,42u) and the K_2PdCl_4 molecular weight (Mw = 326,42 g/mol), per cent. The chemical reduction process of different palladium salts in EG was investigated. Nanostructured palladium powders were prepared by using potassium tetrachloropalladate(II) (K_2PdCl_4) as a source of palladium nanoparticles. Nanocomposites palladium based, embedded in PVP polymer matrix, will be prepared by using this salt.

3.3.2. Chemical reduction with surface stabilizers

In order to evaluate the temperature effects on palladium nanoparticles produced, three different temperatures, 70°C, 80°C and 90°C, were investigated. The morphology and the particles size distribution of three different Pd/PVP samples are reported in Figure 3.8. In particular, in Figure 3.8, A, C and E are reported the Pd/PVP nanocomposites micrographs prepared at 70°C, 80°C and 90°C, respectively. As it is visible, the Pd/PVP nanocomposites prepared at 70°C and 80°C presents a non-homogeneous particle size distribution of the clusters, with an average size of about 4nm. The chemical reduction of $[PdCl_4]^{2-}$ ions performed at 90°C for 120 minutes produced mono-dispersed clusters [14,19], of a quasi-spherical shape. Such crystals had an average size of about 3nm (see Figure 3.8, E).

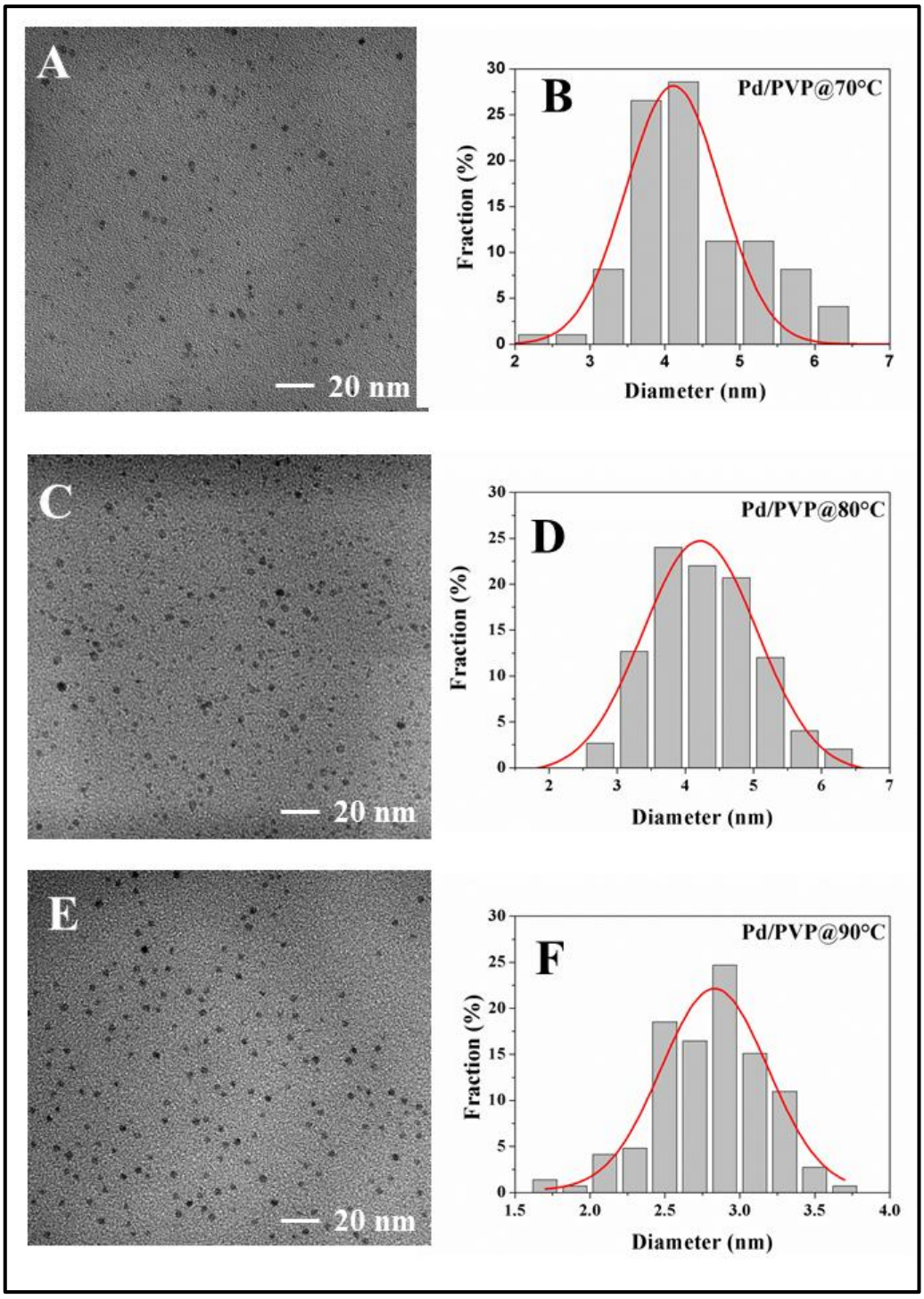

Figure 3.8 TEM-micrographs of palladium clusters produced by reduction of $[PdCl_4]^{2-}$ at 70°C (A), 80°C (C), and 90°C (E) and the corresponding particle size distributions (B,D and F)

The XRD pattern of the palladium clusters obtained in the above experimental conditions is shown in Figure 3.9. A higher and broader peak at 2θ = 40.1°, corresponding to the (111) of palladium diffraction pattern, was observed [9,14,19]. According to JCPDS-461043 files, such diffraction peak can be well-indexed to face-centered cubic (fcc) of Pd, indicating that the as-prepared Pd clusters have a high purity and high crystallinity. The

Pd/PVP nanocomposites prepared at 70°C, 80°C showed other three peaks at 29.6º, 30.8º and 43.2º, respectively. These peaks can be attributed to a salt reagent not completely converted. These peaks were absent in the Pd/PVP nanocomposite prepared at 90°C. The mean particles size for the Pd/PVP nanocomposites prepared at 90°C for 120 minutes estimated by the Scherrer's equation on the broader peak at 2θ = 40.1º resulted of about 5nm, which is consistent with TEM measurement.

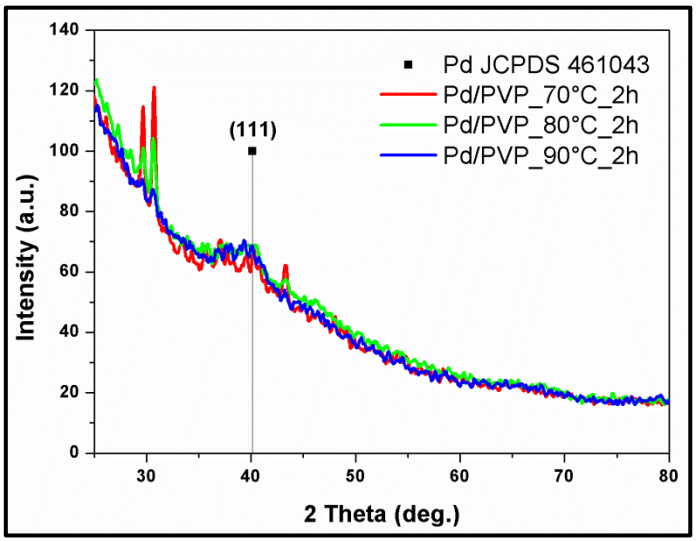

Figure 3.9 XRD spectra of palladium clusters produced by reduction of $[PdCl_4]^{2-}$ at 70°C (red curve), 80°C (green curve) and 90°C (blue curve).

XPS was used to investigate the oxidative state of palladium phase. X-ray Photoelectron Spectroscopy (XPS) has been carried out in a UHV apparatus equipped with an X-ray source (Mg Kα photon at 1253.6eV). In order to perform XPS analysis, the sample powders were dispersed in isopropyl alcohol, dropped on a Si(100) substrate previously cleaned in a sonication bath of trichloroethylene-acetone-isopropyl alcohol, and left to dry in air for 24 hours, before being inserted into the UHV chamber. The wide-scan BE spectra (not shown here) of the Pd clusters embedded in PVP evidence the nature of all contained chemical species: C, O, N and a very small contribution from Pd. All core levels are shifted towards higher BE, caused by charging effects during the analysis due to the presence of the non-conducting polymeric phase that gives to all core levels different shifts from one sample to the others. Figure 3.10 shows the Pd3d region for a PVP film and PVP-embedded Pd nanoparticles.

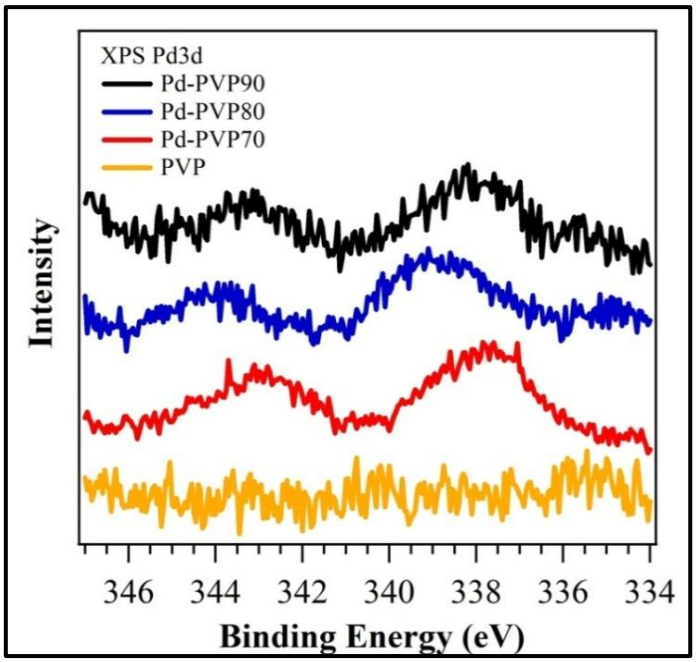

Figure 3.10 XPS Pd3d spectra of Pd clusters embedded in PVP, produced by reduction of $[PdCl_4]^{2-}$ at 70°C, 80°C and 90°C, and of a pure PVP sample for reference.

Pd3d core level is located at 337.0 – 339.0eV, with a spin-orbit splitting of 5.27eV. Its intensity is very low, suggesting that the photoemission signal from the nanoparticles strongly reduced by the presence of PVP [20]. The Pd3d peak position can be rescaled, according to the charging effects, to lower BE thus suggesting that the as-prepared Pd nanoparticles are in a zero-valent chemical state rather than oxidized [20,21]. The atomic percentage of each chemical species has been evaluated from the core level intensities and for Pd it ranges from 0.10 to 0.20%, a value close to the XPS sensitivity limit. Considering all the chemical species, the relative percentages have been reported in Table 3.1. The C, O and N atomic percentages are in agreement with the reference sample for the nanoparticles obtained at 90°C, while an increased content of carbon is found for the other preparation conditions, probably due to the variable content of monoalkoxide species on the palladium nanoparticles surface [18].

Samples	**Atomic percentages of C, O ,N and Pd**			
	% C	**%O**	**%N**	**%Pd**
Pd-PVP_90°C	74.9	12.0	13.1	0.1
Pd-PVP_80°C	84.3	11.2	4.4	0.1
Pd-PVP_70°C	88.2	11.8	7.7	0.2
PVP	73.4	10.5	16.1	0.0

Table 3.1 Atomic percentage of chemical species by XPS analysis

3.3.3. Structural Characterizations of Palladium Clusters Prepared by Polyol Reduction of $[PdCl_4]^{2-}$ Ions

From previous experimental results it has been found that the chemical reduction of $[PdCl_4]^{2-}$ ions at 90°C for 120 minutes produced mono-dispersed clusters with very small average size of ca.3nm (Figure 3.8, E and F), confirmed by the presence of a broad peak located at 2θ = 40.1°, corresponding to the (111) lattice plane of palladium diffraction pattern (according to JCPDS-46104) (see Figure 3.9). The broad shape and the low intensity of such peak can be attributed to the extremely small crystal size. The mean particle size estimated by the Scherrer's equation [22] applied on (111) Pd diffraction peak (see Figure 3.9) was resulted to be ca. 5nm, which consistent with TEM measurements. Starting from these results, a deep investigation of this Pd/PVP nanocomposite prepared at 90°C was performed, with many others characterization. The starting colloidal solution was also analyzed. The temporal evolution of UV-Vis absorption spectra of the reactive system is reported in Figure 3.11. The freshly prepared solution was promptly placed in the UV-Vis spectrophotometer, previously thermostated at 90°C, to evaluate the variation of the absorption peaks during the reaction.

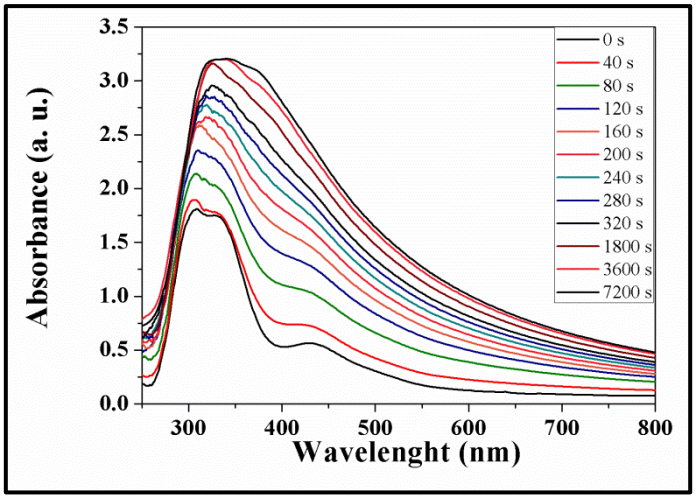

Figure 3.11 UV-Vis absorption spectra at different reaction times during the reduction of $[PdCl_4]^{2-}$ at 90°C

As shown in Figure 3.11, at the beginning of the reaction (0-40s curves) two strong characteristic absorption peaks at ca.305nm and 330nm and a shoulder at ca. 440nm are present, corresponding to $[PdCl_4]^{2-}$ ions [8,15]. It can be seen that no significant change in

the absorption peaks was observed after 40s. When the reaction proceeded for 80s, the peaks at 305nm and 330nm slowly begin to shift at higher wavelengths, and the shoulder at ca. 440nm begins to disappear. The absorption spectrum exhibited a typical light-scattering phenomenon, thus indicating the palladium nanoparticles formation. The light-scattering is further enhanced with time, due to the increase of Pd nanoparticles, reaching an intensity maximum after 1800s. At this time the two peaks at 305nm and 330nm were shifted at 332nm and 355nm respectively, and the shoulder at ca. 440nm disappears. During the process, the solution color changed from light-brown to black because of the $[PdCl_4]^{2-}$ ions disappearance and palladium clusters formation, indicating that the reduction process was complete after 240s. After this time, only a rising of the absorbance baseline was observed, due to the scattering of the palladium nanoparticles formed into the polymer.

The thermal behavior of Pd/PVP sample in air was then investigated. The thermogram of a Pd/PVP sample is shown in Figure 3.12. Most of the weight loss is in the range 400°C- 460 °C and the residual weight is of 0.6 wt% (see inset in Figure 3.12). The amount of residual weight that corresponds to the synthetized Pd(0) phase, is higher than the expected theoretical value (0.1wt.%), probably due to the PVP loss during the washing cycles and to traces of impurities coming from K_2PdCl_4. The expected theoretical value was calculated using the initial weight of the K_2PdCl_4 salt and of PVP, used for the nanocomposites preparation. According to the stoichiometric amount of Pd present in K_2PdCl_4 (32.60% by weight), it was possible to calculate the amount of palladium present in the initial mass of salt (of about 0.085g). The initial PVP amount was of about 24.4g. The synthetized Pd(0) phase theoretical value was calculated as weight ratio of the palladium present in the initial mass of salt on the total weight of the sample (palladium weight and polymer weight).

The morphology of the residual Pd (of 0.6 wt%), is shown in Figure 3.13 A,B and C. A continuous metallic structure, generated by coalescence/sintering of adjacent palladium clusters after PVP removal, is clearly visible. The chemical composition of the residual Pd after the TGA tests was determined by using the energy-dispersive X-ray spectroscopy (EDS-SEM) (Figure 3.13,D). This material was mainly composed of oxygen and palladium together with traces of other elements, coming from the reagents.

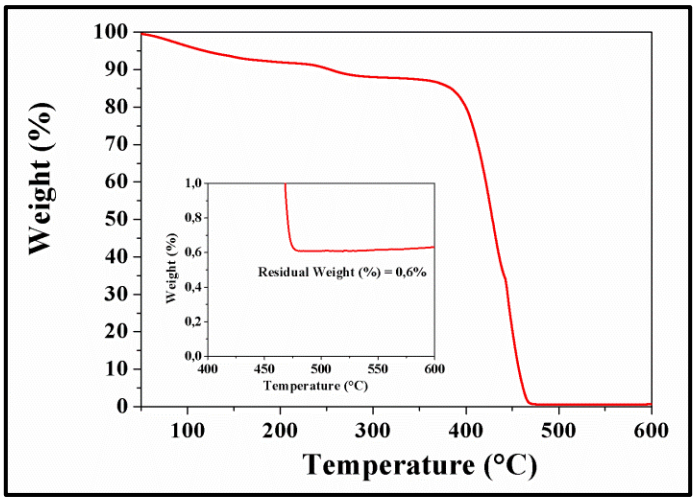

Figure 3.12 Thermogram of palladium clusters embedded in PVP produced by reduction of $[PdCl_4]^{2-}$ at 90°C performed at rate of 10K/min in air

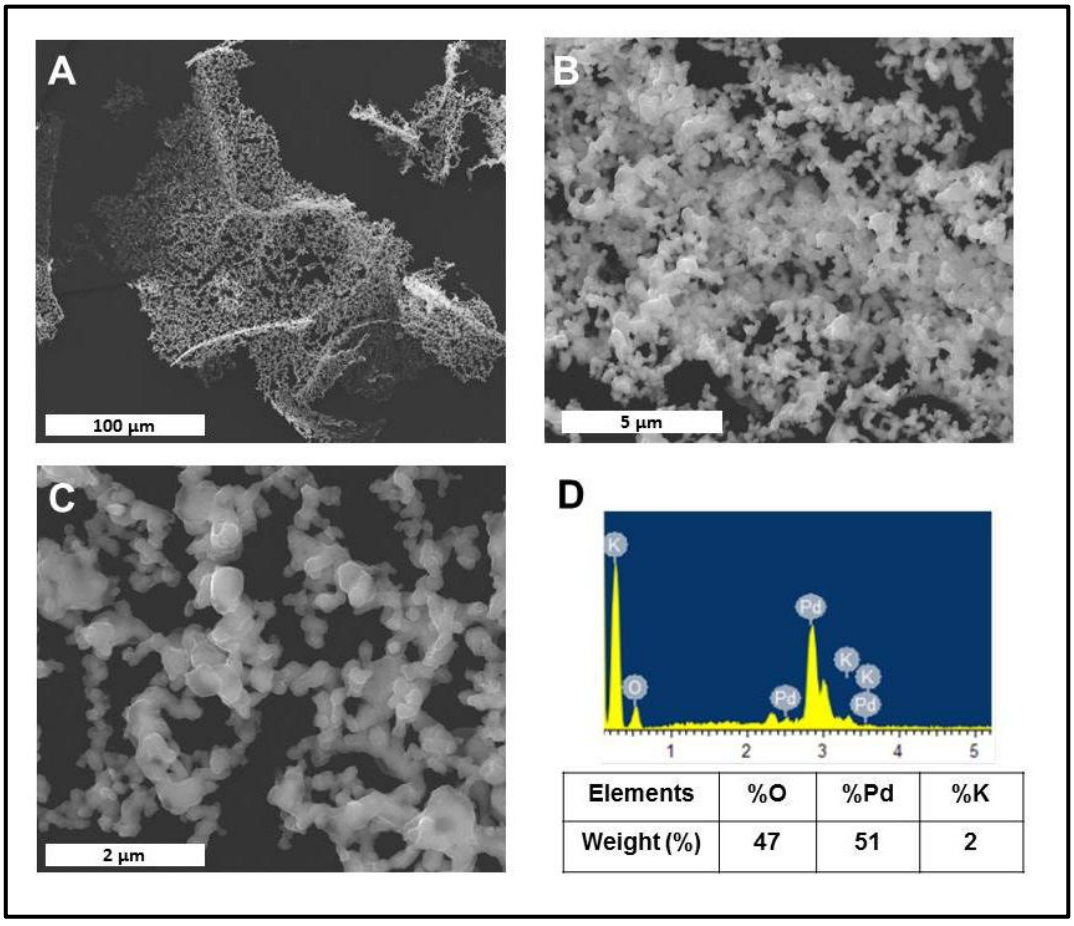

Elements	%O	%Pd	%K
Weight (%)	47	51	2

Figure 3.13 SEM micrographs of the residual palladium clusters obtained by TGA tests in air (A, B and C) and the corresponding compositional EDS-SEM analysis (D)

XPS was employed to investigate the chemical state of the palladium nanoparticles and qualify the interaction between PVP molecules and palladium atoms during the formation of PVP-capped palladium nanoparticles. Figure 3.14 shows the wide binding energy (BE) range spectrum for the PVP-capped Pd nanoparticles compared to the PVP reference spectrum, putting in evidence the presence of all the expected chemical species, that are C, O, N (both Auger emission and core levels are clearly identifiable) and a very weak contribution from Pd3d core level. All core levels are shifted towards higher BE, a phenomenon that is related to charging effects during the analysis due to the presence of the polymeric not-conductive material [23]. Such a shift can be evaluated to be about +2.5eV from the main C1s component, that should be at 285eV.

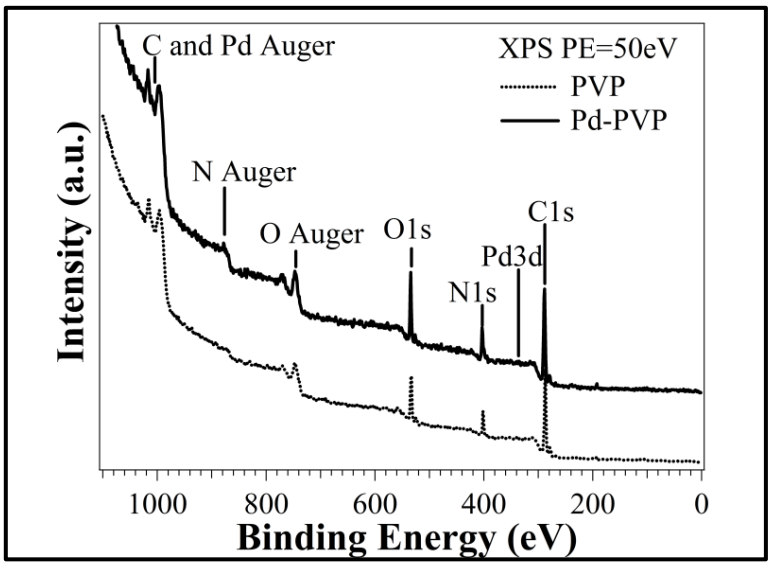

Figure 3.14 XPS wide-range spectra of Pd nanoparticles embedded in PVP and of a pure PVP (reference)

Figure 3.15 shows the Pd3d region for a PVP film and PVP-capped palladium nanoparticles. Pd3d core level is located at 338.0eV, with a spin-orbit splitting of 5.27eV. Taking into account charging effects, the peak position for Pd3d can be rescaled to lower BE suggesting that the as-prepared Pd nanoparticles are in a metallic chemical state rather than oxidized [20,21,24].

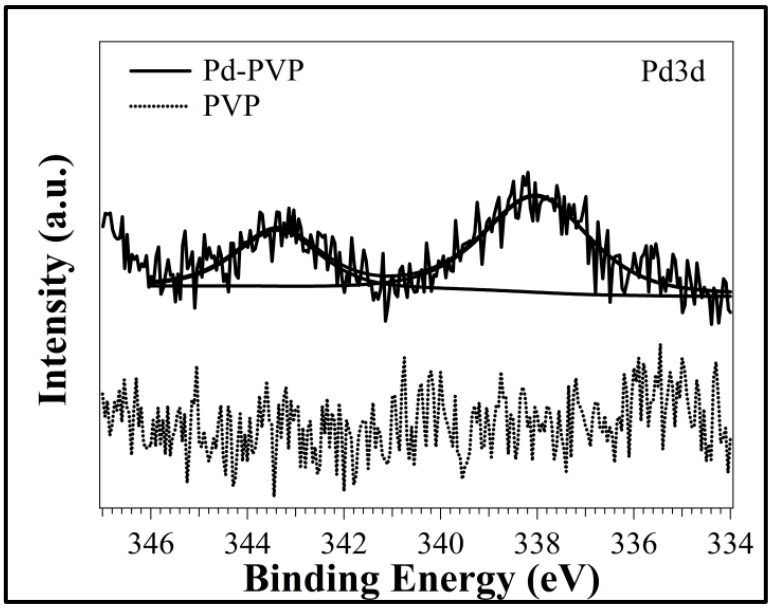

Figure 3.15 XPS Pd 3d spectra of Pd nanoparticles in PVP and of a pure PVP sample for reference.

The Pd core level intensity is very low, as it is shown with the comparison of a PVP sample without Pd particles (Figure 3.15). Such a low intensity can be probably related also to the presence of the capping PVP layer, leading to a strong photoemission signal decrease as the escape depth of Pd photoelectrons is in the range of few nanometers [25]. The surface atomic percentage of each chemical species has been evaluated from core level intensity and for Pd is 0.1 %, a value close to the XPS sensitivity but in agreement both with the low density of the nanoparticles observed by the TEM images and with energy-dispersive X-ray spectroscopy (EDS-SEM), (Table 3.2).

Elements	Weight (%) from EDS	Atomic (%) from EDS	Atomic (%) from XPS
%C	76.7	82.0	76.1
%O	22.1	17.8	12.4
%Pd	1.2	0.1	0.1

Table 3.2 Weight and atomic percentages obtained by EDS-SEM and XPS analysis for palladium clusters embedded in PVP produced by reduction of $[PdCl_4]^{2-}$ at 90°C.

Considering other chemical species, the following percentages have been found: 76.1 % for C1s, 12.4% for O1s and 11.4% for N1s, in good agreement with the chemical formula of PVP showing theoretical atomic percentages of 75.0% for C, 12.5% for O and 12.5% for N.

3.4. Conclusion

Extremely small and monodispersed palladium clusters (average diameter of about 2.6nm by TEM) have been produced by reduction of $[PdCl_4]^{2-}$ ions with ethylene glycol at 90°C, without inert atmosphere and in presence of PVP as surface stabilizer. A very simple synthetic approach has been proposed. The study was verified by a complete characterization of Pd clusters with different techniques, aimed to study their properties from different points of view. A complete structural/morphological characterization of the chemical composition and Pd valence state was performed. The experimental results show that the reaction conditions (i.e. temperature, time, metallic precursor type, etc.) play an important role in controlling both the size of synthesized palladium nanoparticles and their chemical properties. A correct choice of the conditions allowed to obtain small and non-oxidized particles, suitable for different technological applications, ranging from catalysis to membranes for hydrogen storage, etc. In addition, we have recently discovered that, as a result of quantum-size effects, palladium may acts as a catalyst in the polymers combustion[3].

[3] L.Schiavo et al; *"**Catalytic effect of Pd clusters in the poly (N-vinyl-2-pyrrolidone) combustion",*** submitted in October 2017.

3.5. References

[1] D.L. Feldheim, J. Colby A. Foss, Metal Nanoparticles: Synthesis, Characterization, and Applications, Marcel Dekker, Inc., 2001.

[2] Corain B Schmid G Toshima N, Metal nanoclusters in catalysis and materials science : the issue of size control, in: Elsevier, 2008: p. 458. doi:10.1016/B978-044453057-8.50036-2.

[3] S.W. Kim, M. Kim, W.Y. Lee, T. Hyeon, Fabrication of hollow palladium spheres and their successful application to the recyclable heterogeneous catalyst for suzuki coupling reactions, J. Am. Chem. Soc. 124 (2002) 7642–7643. doi:10.1021/ja026032z.

[4] P. Tobiska, O. Hugon, A. Trouillet, H. Gagnaire, An integrated optic hydrogen sensor based on SPR on palladium, Sensors Actuators, B Chem. 74 (2001) 168–172. doi:10.1016/S0925-4005(00)00728-0.

[5] D. Hao, S. Hue-Zhao, S. Cheng-Min, H. Chao, X. Zhi-Chuan, L. Chen, T. Yuan, W. Deng-Ke, G. Hong-Juan, Synthesis of monodisperse palladium nanocubes and their catalytic activity for methanol electrooxidation, Chinese Physic B. 19 (2010) 106104–1. doi:10.1088/1674-1056/19/10/106104.

[6] C. Ducamp-Sanguesa, R. Herrera-Urbina, M. Figlarz, Fine palladium powders of uniform particle size and shape produced in ethylene glycol, Solid State Ionics. 63–65 (1993) 25–30. doi:10.1016/0167-2738(93)90081-D.

[7] S. Ayyappan, R.S. Gopalan, G.N. Subbanna, C.N.R. Rao, Nanoparticles of Ag, Au, Pd, and Cu produced by alcohol reduction of the salts, J. Mater. Res. 12 (1997) 398–401. doi:10.1557/JMR.1997.0057.

[8] F. Fievet, J.P. Lagier, B. Biblin, Homogeneous and heterogeneous nucleations in the polyol process for the preparation of micron and submicron size metal particles, Solid State Ionics. 32–33 (1989) 198–205. doi:10.1016/0167-2738(89)90222-1.

[9] W. Lu, B. Wang, K. Wang, X. Wang, J.G. Hou, Synthesis and characterization of crystalline and amorphous palladium nanoparticles, Langmuir. 19 (2003) 5887–5891. doi:10.1021/la034160a.

[10] N. Thosima, F. Fievét, M.P. Pileni, K. Kimura, Metals, Fine Part. Synth. Charact. Mech. Growth. 92 (2000) 430–550.

[11] D. Berger, G.A. Traistaru, B. Vasile, Palladium Nanoparticles Synthesis With Controlled Morphology Obtained By Polyol Method, U.P.B. Sci. Bull. Ser. B. 72

(2010) 113–120.

[12] J. Xian, Q. Hua, Z. Jiang, Y. Ma, W. Huang, Size-Dependent Interaction of the Poly(*N* -vinyl-2-pyrrolidone) Capping Ligand with Pd Nanocrystals, Langmuir. 28 (2012) 6736–6741. doi:10.1021/la300786w.

[13] J. Cookson, The preparation of palladium nanoparticles, Platin. Met. Rev. 56 (2012) 83–98. doi:10.1595/147106712X632415.

[14] T. Teranishi, M. Miyake, Size Control of Palladium Nanoparticles and Their Crystal Structures, Chem. Mater. 10 (1998) 594–600. doi:10.1021/cm9705808.

[15] C. Evangelisti, N. Panziera, A. D'Alessio, L. Bertinetti, M. Botavina, G. Vitulli, New monodispersed palladium nanoparticles stabilized by poly-(N-vinyl-2-pyrrolidone): Preparation, structural study and catalytic properties, J. Catal. 272 (2010) 246–252. doi:10.1016/j.jcat.2010.04.006.

[16] A. Nemamcha, H. Moumeni, J.L. Rehspringer, PVP Protective mechanism of palladium nanoparticles obtained by sonochemical process, in: Phys. Procedia, 2009: pp. 713–717. doi:10.1016/j.phpro.2009.11.015.

[17] P. Grammatikopoulos, C. Cassidy, V. Singh, M. Sowwan, Coalescence-induced crystallisation wave in Pd nanoparticles., Sci. Rep. 4 (2014) 5779. doi:10.1038/srep05779.

[18] A. Shailja, L.S. Madan, K. Pratibha, Evidence for monoalkoxide species on the surface of palladium nanoparticles synthesized in ethylene glycol, Mater. Chem. Phys. 114 (2009) 107–112. doi:10.1016/j.matchemphys.2008.08.082.

[19] D. Hao, S. Xue-Zhao, S. Cheng-Min, H. Chao, X. Zhi-Chuan, L. Chen, T. Yuan, W. Deng-Ke, G. Hong-Jun, Synthesis of monodisperse palladium nanocubes and their catalytic activity for methanol electrooxidation, Chinese Phys. B. 19 (2010) 106104. doi:10.1088/1674-1056/19/10/106104.

[20] C.D. Wagner, W.M. Riggs, L.E. Davis, J.F. Moulder, B.E. Muilenberg, The technical writer's handbook of x-ray photoelectron spectroscopy, perkin-elmer, Perkin-Elmer, Phys. Electron. Div. (1979).

[21] Y. Yu, Y. Zhao, T. Huang, H. Liu, Shape-controlled synthesis of palladium nanocrystals by microwave irradiation, Pure Appl. Chem. 81 (2009) 2377–2385. doi:10.1351/PAC-CON-08-11-22.

[22] A.L. Patterson, The scherrer formula for X-ray particle size determination, Phys. Rev. 56 (1939) 978–982. doi:10.1103/PhysRev.56.978.

[23] M. Nardi, R. Verucchi, L. Aversa, M. Casarin, A. Vittadini, N. Mahne, A. Giglia, S.

Nannarone, S. Iannotta, K.M. Kadish, S. Kera, Electronic properties of tetrakis(pentafluorophenyl)porphyrin, New J. Chem. 37 (2013) 1036. doi:10.1039/c3nj40910d.

[24] A. Gniewek, A.M. Trzeciak, J.J. Ziółkowski, L. Kępiński, J. Wrzyszcz, W. Tylus, Pd-PVP colloid as catalyst for Heck and carbonylation reactions: TEM and XPS studies, J. Catal. 229 (2005) 332–343. doi:10.1016/j.jcat.2004.11.003.

[25] D. Briggs, Handbook of X-ray Photoelectron Spectroscopy CD Wanger, WM Riggs, LE Davis, JF Moulder and GE Muilenberg Perkin-Elmer Corp., Physical Electronics Division, in: Surf. Interface Anal., 1981: p. 190. doi:10.1002/sia.740030412.

Chapter 4

Synthesis and characterization of nanostructured magnesium composites into a poly(methyl methacrylate) (PMMA) matrix

4.1. Introduction

The hydrogen storage technologies represent the critical point for the transport systems H_2-based developing [1,2]. Recently, a group of Mg-based hydrides stands as promising candidate for competitive hydrogen storage, with reversible hydrogen capacity up to 7.6 wt% for on-board applications [3–6]. Many researchers have focused their attention toward the development of new nanostructured magnesium-based materials and their composites, due to their improved properties, as fast kinetics, high hydrogen storage capacity in a reversible way, and lower desorption temperature, than to the corresponding bulk materials [7–11]. A most common method used for the nanostructured magnesium production was the ball-milling technique, because is a cheap scalable and easy of use approach [3,12]. This technique allows to obtain significant surface improvements due to the formation of micro/nanostructures, and also of the defects up to inside to the materials, that produce an increasing of surface area [13]. The kinetics and thermodynamic parameters are strictly connected to surface properties, and they improves with the surface area increasing, showing better properties than the corresponding bulk materials [3,8]. However, the most important disadvantage of the mechanical alloying process concerns an oxidized layer formation on magnesium surface. The oxygen layer causes changes in the surface properties, thus inhibiting the hydrogenation. Actually, an air-stable composite material consisting of metallic Mg nanocrystals in a gas-selective polymer, poly(methyl

methacrylate) (PMMA) was developed [14]. The use of a polymer offers different advantages. It can be used like a stabilizing agent able to produce a tailored material, simply modifying the synthesis parameters as temperature, pressure or precursor/polymer concentration. Different nucleation processes occurred changing these parameters, and crystals of different sizes can be achieved. Besides, the use of a gas-selective polymer, as PMMA, allows to mitigate the oxygen and humidity diffusion towards the Mg nanocrystals embedded in it. At the same time, it enhances the hydrogen permeability. In addition, the improved nanocomposites flexibility promoted by using the polymer matrix allows to withstand the volume expansion during phase transition between Mg and MgH_2. Impressively, the produced Mg/PMMA nanocomposites have shown stability after two weeks of air exposure [14]. The novel nanocomposites facilitate hydrogen storage with both high density (up to 6 wt% of Mg, 4 wt% for the composite) and rapid kinetics (loading in <30 min at 200°C) without using heavy metal catalysts. The remarkable uptake capacity and kinetics can be sustained for a few adsorptions and desorption cycles, with only slightly decrease of dehydrating rate. For these reasons, such new interesting Mg nanocomposites certainly deserve further attention.

In this research activity an innovative method for the nanocomposites Mg-based by thermolysis of an organometallic compound, the bis(η^5-cyclopentadienyl) magnesium(II) (Cp_2Mg), embedded into a poly(methyl methacrylate) (PMMA), was developed. The bis(η^5-cyclopentadienyl) magnesium(II) [15–17] (Cp_2Mg), belonging to the magnesocene class, consists of two cyclopentadienyl anions (Cp^-, which is $C_5H_5^-$) bounded to a central metal (M^{2+}) in the oxidation state II, with the resulting general formula $(C_5H_5)_2$ M. The schematic illustrations of Cp_2Mg general chemical structure (A) and of the ball-and-stick model (B), where the cyclopentadienyl anions are in a staggered conformation, are reported in Figure 4.1.

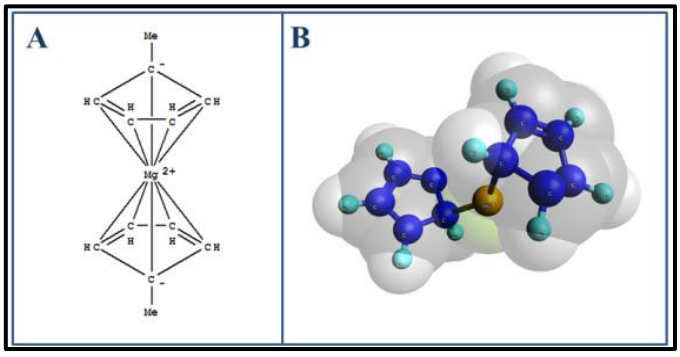

Figure 4.1 Cp_2Mg general chemical structure (A) and of the ball-and-stick model (B)

According to IUPAC, a metallocene contains a central metal and two cyclopentadienyl ligands coordinated in a sandwich structure. The cyclopentadienyl anion is an aromatic 6π-electron system. Both anions are on parallel planes with equal bond lengths and strengths. The Mg^{2+} cation should be enough small ($r \approx 0.65$ A°) to facilitate the interaction of both Cp^- rings [18], which can be easily removed from the structure by a heating treatment [19]. Its structure is similar to that of ferrocene $Fe(C_{10}H_{10})_2$ [16,20]. Thanks to this particular kind of structure, Cp_2Mg was widely used as a cyclopentadienyl group transfer reagent, in the preparation of metal cyclopentadienyl complexes and it has also been used as a polymerization catalyst [21]. In the last 20 years, Cp_2Mg has been also used as a dopant source for the growth of *p*-type semiconductor films by chemical vapor deposition (CVD) techniques [22,23]. The Cp_2Mg low melting point (176°C) and the reduced vapor pressure [15,16] make this compound particularly suitable as precursor in the thermolysis approach. A new method, for the nanocomposites Mg-based materials preparation, was proposed. The nanocomposite sample preparation process consist of two steps: the first step concerns the precursor/polymer solid solution preparation, called "Cp_2Mg/PMMA", which corresponds to a "*reactive system"* made of the two starting reagents mixed together by a *"solvent mediated method"*, in which tetrahydrofuran (THF) is used as solvent. The second step concerns the thermal decomposition (or thermolysis) of such solid solution on a heating ceramic plate for the nanostructured magnesium embedded into the polymer (Mg/PMMA) formation. The annealing is used to remove the two radicals fragments ($\cdot C_5H_5$) coordinated to the central metal of the precursor embedded into the polymer matrix. The homolysis of the C-Mg bonds promotes the Mg-nanocrystals embedded into the polymer formation. Different characterizations have been performed. Microscopic and spectroscopic techniques were used for the structural and morphological Mg-nanocrystals embedded into the polymer characterization. The transmission electron microscopy (TEM), the scanning transmission electron microscopy (STEM) and the electron energy loss spectroscopy (EELS) measurements have been used to obtain information about the morphology, the atomic and electronic structure of the magnesium nanocrystals. The thermal stability both of the reactive system and of the magnesium nanocomposites has been studied by thermo-gravimetric analysis (TGA). The functional groups decomposition of the precursor, both in the pure form and as solid solution, was investigated by FTIR analysis. The optical spectroscopy (UV-Vis) was also used to investigate the reactive system. The surface composition of the samples was investigated using the X-ray

Photoelectron Spectroscopy (XPS) and the energy dispersive X-ray microanalysis (EDS-SEM) analysis. The techniques aforementioned are described in the Appendix B.

4.2. Experimental details

The nanostructured magnesium composites preparation has involved two steps: the first step concerns the polymer/precursor solid solution preparation (Cp_2Mg/PMMA blend) by a wet-way; the second step concerns the thermal annealing of such solid solution. A schematic representation of nanocomposites sample preparation process is reported in Figure 4.2.

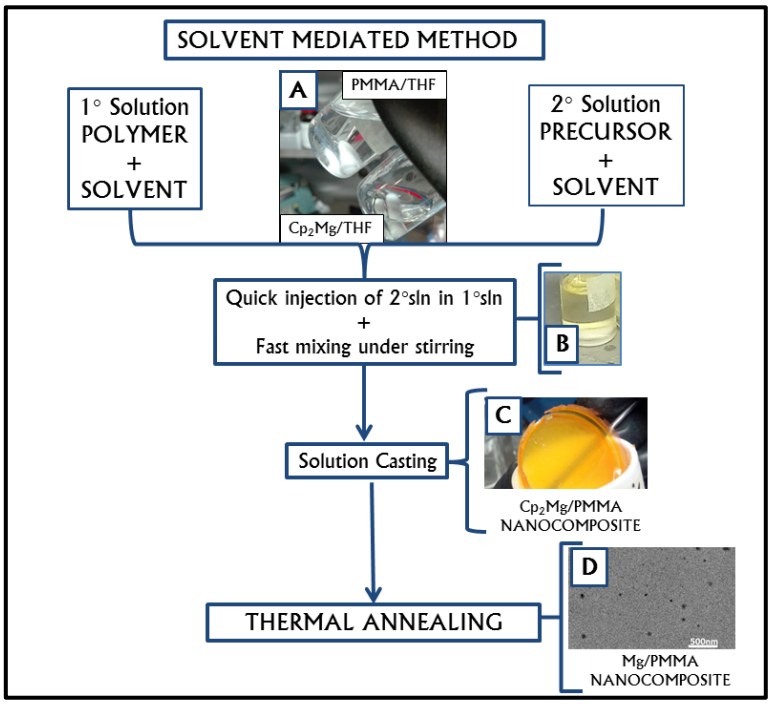

Figure 4.2 Schematic representation of nanocomposite sample preparation process

The raw materials were commercial products: poly(methyl methacrylate) (PMMA) of two different molecular weights ($\overline{Mw}$ ~120,000 by GPC and average $\overline{Mw}$ ~350,000 by GPC); the bis(η^5-cyclopentadienyl)magnesium(II) (Cp_2Mg, purified by sublimation, 97%); the tetrahydrofuran (THF) (anhydrous ≥99.9%, inhibitor-free). All materials were purchased from Sigma-Aldrich and used as received. The whole process was performed in a "*LABmaster Up*" glove box workstation from MBraun, operating under nitrogen atmosphere. The glove box was equipped with an oxygen and humidity controller working at <0.1ppm and <0.1ppm contents, respectively. The organometallic compounds of the

most electropositive metal elements (as magnesium) exhibit some common features such as high air reactivity (spontaneous ignition) and oxidation phenomena. For these reason the reactions involving the organometallic compounds, as Cp_2Mg, have been manipulated in inert atmosphere. A more detailed description of the manipulation of the air sensitive compounds is given in Appendix A. The Cp_2Mg/PMMA blends were prepared by dissolving separately the PMMA and Cp_2Mg in the THF, for the preparation of the "*1° Solution*" and "*2°Solution*" respectively, as reported in the Figure 4.2. This approach is known as **"*Solvent Mediated Method*"**, and it is commonly used for the blends or polymer solution preparation. The *1° Solution* was prepared dissolving a certain amount of PMMA (≈500mg) in THF (10mL). This solution was left under stirring for 24 hours, to allow the complete dissolution of the polymer into the solvent. Successively, the *2°Solution* obtained by the dissolution of a certain amount of Cp_2Mg (≈ 167mg) in THF (2mL) (solution 0.5 M of Cp_2Mg in THF) was prepared. The precursor and polymer amounts were selected to obtain a magnesium-nanocomposite at 5 wt% of Mg in PMMA (5 wt% Mg/PMMA), so that the produced nanoparticles were well dispersed in the polymer matrix (low concentration). This solution was left under stirring for few minutes, and a complete dissolution fastly occurred. After this time the *2°Solution* was quickly added, with a rapid injection, into the polymer solution (Figure 4.2, B). The resulting solution was poured into a teflon container: the solvent was then removed by evaporation at room temperature (casting from solution) in the glove box. After casting, the solvent was removed and the achieved blend (see Figure 4.2, C) was **thermally annealed** at 220°C for 10 minutes. Thanks to the reduced vapor pressure of the Cp_2Mg compound, during the thermal treatment the two organic radicals ($\cdot C_5H_5$) interacts, forming an hydrocarbon [18] which completely evaporate during the process. During the first 5 minutes of thermal treatment, a brown gaseous phase was released, probably due to evaporation of the two cyclopentadienyl. The inorganic phase was formed into the polymer matrix (5wt%Mg/PMMA) in a finely dispersed form. The TEM micrograph of the resulting nanocomposites is shown in Figure 4.2, D. The synthesis of metal nanoparticles in presences of surface stabilizer prevents the strong tendency of fine metal particle to coalesce. The poor metallic clusters mobility into the polymer matrix reduces the possibility of aggregates formations, due to the diffusion limited growth of the nanoparticles [24–27], leading to the achievement of a nanoscopic phase uniformly dispersed and in a non-aggregated form.

At the beginning, preliminary studies on the materials used were performed, starting from the polymer and the magnesium precursor. The thermal properties of different PMMA films were investigated. The study of the polymer thermal stability was used to establish the temperature required for the annealing treatment. The thermolysis process should occur at temperatures lower of decomposition temperature of the polymer and, at the same time, higher than the decomposition temperature of the precursor, to facilitate the removal of organic fragments. For these reasons, the decomposition temperature of the polymer must be higher than the melting point of the magnesium precursor. The reactivity of Cp_2Mg, evaluated by the oxidation process occurring during a progressive air exposure was also examined by using the FTIR-spectroscopy analysis. Successively the reactive system (Cp_2Mg/PMMA blend) thermal properties were studied. The thermal decomposition represents a key point in the synthesis process, for the selection of the annealing temperature. The optical spectroscopy (UV-Vis) had allowed to study the kinetic of the nanoparticles formation. Finally, a deeply investigation of the Mg/PMMA nanocomposites was performed. Different characterization techniques, described in the Appendix B, were used to study the Mg clusters embedded into the polymer. The magnesium is a reactive element, and when it came in contacts with air or humidity can lead to oxidative phenomena. Thus a careful manipulation before the analysis is strongly necessary to achieve good results.

4.3. Experimental results

4.3.1. Thermal stability characterizations of PMMA

The first process step involves the dissolution of PMMA in THF. Three PMMA films were prepared, using polymers with different molecular weights. The first PMMA polymer had a $\overline{Mw}$ ~120,000 (Aldrich), called "PMMA120", the second had a $\overline{Mw}$~350,000 (Aldrich), called "PMMA350". These two films were prepared by solution casting of PMMA in THF, in air at room temperature. Another PMMA film was obtained using the PMMA350, at room temperature and inert atmosphere (PMMA350GB). The thermal stability of all films was studied by thermogravimetric analysis (TGA), and the corresponding thermograms were reported in Figure 4.3.

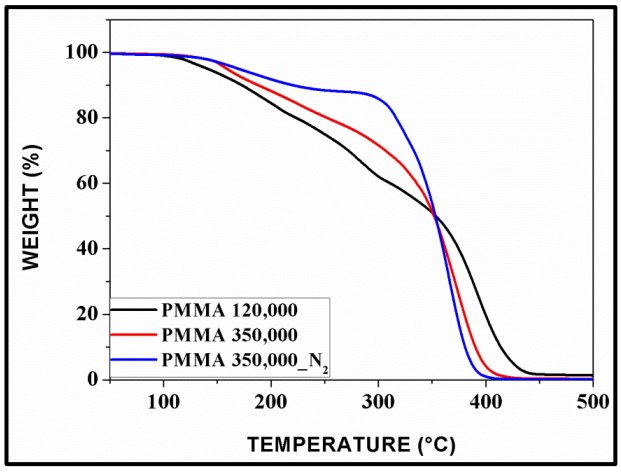

Figure 4.3 Thermograms of PMMA polymers having $\overline{Mw}$≈120,000 (black curve) and $\overline{Mw}$≈350,000 (red curve) prepared in air. Thermogram of PMMA polymer having $\overline{Mw}$≈350,000, prepared in inert atmosphere (blue curve). The TGA analysis were performed at rate of 10°C/min under nitrogen atmosphere

The TGA analysis was performed by a dynamic scan from room temperature to 500°C, at rate of a 10°C/min in nitrogen atmosphere. As it is visible, the PMMA350GB sample (blue curve) prepared in glove box shows a better thermal stability than the others two films, PMMA350 and PMMA120, prepared in air. The last two samples begin to decompose already at about 120°C, which is a not suitable temperature considering the thermal decomposition of the of Cp_2Mg precursor. The PMMA350GB begin to decompose at about 300°C (see Figure 4.2), a temperature enough higher than the melting point (176°C) of Cp_2Mg precursor. For this reason the polymer solution for the Mg/PMMA nanocomposites preparation was performed by using the PMMA350GB. Such solution was prepared in glove box.

4.3.2. Morphology and reactivity of Cp_2Mg precursor

The Cp_2Mg morphology was studied by TEM analysis. The organometallic Cp_2Mg precursor was dissolved in THF at room temperature in inert atmosphere, and a drop of this solution was placed on the Formvar-coated copper grid. The grid was sealed in an aluminum bag under nitrogen atmosphere (in order to prevent by the oxidation phenomena) and the bag was opened just before of the characterizations. The TEM micrographs of Cp_2Mg precursor at different magnifications can be seen in Figure 4.4. As is shown the TEM micrographs, areas of different colors of the grayscale are clearly visible, which can be attributed to the formation of agglomerated of Mg, $Mg(OH)_2$ and MgO particles. The formation of $Mg(OH)_2$ and MgO phases may have occurred both for

air exposure during the experimental preparation stage [3,14,28], and for the degradation phenomena of the Cp_2Mg compound induced by the electron-beam irradiation during the observation by TEM can also verified [19,29].

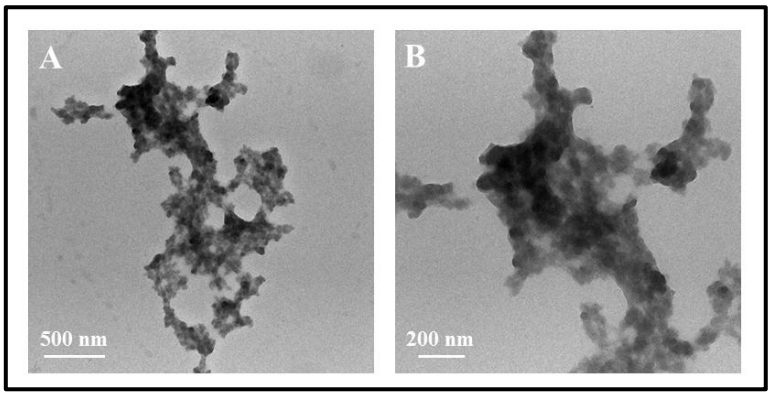

Figure 4.4 TEM micrographs of Cp_2Mg precursor at different magnifications

The Cp_2Mg reactivity was evaluated by spectroscopic analysis using the FTIR spectroscopy. The Cp_2Mg sample powders were dispersed in vaseline (2% wt/wt) and spreaded between sodium chloride (NaCl) windows, commonly used for FTIR spectroscopy, in inert atmosphere. The measurements were collected in air. The FT-IR spectra of vaseline dispersing medium (black curve) and of Cp_2Mg precursor in vaseline (red curve) were reported in Figure 4.5.

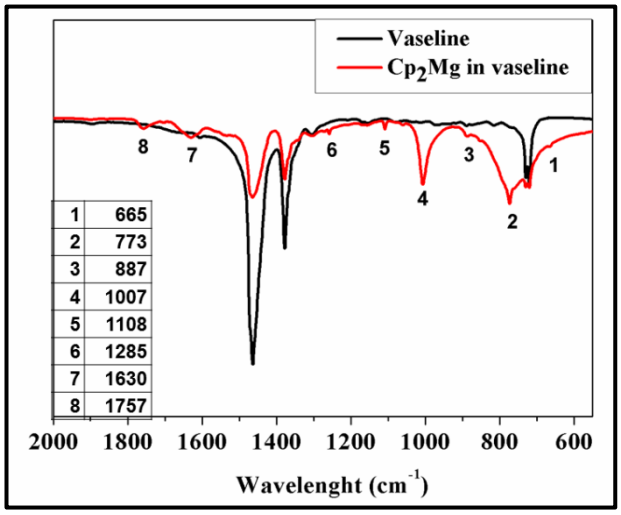

Figure 4.5 FT-IR spectra of vaseline dispersing medium (black curve) and of Cp_2Mg precursor dispersed in vaseline (red curve)

The peaks ranging between the 1400 to 600 cm^{-1} wavenumber (Finger Print Zone) exactly match those of the Cp_2Mg powder [28,30]. The table in the Figure 4.5 reports the index and the wavenumber values of the peaks, respectively. The perfect correspondence of the peaks with those of the precursor indicates that the functional groups of the sample dispersed in vaseline observed after a few minutes of air exposure have not undergone any modification. Then, on the same sample, the effects of air exposure during the time have been studied. In Figure 4.6 the FT-IR spectra of vaseline (black curve), of Cp_2Mg precursor dispersed in vaseline promptly observed (red curve), after 1 minute (blue curve) and after 40 minutes (magenta curve) of air exposure, were reported. The 1007 cm^{-1} peak (number 4), corresponding to the C-H out of the plane bending vibration, typical of the cyclopentadienyl anions Cp^- [28,30], was used as reference to study the of decomposition of functional groups of the precursor. As visible, the reference peak intensity decreases during the time, because probably degradation phenomena occurred. Is well known that air exposure of Cp_2Mg leads to a partial hydrolysis of Cp^- to C_5H_6 ring [28], and that after a long air exposure, oxidative phenomena occur [14].

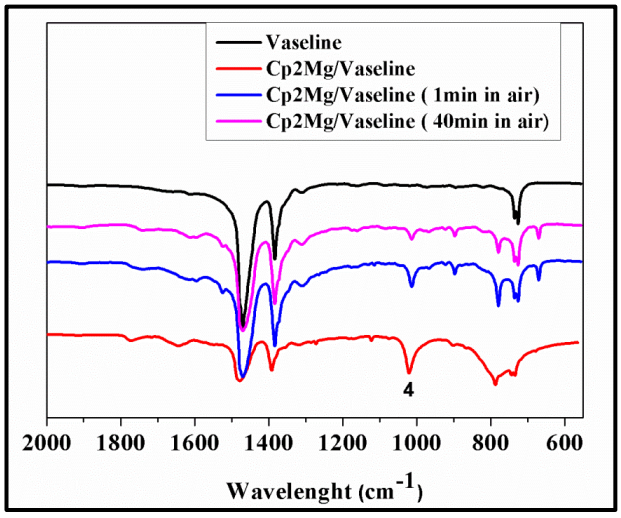

Figure 4.6 FT-IR spectra of vaseline (black curve), of Cp_2Mg precursor dispersed in vaseline quickly observed (red curve), after 1 minute (blue curve) and after 40 minutes (magenta curve) of air exposure.

These hypotheses were verified in the next set of FTIR measurements, in which the sample was directly prepared in air (see Figure 4.8). Few milligrams of Cp_2Mg were taken from glove box in an Eppendorf tube (see Figure 4.7). At the beginning the Cp_2Mg powders were white.

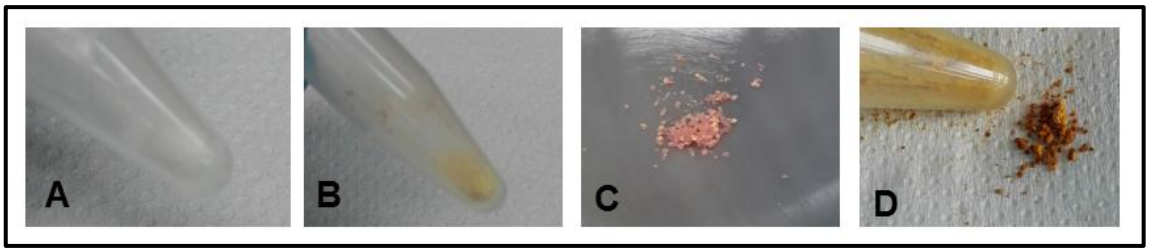

Figure 4.7 Cp_2Mg powders taken from glove box (A) and after different air exposure times (B,C and D)

After Eppendorf opening, the color immediately changes from white to light yellow, and during a permanent air exposure to pink (Figure 4.7, B and C). After a long air exposure, the color turns to dark yellow (Figure 4.7, D). At the measurement time, the powder was pink. The pink powder was dispersed in vaseline and spreaded between two NaCl windows. The FT-IR spectra of vaseline (black curve), of the Cp_2Mg precursor dispersed in vaseline in inert atmosphere (red curve) and of the Cp_2Mg dispersed in vaseline in air (blue curve) are given in Figure 4.8. Taking the peak at 1007 cm^{-1} as reference peak, an immediate disappearance of such peak, just after 1 minute of air exposure, was observed (Figure 4.6, blue curve). When the sample was prepared into a glove box the reference peak slowly disappeared, as the vaseline partially acts as a protective agent, although it was permeable to oxygen and moisture.

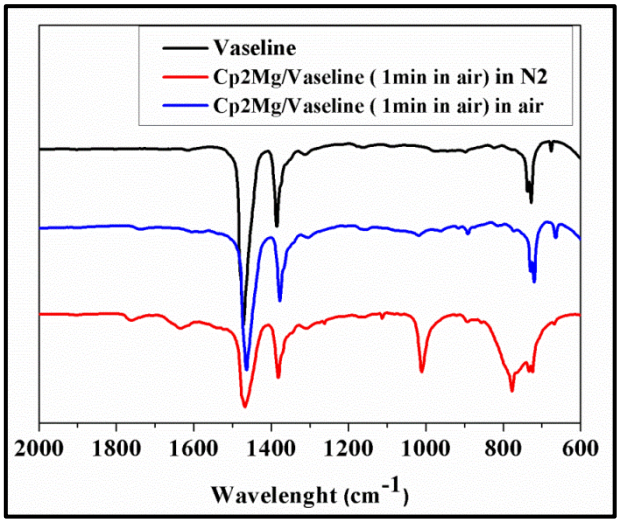

Figure 4.8 FT-IR spectra of vaseline (black curve), of Cp_2Mg precursor dispersed in vaseline in inert atmosphere(red curve) and of Cp_2Mg dispersed in vaseline in air (blue curve)

4.3.3. Characterization of Cp_2Mg/PMMA reactive system

The photographic images of the reactive system solution at 5 wt% of Mg in PMMA (Figure 4.9, B), of the reactive system after solution casting (Figure 4.9, C) and finally after thermal annealing (Figure 4.9, D) are reported. Both the films have been later completely characterized. The spectroscopic (UV-Vis) and thermogravimetric (TGA) characterizations for the Cp_2Mg/PMMA reactive system at 5 wt% of Mg were performed.

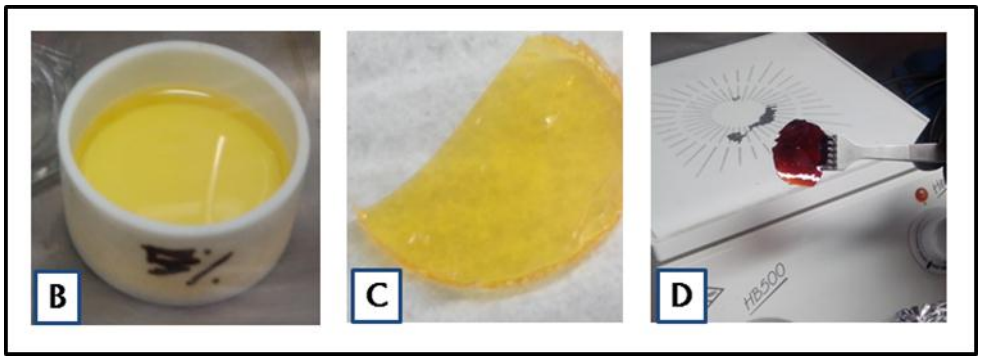

Figure 4.9 Photographic images of the reactive system solution (B), of such solution after casting (C) and after thermal annealing (D)

The UV-Vis spectra for different air-exposure times (at room temperature) were reported in Figure 4.10. At the beginning a 494nm shoulder and a 537nm peak were visible,

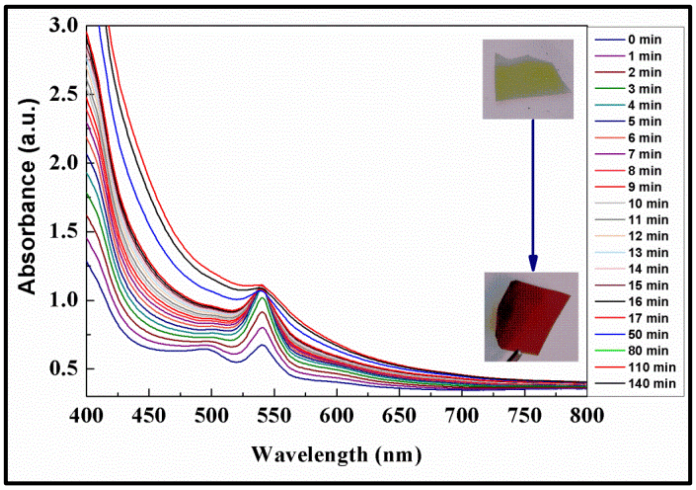

Figure 4.10 UV-Vis spectra of Cp_2Mg/PMMA reactive system at 5 wt% of Mg in PMMA, recorded at different air-exposure times performed at room temperature

corresponding to the surface plasma resonance of magnesium nanoparticles in the visible spectra range [31]. The nanoparticles formation reaction was quick enough; in fact the

peak at 537nm reached the maximum value in 8 minutes. During this time, a clear rising of the absorbance baseline was observed, and, at the same time, the peak disappears due to the scattering of the magnesium nanoparticles formed into the polymer. During this time the blend color changes from light yellow to dark red, as visible in the inlet of Figure 4.10. The thermal stability of Cp_2Mg/PMMA reactive system at 5 wt% of Mg in PMMA, performed at a rate of 10°C/min in nitrogen atmosphere, was successively studied. A comparison between the PMMA and the Cp_2Mg/PMMA thermograms (black and orange curves, respectively) is reported in Figure 4.11, A. The TGA curve of pure PMMA shown a first weight loss, up to about 300 °C, probably due to the evaporation of the solvent used for the polymer preparation. In the same temperature ranges, the weight loss for the Cp_2Mg/PMMA reactive system was greater than the pure PMMA, due to a further evaporation of the two cyclopentadienyl ligands.

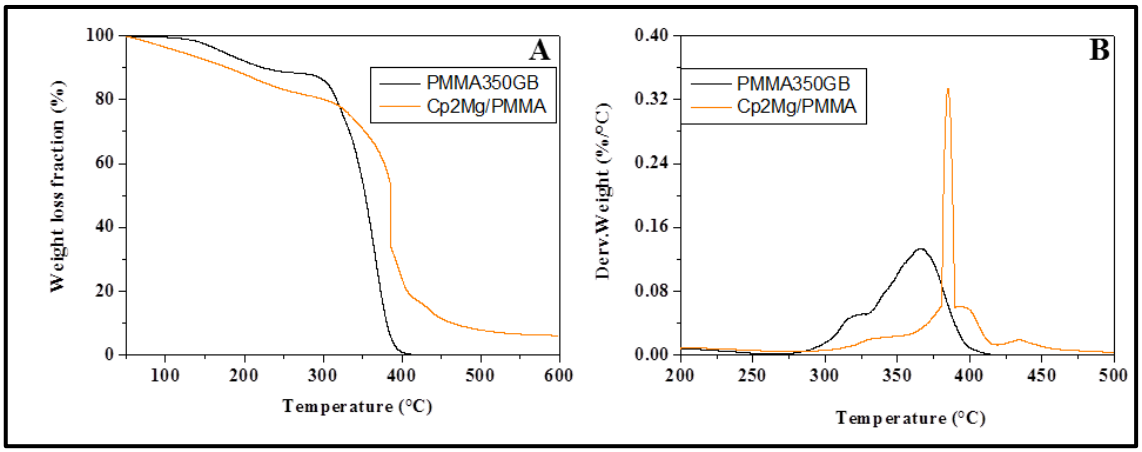

Figure 4.11 (A) Thermograms of PMMA (black curve) and Cp_2Mg/PMMA reactive system (orange curve) and (B) the corresponding derivative weight (%/°C), performed at a rate of 10°C/min in N_2 atmosphere

The major weight loss for the pure PMMA was found to occur between 300°C and 400°C while for the Cp_2Mg/PMMA blend it occurred at a slightly higher temperature (of about 20°C). Figure 4.11, B also shows a residual weight loss of ca. 6 wt% at 600°C for the Cp_2Mg/PMMA blend, due to Mg phase content. The maximum value of the decomposition temperature was evaluated by the DTG curves (see Figure 4.11, B). The DTG curve of pure PMMA exhibited a maximum rate of weight loss at 366°C while the peak value for Cp_2Mg/PMMA blend shifted at higher temperature of 384°C, indicating that the blend was thermally stable up to such temperature. The study of the thermal stability of the Cp_2Mg/PMMA reactive system is important to select the annealing temperature, which

must be lower of the reactive system decomposition temperature but, at the same time, higher than the melting point of Cp_2Mg precursor (176°C). An annealing temperature of 220 °C was chosen; the Cp_2Mg/PMMA reactive system was heated for 10 minutes, until the disappearance of the reaction fumes has been observed, to ensure complete evaporation of the organic part of the precursor.

4.3.4. Characterization of Mg/PMMA nanocomposites

A magnesium-nanocomposite at 5 wt% of Mg in PMMA (5 wt% Mg/PMMA) was prepared and characterized both morphologically and structurally by using the transmission electron microscopy (TEM) and the X-ray diffraction (XRD). The chemical composition and the corresponding oxidative states were also evaluated by X-ray photoelectron spectroscopy (XPS). In addition, atomic and electronic structure of the magnesium nanocrystals embedded into the polymer were performed by using scanning transmission electron microscopy (STEM) and the electron energy loss spectroscopy (EELS) measurements. More details on the last used techniques were reported in Appendix B.

4.3.4.1. Morphological characterization of Mg/PMMA

In order to evaluate the morphological properties of the 5wt% Mg/PMMA sample, a thin film of such sample was prepared. Ultra-thin sections of specimens are cut using an ultramicrotome cutting technique. Sections from 50 to 100 nm thick are prepared to be viewed in the TEM. The micrographs images of 5wt% Mg/PMMA thin film at different magnifications were reported in Figure 4.12. As the TEM micrographs reveals nanoparticles aggregates of different sizes embedded into the polymer matrix are visible. Nanoparticle aggregation phenomena can be attributed to blade action during cutting. The cutting section is clearly visible in Figure 4.12, A. As this sample preparation method did not allow it to estimate the shape and the distribution of the nanoparticles embedded into the polymer, a small amount of 5wt% Mg/PMMA was dissolved in THF at room temperature under inert atmosphere by stirring. The solution was sonicated by an ultrasonic bath for 30 minutes, in order to allow good dispersion of the sample into the solvent. A drop of this solution was placed on the Formvar-coated copper grid. The grid was sealed in an aluminum bag under nitrogen, to prevent oxidation phenomena, and the bag was opened just before the measurements. The TEM micrographs of the sample are showed in Figure 4.13.

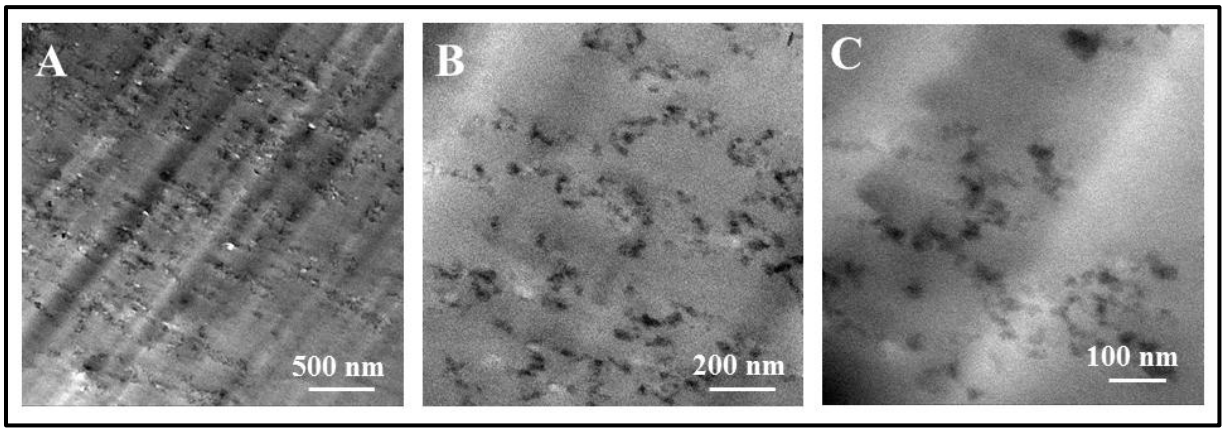

Figure 4.12 The micrographs images of 5wt% Mg/PMMA thin film at different magnifications

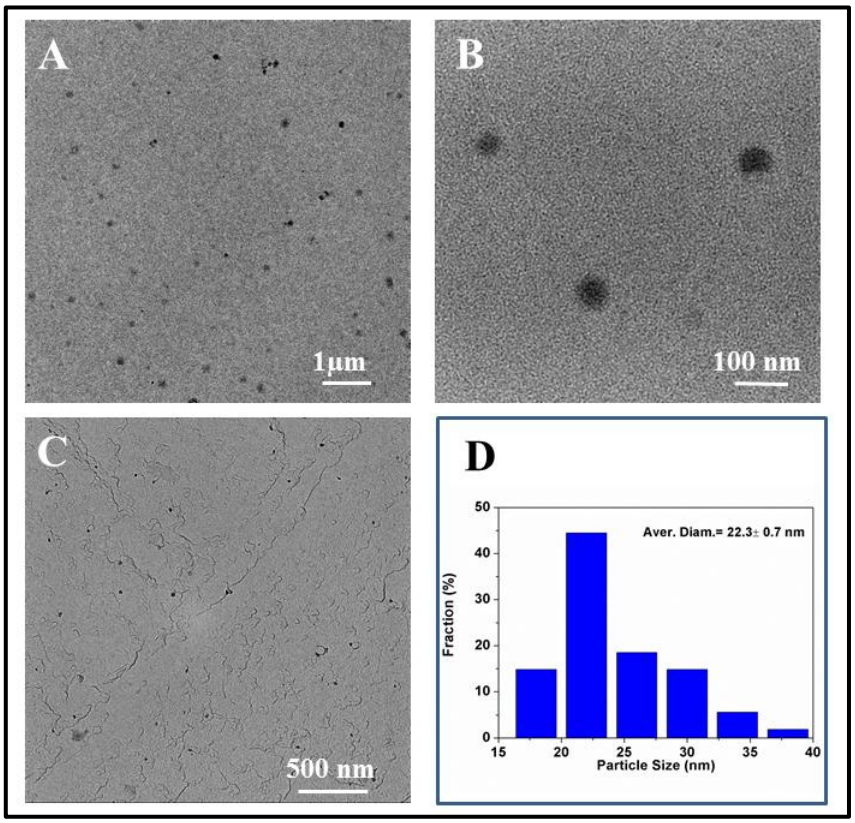

Figure 4.13 The micrographs images of 5%Mg/PMMA prepared by solution casting by THF

Magnesium nanoparticles of a polyhedral shape, having nanoscopic size of ca. 22nm (see Figure 4.13, D) quite monodispersed into the PMMA were formed (Figure 4.13, A), without aggregates. However, the low contrast effects between the metal (of low atomic weight) and the polymer matrix prevent it to obtain clear images at lower magnifications (Figure 4.13,B) [14,32,33].

4.3.4.2. Structural characterization of Mg/PMMA

The structural characterization of the 5wt%MgPMMA for Mg-phase embedded into the PMMA identification was carried out by using X-ray diffraction (XRD). The 5wt%MgPMMA diffractogram is shown in Figure 4.14. The 5wt%MgPMMA diffractogram show a broadening of diffraction peaks line, and the presence of two very low intensity peaks, one at 2θ = 43.6° belonging to magnesium oxide (MgO) [34] and another of lower intensity at 2θ = 36.3° belonging to the metallic magnesium (Mg) nanoparticles [14]. In order to better identify the Mg-phase produced, other XRD analyses were repeated, which led anyway to diffractograms with a broadening of diffraction peaks line. Such phenomenon can be attributed both to the reduced nanoparticles size [35–37] and to their reduced concentration into the polymer, which led to the PMMA spectrum completely amorphous as a result of X-ray diffraction [38,39].

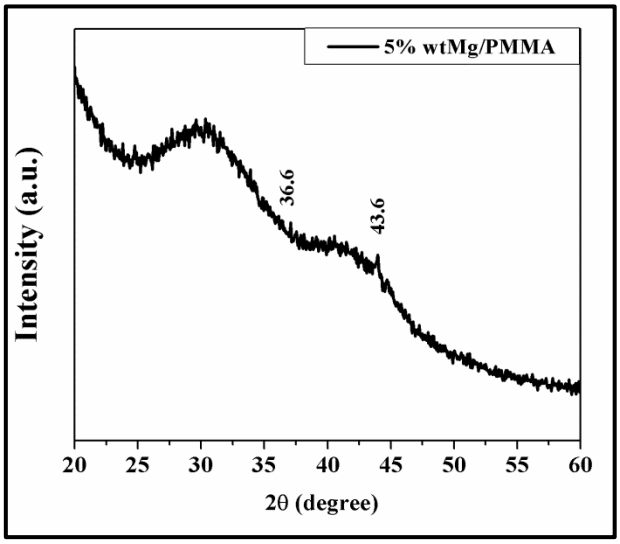

Figure 4.14 XRD diffractogram of 5wt%Mg/PMMA

The Mg-phase will be structurally characterized by using high resolution techniques, such as scanning transmission electron microscopy, which provides local information on the nanometer scale.

4.3.4.3. Photoelectron Spectroscopy characterization of Mg/PMMA

XPS was used to investigate the oxidation state of the Mg nanoparticles embedded into 5wt%MgPMMA nanocomposite. The sample was sealed as prepared in an aluminum bag under nitrogen atmosphere and such bag was opened 5 minutes before to be placed into the

measurement chamber. A significant degassing stage in the Ultra High Vacuum (UHV) chamber was observed. The characterization was carried out at pass energy (PE) of 20eV for the single core level and at PE of 50eV for the wide range spectra, to have the better combination between resolution and short-time analysis. At this PE, the precision on peak positions evaluation is quite good. The wide binding energy (BE) range spectrum of the 5wt%MgPMMA sample was shown in Figure 4.15.

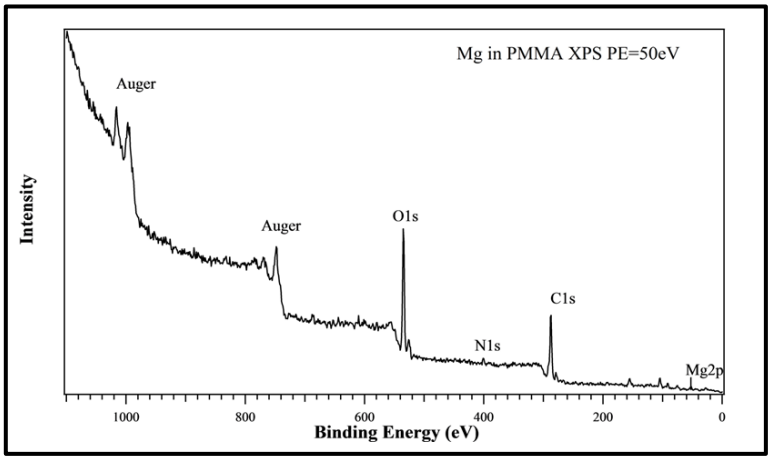

Figure 4.15 XPS wide-range spectra of Mg nanoparticles in PMMA

The presence of all the expected chemical species, that are, C, O, and N (both Auger emission and core levels are clearly visible), and even the Mg was revealed. All core levels are shifted towards higher BE, a phenomenon that is related to charging effects during the analysis due to the electrically insulated characteristics of the polymer. The C1s spectrum (see Figure 4.16) shows a wide structure at ca. 287eV and a second peak at ca. 291.5eV. This second peak, at higher BE position, can be attributed to the C-O bonds in the PMMA, and in particular to the carboxyl bonds. Since the carboxyl bonds peak position in a standard PMMA film is known (~ 288.8eV) [40], it is possible to calculate the shift of all core levels rescaling the spectra, thus getting the correct BE. Figure 4.17 shows the Mg2p spectrum of Mg nanoparticles in PMMA. The Mg2p core level has been analyzed by Voight lineshape deconvolution after background subtraction of a Shirley function. Two main components, one at low BE and the other at higher BE, about 1eV from the main peak, have been introduced to properly reproduce the peak lineshape, that cannot be analyzed with only one feature.

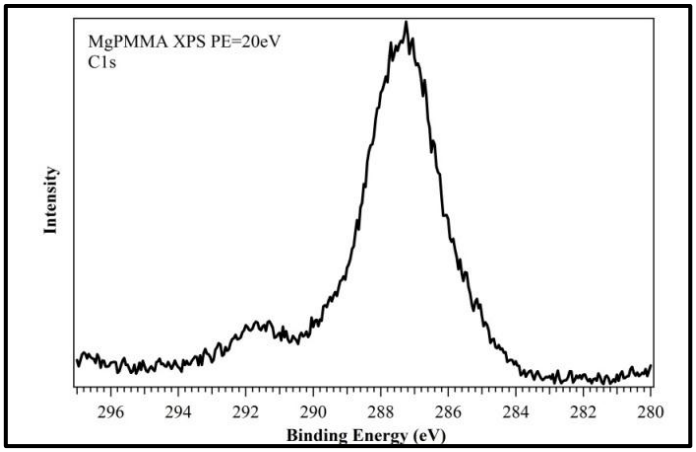

Figure 4.16 XPS C1s spectra of Mg nanoparticles in PMMA

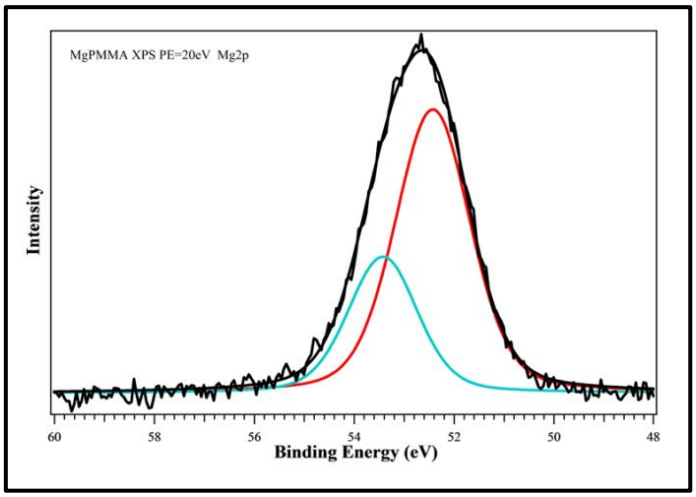

Figure 4.17 XPS Mg2p spectra of Mg nanoparticles in PMMA

Considering the energy scale correction, the main peak is ca. 49.5eV, in an energy range closer to the metallic Mg than to greater valence species [41,42]. The highest BE peak can be attributed both to oxidized species and to Mg bonds with other chemical species. Within this peak, the red component is ca. 69.3%. About the atomic percentage on the surface, assuming that all carbon and oxygen atoms belongs to the sample (contamination has been subtracted), the integral area of the core level evaluation allows to estimate these percentages, that are the following: C 67.1%, O 20.7% and Mg 12.2%, with a 2.5% error on the absolute value.

4.3.4.4. Atomic and electronic structure characterization of Mg/PMMA

Deep structural and morphological investigation were carried out using a sub-Angstrom aberration-corrected JEOL ARM200F microscope, equipped with a high resolution camera and scanning transmission electron microscopy systems (STEM). The energy dispersive X-ray (EDX) and the electron energy loss (EELS) spectroscopic analyses were respectively performed for the chemical composition and electronic structure recognition. The EELS analysis is able to give structural and chemical information about a solid, with a spatial resolution down to the atomic level. The diffraction profile study was performed for the structural Mg-phase identification.

The sample preparation has involved the nanocomposite dissolution in THF solvent under stirring at room temperature and in inert gas atmosphere; the solution was successively sonicated for 30 minutes, in order to improve the fine solid dispersion. The bottle containing the solution was sealed in an aluminum bag under nitrogen atmosphere and opened just before the characterization. The sample was then deposited on a grid of "lacey carbon only" in air, and observed. In the Figure 4.18 the conventional TEM micrographs (CTEM) of 5 wt% of Mg in PMMA (A, B and C) and the corresponding diffraction profile, calculated by using a Fast Fourier Transform (FFT) (D) are reported. As it is visible in Figure 4.18, A, a homogeneous distribution of very small nanocrystals embedded into the polymer matrix is shown. The crystallites are randomly organized within the polymeric matrix (Figure 4.18, B and C), showing a clear diffraction profile (Figure 4.18, D). The Bright Field (BF) STEM image (Figure 4.19, A) clearly shows the crystallites morphology and dimension, corresponding to 2 nm. The Mg crystals appear with dark contrast, since they give heaviest scattering in this system. In the High Angular Annular Dark Field (HAADF) STEM image (Figure 4.19, B), the different contrast mechanisms of incoherently scattered electrons contribute to the mapping of the sample, giving clearer informations on the distribution of the nanocrystals-embedded into the polymer. The energy dispersive X-ray analysis (EDX) and the electron energy loss spectroscopy (EELS) of 5 wt% of Mg in PMMA nanocomposite at 200KeV were performed and reported in Figure 4.20.

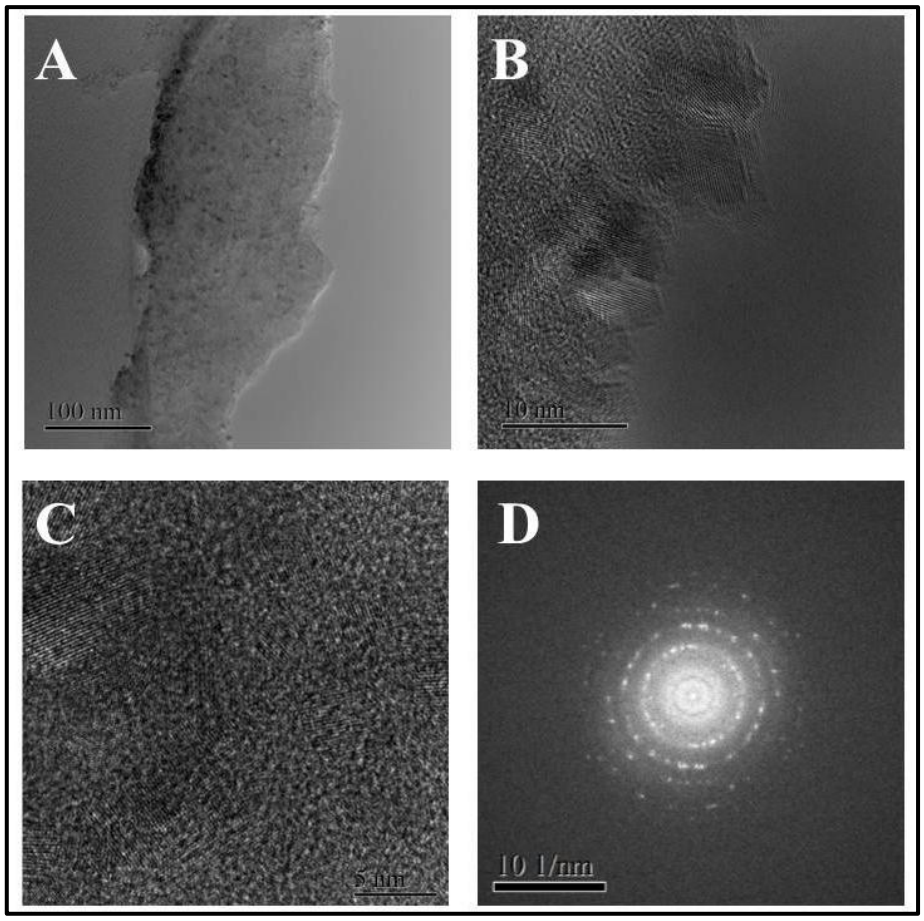

Figure 4.18 CTEM micrographs of magnesium nanocrystals at 5 wt% of Mg in PMMA nanocomposite (A, B and C) and the corresponding diffraction profile (D) performed at 200KeV.

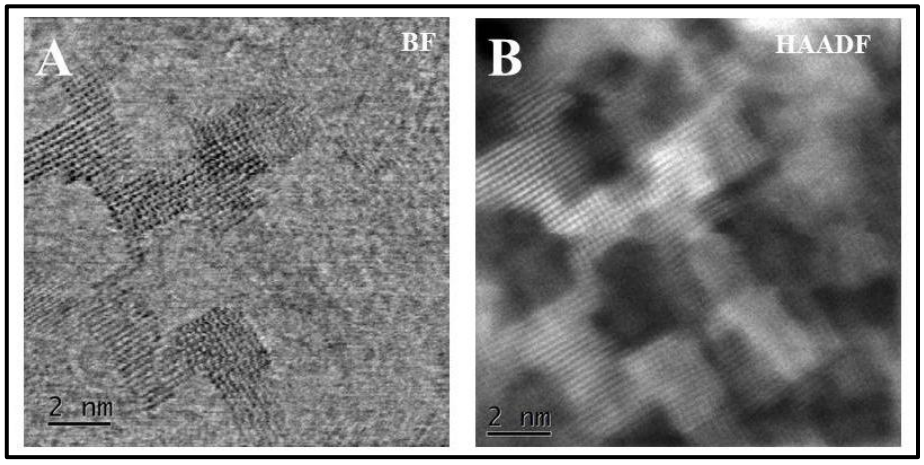

Figure 4.19 Bright Field" (BF) (A) and "High Angular Annular Dark Field" (HAADF) (B) STEM images of 5 wt% of Mg in PMMA nanocomposite performed at 200KeV.

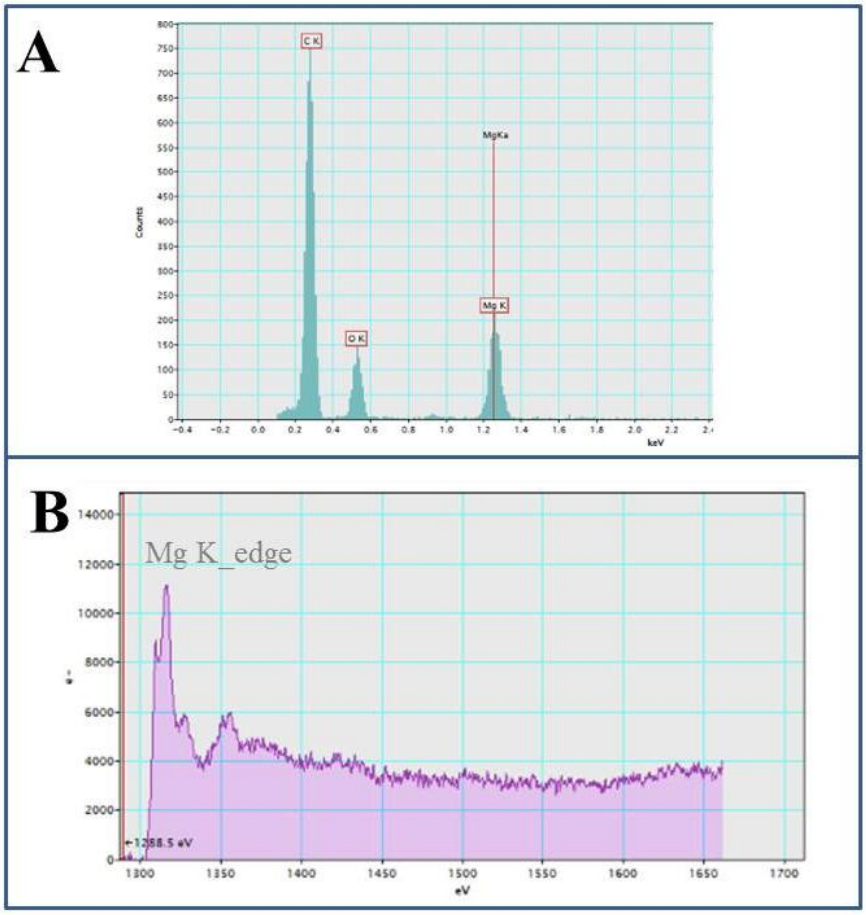

Figure 4.20 EDX (A) and (EELS) spectra (B) of 5 wt% of Mg in PMMA nanocomposite performed at 200 KeV.

The chemical microanalysis technique (Figure 4.20, A) have revealed that the chemical composition of the Mg/PMMA nanocomposite was composed only of carbon, oxygen and magnesium (C, O and Mg) elements, thus indicating that the sample is free from impurities. The EELS spectrum presents the characteristic shape of the Mg K edge in MgO crystal. This result was better explained by the diffraction profile investigations (see Figure 4.21). As it is shown in Figure 4.21, the X-ray diffraction pattern of the 5 wt% Mg/PMMA nanocomposite had shown a peak with a 55% of intensity, related to (020) plane corresponding to a cubic structure of magnesium oxide (MgO) and another peak with a 19% of intensity, due to (113) plane corresponding to the hexagonal structure of metallic magnesium (Mg). The last index belongs both to Mg and MgO crystals. Therefore it is possible to conclude that the previously identified magnesium crystallites of 2 nm are prevalently oxidized. Oxidation phenomena may be due both to the time between the preparation of the sample and its measurements and the grid air exposure before the TEM analysis.

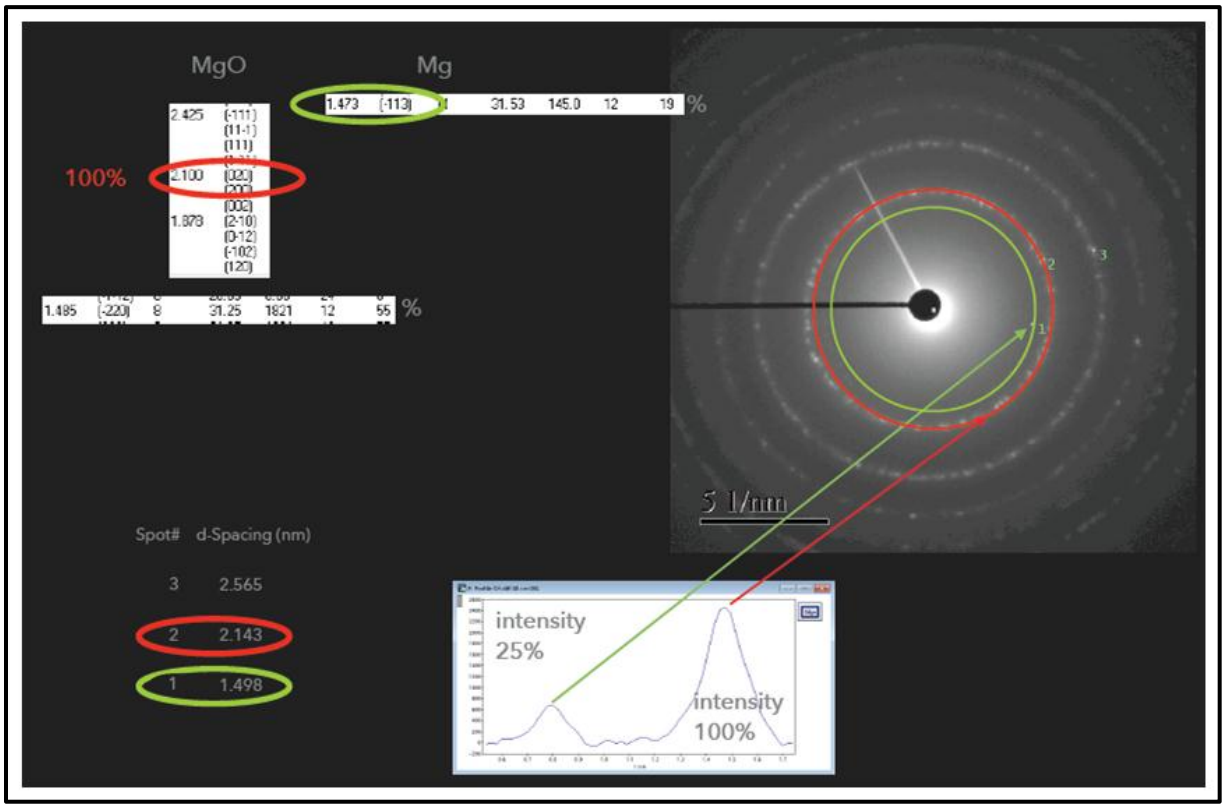

Figure 4.21 Diffraction profile of 5 wt% of Mg in PMMA performed by the scanning transmission electron microscopy (S/TEM) at 200 KeV

4.4. Conclusion

An innovative method for trying to prepare air-stable nanocomposites magnesium-based was proposed. Such method is based on the thermolysis of an organometallic compound, the Cp_2Mg, embedded into a PMMA matrix. The preparation involves two steps. The first step is used for the Cp_2Mg/PMMA solid solution preparation, whereas the second step of thermal annealing is performed for the nanostructured Mg/PMMA composites preparation. Different characterizations were performed for the Mg-phase identification. The X-ray photoelectron spectroscopy (XPS) performed on the sample "as prepared" have been revealed the presence both of the metallic (most abundant) and oxidized Mg phases. The morphological (TEM) and structural (STEM) investigations has revealed the presence of magnesium nanocrystals of about 2nm, completely oxidized. However, the magnesium is a reactive metal and probably, during the sample preparation for the analysis, oxidation phenomena occurred. It should also be pointed out that the reduced dimensions of the metal produced, and hence the nanostructuring effects, amplify the interface phenomena and therefore the oxidation.

4.5. References

[1] L. Schlapbach, a Züttel, Hydrogen-storage materials for mobile applications., Nature. 414 (2001) 353–358. doi:10.1038/35104634.

[2] S.S. Makridis, Hydrogen storage and compression, MRS Bull. 33 (2008) 421–428. doi:10.1557/mrs2008.84.

[3] B. Sakintuna, F. Lamari-Darkrim, M. Hirscher, Metal hydride materials for solid hydrogen storage: A review, Int. J. Hydrog. Energy. 32 (2007) 1121–1140. doi:10.1016/j.ijhydene.2006.11.022.

[4] I.P. Jain, C. Lal, A. Jain, Hydrogen storage in Mg: A most promising material, Int. J. Hydrogen Energy. 35 (2010) 5133–5144. doi:10.1016/j.ijhydene.2009.08.088.

[5] P. Selvam, B. Viswanathan, C. Swamy, V. Srinivasan, Magnesium and magnesium alloy hydrides, Int. J. Hydrogen Energy. 11 (1986) 169–192. doi:10.1016/0360-3199(86)90082-0.

[6] K.-F. Aguey-Zinsou, J.-R. Ares-Fernández, Synthesis of Colloidal Magnesium: A Near Room Temperature Store for Hydrogen, Chem. Mater. 20 (2008) 376–378. doi:10.1021/cm702897f.

[7] A. Pundt, Hydrogen in Nano-sized Metals, Adv. Eng. Mater. 6 (2004) 11–21. doi:10.1002/adem.200300557.

[8] M.U. Niemann, S.S. Srinivasan, A.R. Phani, A. Kumar, D.Y. Goswami, E.K. Stefanakos, Nanomaterials for hydrogen storage applications: A review, J. Nanomater. 2008 (2008) 1–9. doi:10.1155/2008/950967.

[9] R. Bardhan, A.M. Ruminski, A. Brand, J.J. Urban, Magnesium nanocrystal-polymer composites: A new platform for designer hydrogen storage materials, Energy Environ. Sci. 4 (2011) 4882–4895. doi:10.1039/c1ee02258j.

[10] F. Cheng, Z. Tao, J. Liang, J. Chen, Efficient hydrogen storage with the combination of lightweight Mg/MgH2 and nanostructures, Chem. Commun. 48 (2012) 7334. doi:10.1039/c2cc30740e.

[11] A. Zaluska, L. Zaluski, J.. Ström–Olsen, Nanocrystalline magnesium for hydrogen storage, J. Alloys Compd. 288 (1999) 217–225. doi:10.1016/S0925-8388(99)00073-0.

[12] V. Bérubé, G. Radtke, M. Dresselhaus, G. Chen, Size effects on the hydrogen storage properties of nanostructured metal hydrides: A review, Int. J. Energy Res. 31 (2007) 637–663. doi:10.1002/er.1284.

[13] R.A. Varin, L. Zbroniec, M. Polanski, J. Bystrzycki, A review of recent advances on the effects of microstructural refinement and nano-catalytic additives on the hydrogen storage properties of metal and complex hydrides, Energies. 4 (2011) 1–25. doi:10.3390/en4010001.

[14] K.-J. Jeon, H.R. Moon, A.M. Ruminski, B. Jiang, C. Kisielowski, R. Bardhan, J.J. Urban, Air-stable magnesium nanocomposites provide rapid and high-capacity hydrogen storage without using heavy-metal catalysts, Nat. Mater. 10 (2011) 286–290. doi:10.1038/nmat2978.

[15] J.M. Birmingham, Synthesis of Cyclopentadienyl Metal Compounds, in: 1965: pp. 365–413. doi:10.1016/S0065-3055(08)60082-9.

[16] W.A. Barber, W.L. Jolly, Magnesium Cyclopentadienide, in: Inorg. Synth., John Wiley & Sons, Inc., 1960: pp. 11–15. doi:10.1002/9780470132371.ch5.

[17] B. Wakefield, Organomagnesium methods in organic synthesis 1st Edition, Academic Press, 1995.

[18] H. Kunkely, A. Vogler, Optical properties of bis(cyclopentadienyl)magnesium: excimer-type luminescence of the bis(cyclopentadienyl) ligand frame, J. Organomet. Chem. 689 (2004) 2940–2943. doi:10.1016/j.jorganchem.2004.05.048.

[19] D.-W. Lim, J.W. Yoon, K.Y. Ryu, M.P. Suh, Magnesium Nanocrystals Embedded in a Metal-Organic Framework: Hybrid Hydrogen Storage with Synergistic Effect on Physi- and Chemisorption, Angew. Chemie. 124 (2012) 9952–9955. doi:10.1002/ange.201206055.

[20] C. Elschenbroich, Organometallics., Wiley-VCH, 2006.

[21] J. Libiszowski, K. Kałużynski, S. Penczek, Polymerization of cyclic esters of phosphoric acid. VI. Poly(alkyl ethylene phosphates). Polymerization of 2-alkoxy-2-oxo-1,3,2-dioxaphospholans and structure of polymers, J. Polym. Sci. Polym. Chem. Ed. 16 (1978) 1275–1283. doi:10.1002/pol.1978.170160610.

[22] C.-R. Lee, J.-Y. Leem, S.-K. Noh, S.-E. Park, J.-I. Lee, C.-S. Kim, S.-J. Son, K.-Y. Leem, Characteristics of Mg-doped GaN epilayers grown with the variation of Mg incorporation, J. Cryst. Growth. 193 (1998) 300–304. doi:10.1016/S0022-0248(98)00436-9.

[23] H. Amano, M. Kitoh, K. Hiramatsu, I. Akasaki, Growth and Luminescence Properties of Mg-Doped GaN Prepared by MOVPE, J. Electrochem. Soc. 137 (1990) 1639. doi:10.1149/1.2086742.

[24] J. Cookson, The preparation of palladium nanoparticles, Platin. Met. Rev. 56 (2012)

83–98. doi:10.1595/147106712X632415.

[25] A.D. Pomogailo, G.I. Dzhardimalieva, Reduction of Metal Ions in Polymer Matrices as a Condensation Method of Nanocomposite Synthesis, in: Nanostructured Mater. Prep. via Condens. Ways, Springer Netherlands, Dordrecht, 2014: pp. 13–89. doi:10.1007/978-90-481-2567-8_2.

[26] N.T.K. Thanh, N. Maclean, S. Mahiddine, Mechanisms of Nucleation and Growth of Nanoparticles in Solution, Chem. Rev. 114 (2014) 7610–7630. doi:10.1021/cr400544s.

[27] I. Capek, Noble Metal Nanoparticles: Preparation, Composite Nanostructures, Biodecoration and Collective Properties, Springer, 2017.

[28] W.T. Ford, Spectra of cyclopentadienylalkali and cyclopentadienylmagnesium compounds in tetrahydrofuran, J. Organomet. Chem. 32 (1971) 27–33. doi:10.1016/S0022-328X(00)80156-4.

[29] R.J.T. Houk, B.W. Jacobs, F. El Gabaly, N.N. Chang, A.A. Talin, D.D. Graham, S.D. House, I.M. Robertson, M.D. Allendorf, Silver Cluster Formation, Dynamics, and Chemistry in Metal−Organic Frameworks, Nano Lett. 9 (2009) 3413–3418. doi:10.1021/nl901397k.

[30] V.T. Aleksanyan, I.A. Garbuzova, V.V. Gavrilenko, L.I. Zakharkin, Vibrational spectra and structure of bis(cyclopentadienyl)magnesium, J. Organomet. Chem. 129 (1977) 139–143. doi:10.1016/S0022-328X(00)92483-5.

[31] F. Sterl, N. Strohfeldt, R. Walter, R. Griessen, A. Tittl, H. Giessen, Magnesium as Novel Material for Active Plasmonics in the Visible Wavelength Range, Nano Lett. 15 (2015) 7949–7955. doi:10.1021/acs.nanolett.5b03029.

[32] D. Pukazhselvan, V. Kumar, S.K. Singh, High capacity hydrogen storage: Basic aspects, new developments and milestones, Nano Energy. 1 (2012) 566–589. doi:10.1016/j.nanoen.2012.05.004.

[33] I. Haas, A. Gedanken, M. Moshkovich, D. Aurbach, J. Vandercammen, J.L. Delplancke, R. Winand, M. Moshkovich, E. Levi, Synthesis of metallic magnesium nanoparticles by sonoelectrochemistry, Chem. Commun. 466 (2008) 1795. doi:10.1039/b717670h.

[34] L.-X. Li, D. Xu, X.-Q. Li, W.-C. Liu, Y. Jia, E.R. Mysak, S. Porsgaard, M.B. Salmeron, G.E.B. Jr, A. Nilsson, H. Bluhm, Excellent fluoride removal properties of porous hollow MgO microspheres, New J. Chem. 38 (2014) 5445–5452. doi:10.1039/C4NJ01361A.

[35] J.I. Langford, D. Louër, Powder diffraction, Reports Prog. Phys. 59 (1996) 131–234. doi:10.1088/0034-4885/59/2/002.

[36] L.S. Birks, H. Friedman, Particle Size Determination from X- Ray Line Broadening, J. Appl. Phys. 17 (1946) 687–692. doi:10.1063/1.1707771.

[37] H.R. Moon, J.J. Urban, D.J. Milliron, Size-Controlled Synthesis and Optical Properties of Monodisperse Colloidal Magnesium Oxide Nanocrystals, Angew. Chemie Int. Ed. 48 (2009) 6278–6281. doi:10.1002/anie.200902056.

[38] Q. Wang, X. Wang, X. Li, Y. Cai, Q. Wei, Surface modification of PMMA/O-MMT composite microfibers by TiO2 coating, Appl. Surf. Sci. 258 (2011) 98–102. doi:10.1016/j.apsusc.2011.08.013.

[39] S. Agarwal, N.S. Saxena, V. Kumar, Temperature Dependence Thermal Conductivity of ZnS/PMMA Nanocomposite, in: 2014: pp. 737–739. doi:10.1007/978-3-319-03002-9_190.

[40] R.P. Vasquez, MgO(100) by XPS, Surf. Sci. Spectra. 2 (1993) 13–19. doi:10.1116/1.1247718.

[41] H.B. Yao, Y. Li, A.T.S. Wee, An XPS investigation of the oxidation /corrosion of melt-spun Mg, Appl. Spectrosc. 158 (2000) 112–119. doi:10.1016/S0169-4332(99)00593-0.

[42] O. Friedrichs, J.C. Sánchez-López, C. López-Cartes, M. Dornheim, T. Klassen, R. Bormann, A. Fernández, Chemical and microstructural study of the oxygen passivation behaviour of nanocrystalline Mg and MgH2, Appl. Surf. Sci. 252 (2006) 2334–2345. doi:10.1016/j.apsusc.2005.04.018.

Chapter 5

Synthesis and characterization of nanostructured magnesium composites into a polyetherimide (PEI) matrix

5.1. Introduction

In the previous chapter a chemical approach for trying to prepare air-stable nanocomposites magnesium-based was proposed. This approach consist in the thermolysis of an organometallic compound, the bis(η^5-cyclopentadienyl)magnesium(II) (Cp_2Mg), dissolved into a soluble polymer matrix (PMMA). Different characterizations were performed for the Mg-phase identification. Metallic and oxidized magnesium nanoclusters of extremely low sizes, of about 2 nm were found. The magnesium is a reactive metal, thus during the sample preparation for the analysis, oxidation phenomena can be occurred. In order to prevent oxidation phenomena, PMMA was replaced with a thermally more stable polymer matrix, the polyetherimide (PEI), a high-performance amorphous thermoplastic polymer provided of better oxygen permeability and moisture. The schematic illustration of PEI structure is reported in Figure 5.1.

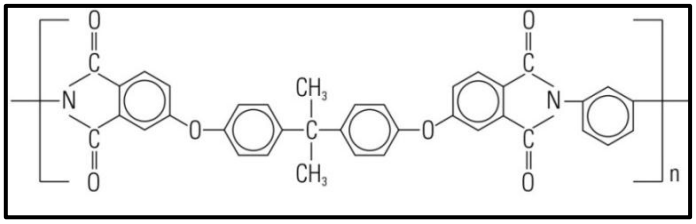

Figure 5.1 Polyetherimide structure

The polyetherimides are a new class of high performance polymers displaying excellent mechanical properties up to high temperature, because of the high glass transition temperature (Tg up to 400°C). Stiffness and high heat resistance provided by the aromatic imide linkages are coupled to the chain flexibility and good melt flow characteristics provided by ether bridges groups [1]. Their outstanding thermo-oxidative stability and flame and solvent resistance are characteristic of aromatic polyimides but, unlike many other polyimides, they can also be processed by conventional techniques (e.g., injection molding) [2]. Of particular interest there is its use to realize membranes for water-vapor separation in the dehumidification of gases, air, and organic vapors [1]. In addition, the polyetherimide has an limited oxygen permeation [2–5], which makes this class of polymers as very suitable for the magnesium nanocomposites preparation. These polymers are soluble in different organic solvents [6], and such feature is useful for their use in the solid solutions preparation. As is visible in Figure 5.1, this polymer structure includes some polar groups (immidic functions, made of carbonyl and amine groups) making it able to interact with the organometallic compounds [7].

In this research activity, a new class of nanostructured magnesium composites prepared by the thermolysis of Cp_2Mg precursor embedded into a soluble matrix, the polyetherimide (PEI), was developed. The process takes place in two stages, such as described in the previous chapter, but different conditions are used, as the type of solvent used for the solid solutions preparation, the annealing temperature, etc. The design of the thermolysis apparatus has been also changed. The "*reactive system*", composed of Cp_2Mg and PEI, was prepared using the anhydrous chloroform ($CHCl_3$), since PEI was highly soluble in such solvent at room temperature. The Cp_2Mg/PEI solid solution thermolysis was made in a tubular oven under nitrogen flow instead of on a ceramic hot plate into the glove box, in order to guarantee a more homogenous and controlled heating treatment, and the possibility to select a higher working temperature. The tubular oven was from "Barnsted/Thermolyne", equipped with a "Eurothterm" thermoregulator. The apparatus process was implemented by a "***sample transport device***", used for the sample transportation under inert atmosphere from the glove box, in which the solid solution were prepared, to the tubular oven and to come back in the glove box. After thermal annealing, the sample was relocated into the glove box and successively sealed in aluminum bags, which will be opened just before the characterizations. A more detailed description of the thermolysis apparatus scale-up is given in Appendix1. Different characterizations

techniques have been performed to identify the produced type of phase. Such techniques are described in the Appendix B.

5.2. Experimental details

The nanostructured magnesium composites preparation consists of two stages: the first stage concern the polymer/precursor solid solution (Cp_2Mg/PEI) preparation by a wet-way, and the second stage concern its thermal annealing. The raw materials were obtained commercially: a PEI of $\overline{Mw}$~350,000 was used. The PEI molecular weight was the same chosen for the previous nanocomposites preparation. The bis(η^5-cyclopentadienyl) magnesium(II) (Cp_2Mg, purified by sublimation, 97%) and chloroform anhydrous ($CHCl_3$, ≥99%, contains 0.5-1.0% ethanol as stabilizer) were used. All reagents were purchased from Sigma-Aldrich and used as received. The solid solution was prepared in a glove box (described in Appendix A) equipped with an oxygen and humidity controller working at <0.1ppm and <0.1ppm contents, respectively. The precursor and polymer amounts were selected to obtain a magnesium-nanocomposite at 8wt% of Mg in PEI (8wt% Mg/PEI). This concentration is slightly higher than the one used for the Mg/PMMA nanocomposites previously prepared in order to try to improve the Mg-phase detection evaluated by the common characterization techniques. Nevertheless, the selected concentration was still low, to ensure good dispersion of nanoparticles in the polymer matrix. The Cp_2Mg/PEI solid solutions were prepared by dissolving separately the PEI and Cp_2Mg in the $CHCl_3$, respectively. A schematic representation of the Cp_2Mg/PMMA solid solution preparation process is reported in Figure 5.2.

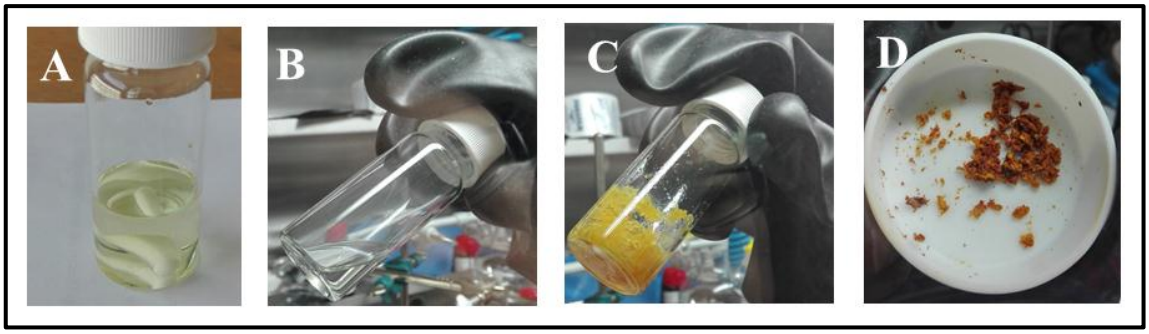

Figure 5.2 Photographic images of Cp_2Mg/PMMA solid solution preparation process

At the beginning the solubility and the thermal properties of a PEI film were investigated. The solubility studies were performed to select a good solvent for the polymer dissolution.

Different organic solvents as THF, DMF, a mixture of THF and DMF solvents [6] were investigated. The polymer showed a good solubility in $CHCl_3$ at room temperature. The PEI solution was prepared dissolving 160mg of PEI in 2mL of $CHCl_3$ at room temperature and under inert atmosphere (Figure 5.2, A). The solution was stirred for 24 hours. After this time, a solution 0.5 M of Cp_2Mg in $CHCl_3$ (≈167mg of Cp_2Mg in 2mL $CHCl_3$) was prepared (Figure 5.2, B). Complete precursor dissolution took immediately place. Such solution was quickly added, with a rapid injection into the polymer solution. The photographic image of solid solution formed is reported in Figure 5.2, C. The Cp_2Mg/PEI solid solution was dried for 24 hours under inert atmosphere (see Figure 5.2, D). After that, the thermal stability of Cp_2Mg/PEI solid solution was studied, in order to determine the annealing temperature. The annealing treatment is used to decompose the Cp_2Mg compound thus producing Mg clusters and remove the two radicals fragments ($\cdot C_5H_5$) that were coordinated to the central metal of the precursor [8]. The homolysis of the C-Mg bonds promotes the formation of Mg-nanocrystals embedded into the polymer. This solid solution resulted to be stable up to a temperature of about 400°C. The annealing was performed at 330°C, which is a temperature sufficiently lower than the solid decomposition temperature.

The polymer thermal stability, before and after a thermal annealing at 330°C was investigated. The decomposition of the polymer functional groups after the heating treatment was also evaluated by ATR spectroscopy. Then the Mg/PEI nanocomposites characterization study was performed. The characterization techniques used are described in Appendix B. Low pressure gas sorption measurements of Mg nanoparticles embedded in PEI were finally performed.

5.3. Experimental results

5.3.1. Solubility and thermal stability characterizations of PEI

The PEI solubility was evaluated in different types of solvents, including the tetrahydrofuran, solvent commonly used for the organometallic precursor Cp_2Mg dissolution. The polymer solutions were prepared at standard temperature and pressure conditions. The polymer was insoluble both in THF and in a mixture of THF and N,N-dimethylformamide (DMF) [6]. Instead it is resulted to be very soluble in chloroform ($CHCl_3$) at room temperature. Therefore was prepared a PEI film by solution casting of

PEI/$CHCl_3$ solution (c.a. 160mg of PEI pellets in 2mL of $CHCl_3$) at room temperature and under nitrogen atmosphere. Only a PEI having $\overline{Mw}$~350,000 (Aldrich) was used. Thermal stability of the film was studied by thermogravimetric analysis (TGA) performed under inert atmosphere. The PEI pellets and the corresponding PEI film thermograms were reported in Figure 5.3.

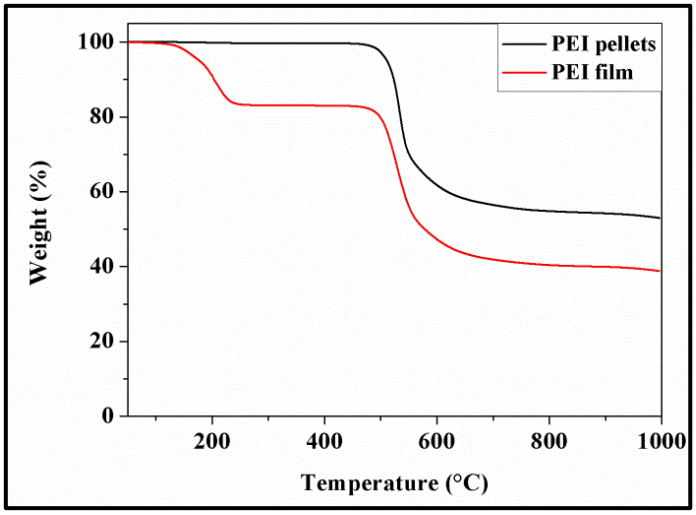

Figure 5.3 TGA thermograms of the PEI pellets and of the film prepared by solution casting in $CHCl_3$

The TGA analysis was performed with a dynamic scan from room temperature to 1000°C, at rate of a 10K/min. As it is visible, both the PEI pellets (black curve) and the film prepared for solution casting (red curve) are very thermally stable, up to 500°C. PEI film presents a first weight loss ending at about 200°C, probably due to clathrates formed by inclusion of solvent molecules during film preparation [9,10]. Such polymer showed higher thermal stability than the PMMA used for the preparation of the first class of magnesium nanocomposites.

The decomposition of the polymer functional groups after the heating treatment at 330°C was also evaluated by the ATR spectroscopic analysis; the spectra were collected in Figure 5.4. In the infrared spectra of PEI (Figure 5.4, black curve), there are absorption bands associated with the vibrations of the two carbonyl groups of imide. The asymmetric and symmetric stretching vibrations of C=O groups were observed in the region of 1776 cm^{-1} and 1715 cm^{-1}. Other absorption bands related to carbonyl, transverse and out of plane vibration of C–N in phthalimide rings, were present in the range of 1350-1360 cm^{-1}, 1070-1100 cm^{-1} and 737-745 cm^{-1}, as shown in Figure 5.4. Vibrations at 1268, 1233, 1072, and 1014 cm–1 are due to the aryl ether bonds (C–O stretching of aromatic ether). Vibrations at

1268, 1233, 1072, and 1014 cm^{-1} are due to aryl ether bonds (C–O stretching of aromatic ether) [11]. As is visible, the PEI peaks position was unchanged after the heating treatment at 330°C. After the annealing the peaks intensities move slightly due to the different thicknesses of the films.

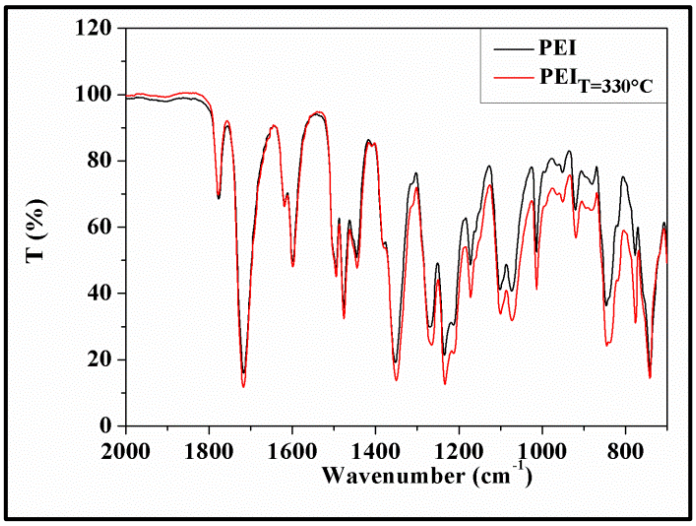

Figure 5.4 ATR spectra of PEI untreated (black curve) and after a thermal annealing at T=330°C (red curve), performed at room temperature

5.3.2. Characterization of Cp_2Mg/PEI solid solution

The thermal stability of Cp_2Mg/PEI solid solution at 8 wt% of Mg in PEI was evaluated by TGA analysis, at rate of a 10K/min under nitrogen atmosphere. A comparison between the PEI and the Cp_2Mg/PEI thermograms (black and red curves, respectively) is reported in Figure 5.5. The TGA curve of pure PEI shown a first weight loss around 200 ºC, that could be associated with loss (~20 wt%) of residual solvent used for the preparation [12]. In the same temperature ranges, the weight loss for the Cp_2Mg/PEI reactive system was lower than for the pure PEI, and thus indicates that the solvent mainly evaporated during the preparation of the solid solution (solution casting). The PEI curve exhibited a maximum of the weight loss starting around 512 ºC, that can be related to the main chain decomposition [1,12]. The maximum weight loss for the Cp_2Mg/PEI solid solution started at a temperature lower than PEI, corresponding to 413°C, probably because of the homolysis of the C-Mg bonds. The Cp_2Mg has the effect to increase the PEI thermal stability because the Cp_2Mg decomposition subtracts part of the heat during the thermal heating. An annealing temperature of 330°C for the solid solution (or reactive system) was

selected, at which such systems was very thermally stable; the reactive system was heated for 10 minutes.

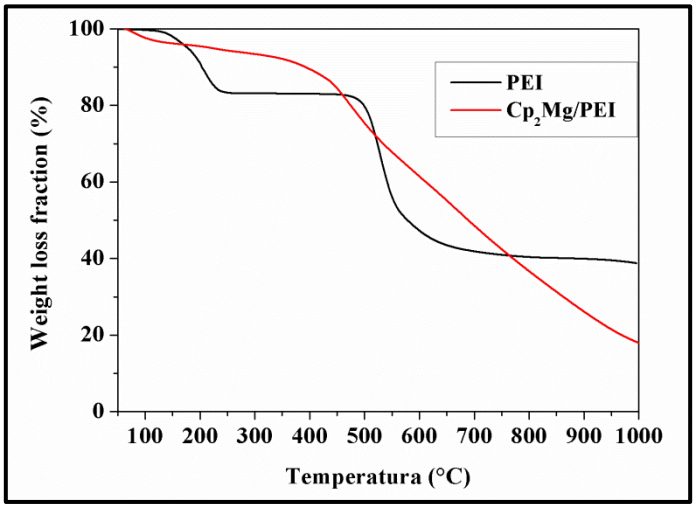

Figure 5.5 Thermogram of PEI (black curve) and of Cp_2Mg/PEI reactive composite (black curve) performed at rate of 10°C/min under N_2 atmosphere

5.3.3. Preparation and characterization of Mg/PEI nanocomposites

Nanostructured magnesium composites with 8 wt% of Mg in PEI were prepared. The Cp_2Mg/PEI solid solution (Figure 5.2, D) was annealed in a tubular oven for 10 minutes at 330°C. The thermal annealing performed at such temperature enhances the release of all the volatile sub-products present in the solid solution, for a sufficiently pure magnesium-based composite formation. In a few minutes, a complete disappearing of these gaseous phase was observed. At the end of the process the nanocomposite was left in the oven, and then cooled down at room temperature. A nanostructured magnesium composite picture (8 wt% of Mg/PEI) after thermal annealing is reported in Figure 5.6.

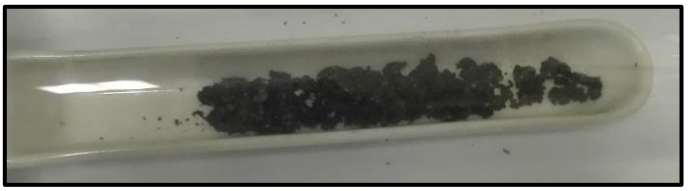

Figure 5.6 Picture of nanostructured magnesium composite (8 wt% Mg/PEI) after thermal annealing

The sample was transferred in the sample transport device from the oven to the glove box. The black color due to the destructive scattering of reflected light can be addressed to an iperfine nature of the metal. The obtained sample was morphologically and structurally characterized, by using the transmission electron microscopy (TEM) and the X-ray diffraction (XRD). The chemical composition and the corresponding oxidative states were also evaluated by X-ray photoelectron spectroscopy (XPS). In addition, atomic and electronic structure of the magnesium nanocrystals embedded into the polymer were performed by using scanning transmission electron microscopy (STEM) and the electron energy loss spectroscopy (EELS) measurements. More details on the last used techniques were reported in Appendix B.

5.3.3.1. Morphological characterization of Mg/PEI nanocomposites

The magnesium nanocomposites morphology was investigated using a TEM. A small amount of 8%wt Mg/PEI was dissolved in $CHCl_3$ at room temperature under inert atmosphere and under stirring, and then the solution was sonicated by an ultrasonic bath for 30 minutes. The sonication is used to allow a good dispersion of the sample into the solvent. A drop of this solution was placed on the Formvar-coated copper grid. The grid was sealed in an aluminum bag under nitrogen atmosphere in order to prevent to oxidation phenomena. The bag was opened just before the measurement. The TEM micrographs are shown in Figure 5.7. As visible from the micrographs acquired in different sample areas and at different magnifications, a highly concentrated and homogeneous distribution of nanoclusters of polyhedral shape (the darker) smaller than 10 nm, dispersed into PEI polymer, are presents. Although the transmission microscopy supply important information about the morphology, and thus about the shape and the distribution of the nanocrystal produced, the use of other characterization techniques are required to identify the produced Mg-phase.

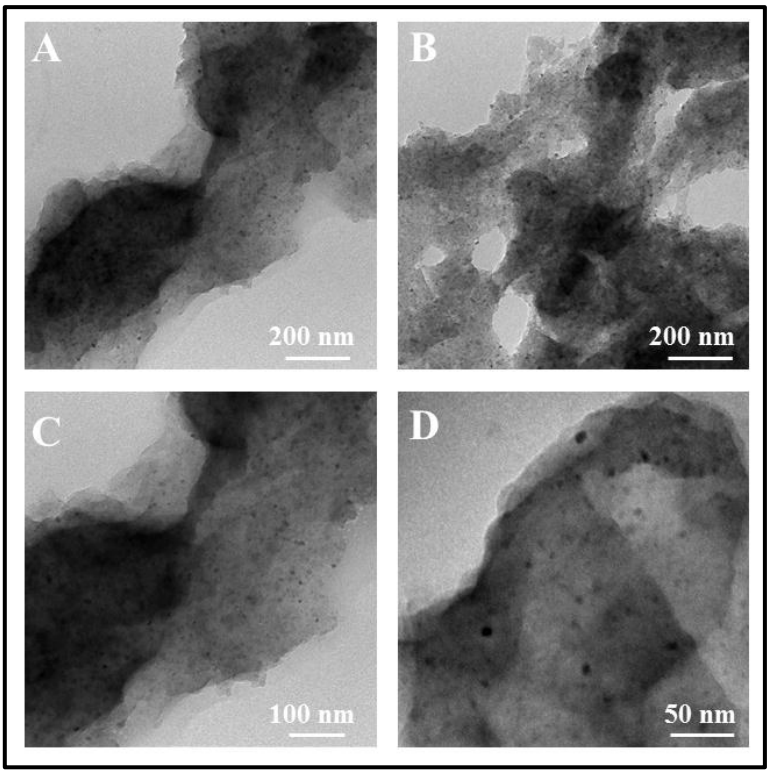

Figure 5.7 TEM micrographs of 8%Mg/PEI after thermal annealing at 330°C in the tubular oven under inert atmosphere, performed at different magnifications

5.3.3.2. Structural characterization of Mg/PEI nanocomposites

The structural characterization of the 8%wt Mg/PEI for the identification of Mg-phase embedded into PEI was carried out by using X-ray diffraction (XRD). The 8%wt Mg/PEI diffractogram is shown in Figure 5.8.

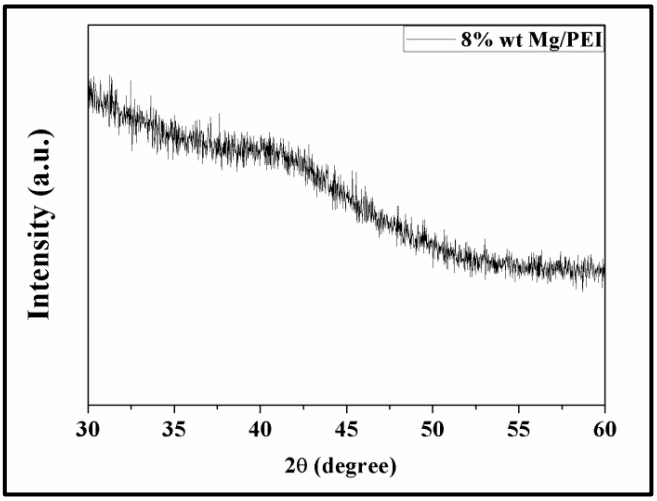

Figure 5.8 XRD diffractogram of 8%wt Mg/PEI after thermal annealing performed at 330°C

The 8%wt Mg/PEI diffractogram shows, as in Mg/PPMA case, a broadening of diffraction peaks line. Such phenomenon can be attributed both to the reduced nanoparticles size [13–15] and to their reduced concentration into the polymer, which led to the PEI spectrum completely amorphous as a result of X-ray diffraction [16,17]. Probably, the instrument sensitivity avoids the detection of small nanoparticles, as those identified in the TEM micrographs.

5.3.3.3. Compositional characterization of Mg/PEI nanocomposites

The chemical composition of the 8%wt Mg/PEI nanocomposite was determined by using the energy-dispersive X-ray spectroscopy (EDS-SEM). In the Table 5.1 the weight percentages of the chemical species which constitute the 8%wt Mg/PEI nanocomposite after its dissolution in $CHCl_3$ and after the thermal annealing (see Figure 5.6) are reported. The dissolution of nanocomposite in the solvent was required to perform different types of measurements (e.g. C/TEM, S/TEM, EELS measurements). The composition for each element was calculated as average values of four measurements, acquired in different sample areas. All data related to analyzed elements were normalized. As shown in Table 5.1, the 8 wt% Mg/PEI nanocomposite was mainly composed of carbon, oxygen, magnesium and chloride traces, coming to the solvent used for the sample preparation. The chemical composition of the 8wt% Mg/PEI nanocomposite changed after its dissolution in $CHCl_3$. In particular, the magnesium quantity drastically decreased and the chloride amount increased. The presence of other elements, such as silicon, calcium and sodium were also revealed. These elements are commonly used to drying solvents [18], and probably traces of them were already present in the commercial solvent used.

Weight (%) from EDS	8%wt Mg/PEI	8%wt Mg/PEI in $CHCl_3$
%Mg	8.5	3.2
%O	20.2	18.8
%C	67.1	57.7
%Cl_2	4.3	14.9
%Si		3,1
%Ca		1,7
%Na		0,6

Table 5.1 Chemical composition of 8wt% Mg/PEI nanocomposite before and after dissolution in $CHCl_3$, performed by EDS-SEM analysis

5.3.3.4. Photoelectron Spectroscopy characterization of Mg/PEI nanocomposites

XPS was also performed on 8 wt% Mg/PEI nanocomposites to evaluate the oxidation state of Mg on the 8%Mg/PEI surface. In order to avoid both air contamination and oxidation processes, the samples were sealed in an aluminum bag after the thermal treatment, and were opened only at moment to be placed into the UHV. Due to significant outgassing in vacuum and to poor signal-to-noise ratio, very high resolution analysis was not possible. Single core levels have been acquired with a PE of 20eV, and wide range spectra at PE of 50eV. Figure 5.9 shows the full range spectrum of the 8%wt Mg/PEI nanocomposites.

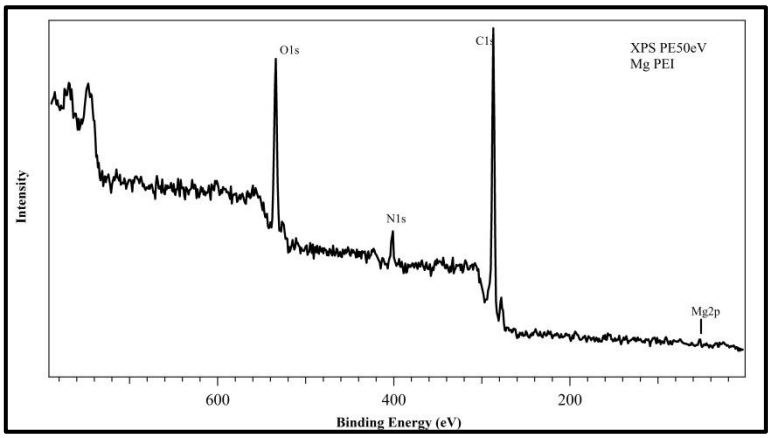

Figure 5.9 XPS wide-range spectra of Mg nanoparticles embedded in PEI

The expected chemical species, such as carbon, oxygen, nitrogen, and Mg were founded. As for PMMA based composites, the charging effect shifts the peaks position to higher binding energies, and thus the core levels BE needed to be corrected (in this case by subtracting 2.1eV). Calibration and correction of charging effects has been possible due to the presence of a reference peak in PEI-C1s core level [19], as shown in Figure 5.10.

C1s spectrum of the bare PEI sample (taken as a reference) highlights the presence of more than one component, in particular a feature ca. 287.3eV related to C-C bonds in the polymer and a second one at ca. 291.1eV, related to C-O and C=O bonds. The feature related to C-N bonds is close to the C-C feature and can be revealed by properly fit the C1s peak. Using the model described in [19], it was possible to reproduce the PEI lineshape and to fit the Mg/PEI C1s peak. Unfortunately this model does not reproduce the peak, but it is possible to identify the C-O/C=O feature, that can be used as calibration peak to calculate the BE shift.

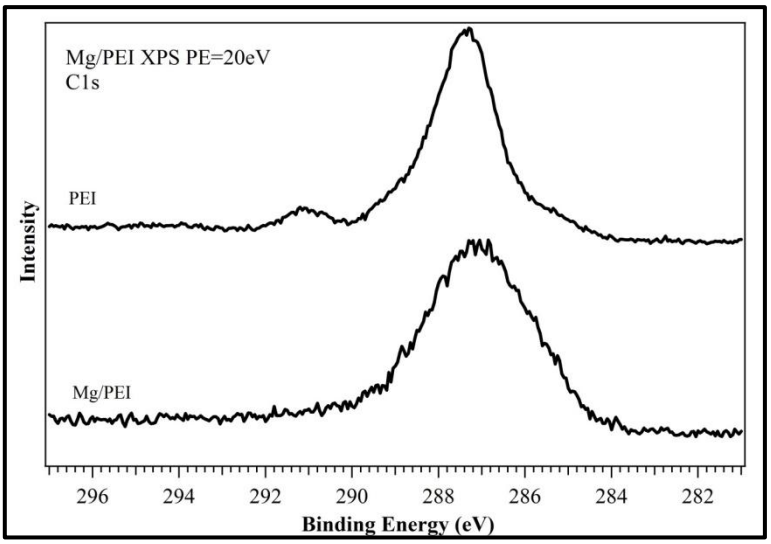

Figure 5.10 XPS C1s spectra of Mg nanoparticles embedded in PEI

The Mg2p core level is shown in Figure 5.11. Although the signal-to-noise is not optimal, the lineshape deconvolution cannot be performed with only one feature, thus two components have to be introduced, one at lower BE (red peak) and the other at higher BE (light blue peak). According to the BE charging shift, the lower BE component is at ~49.5eV, and it corresponds to a typical metallic Mg range [20,21]. The other component suggests the presence of high valence Mg states, like Mg-O bonds. The metallic component corresponds to ca. 31.8% of the total signal area. Concerning the total atomic surface percentages, the integral area of each core level peak leads to the following values (with an error of 2.5% on the absolute value): C 77.3%; O 16.5%; N 4.4% and Mg 1.7%.

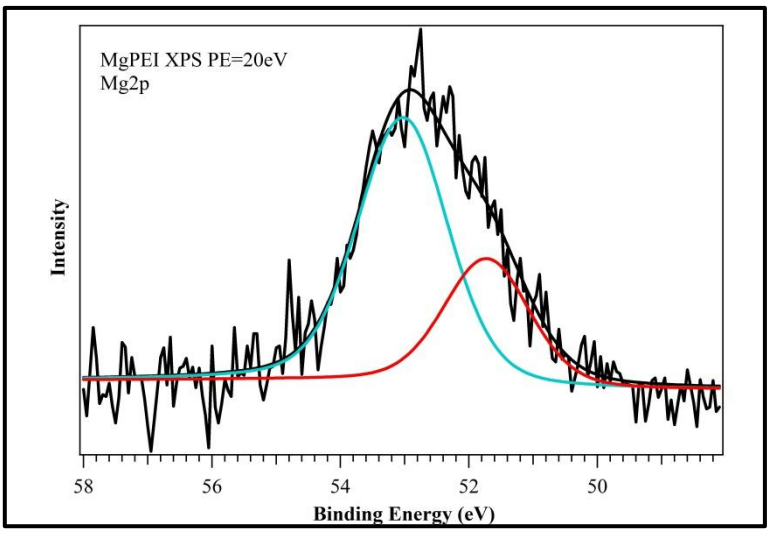

Figure 5.11 XPS Mg2p spectra of Mg nanoparticles embedded in PEI

5.3.3.5. Atomic and electronic structure characterization of Mg/PEI nanocomposites

Structural and morphological investigation were carried out using a sub-Angstrom aberration-corrected JEOL ARM200F microscope, equipped with an high resolution camera and scanning transmission electron microscopy systems (STEM) and analytical electron microscopy systems (EELS). The electron energy-loss spectroscopy (EELS) is an analytical technique that is able to give chemical information about the elements present into the investigated material. The sample preparation involves the nanocomposite dissolution in $CHCl_3$ at room temperature under stirring using an inert atmosphere; the solution was also sonicated for 30 minutes. The bottle containing the solution was sealed in an aluminum bag under nitrogen and opened just before the characterization. Then the sample was deposited on a grid of "lacey carbon only" and observed. The High Angular Annular Dark Field (HAADF)-STEM micrograph of Mg nanoparticles embedded in PEI (Figure 5.12, A) and the corresponding map of elements (Figure 5.12, B) were done by using the STEM microscopy operated at 200KeV. As it is visible from HAADF-S/TEM micrograph, smaller nanocrystals of ca. 5 nm forming large aggregates of about 20 nm were present. Each crystal shows a typical core-shell structure, which is well defined owing the different color areas in the map, according with the elements distribution in the aggregate.

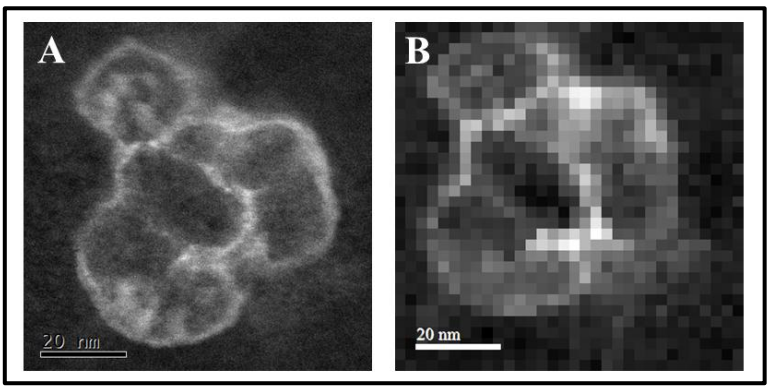

Figure 5.12 High Angular Annular Dark Field (HAADF) micrograph (A) and corresponding elements maps (B) of Mg nanoparticles in PEI, performed by STEM at 200KeV

The local electronic structure identified by the EELS spectroscopy shows the presence, in the shell, of oxygen and sodium. The EDS-TEM analysis revealed the presence of others impurities, such as silicon and calcium.

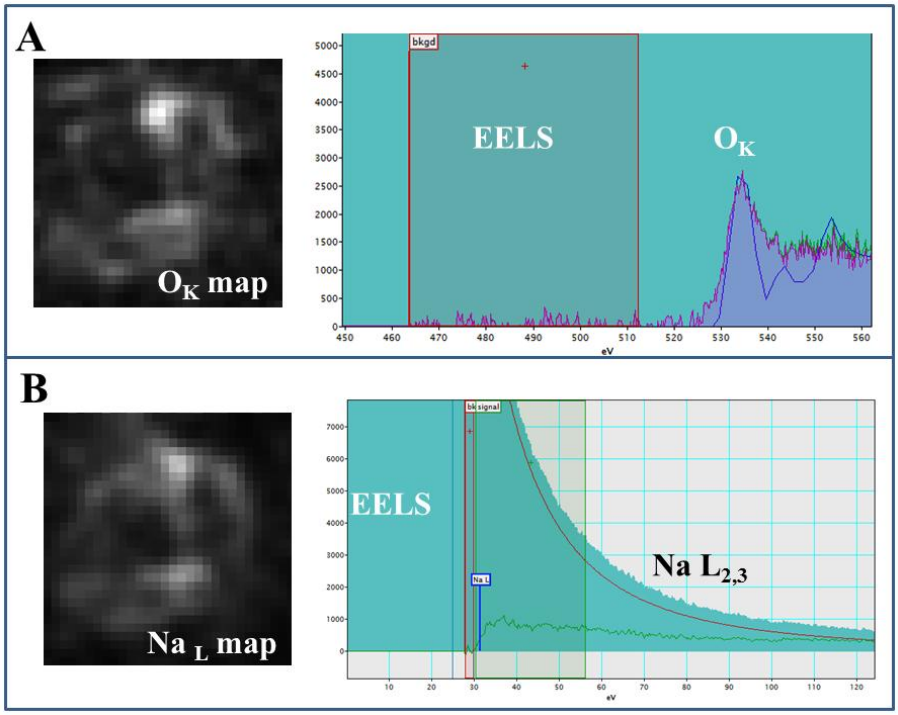

Figure 5.13 HAADF oxygen (A) and sodium (B) maps, with corresponding EELS spectra of Mg nanoparticles in PEI, performed by STEM at 200KeV

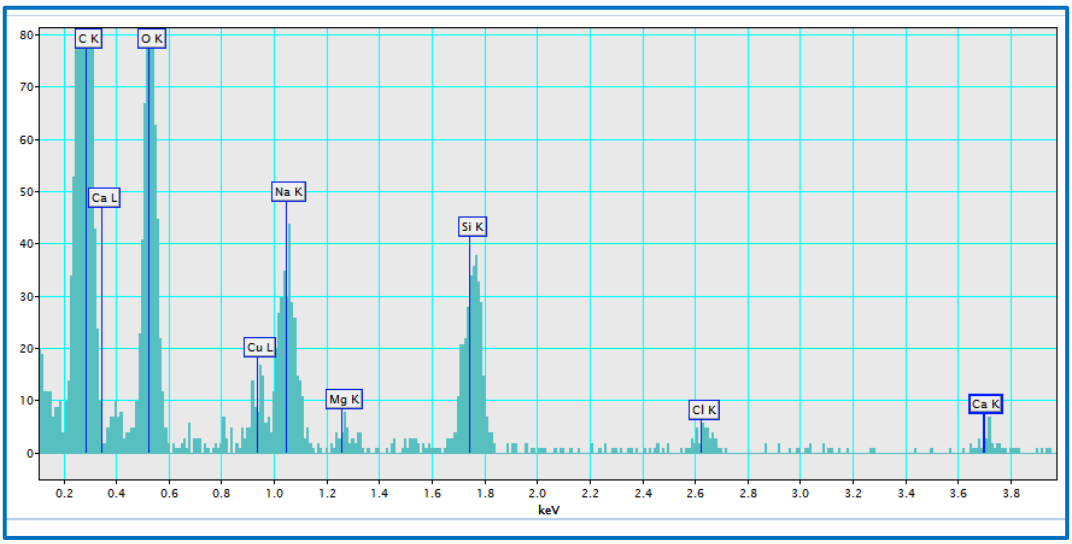

Figure 5.14 EDS –TEM of Mg nanoparticles in PEI, performed by STEM at 200KeV

The presence of these impurities can be attributed to the solvent used for grid preparation. This result was confirmed by both XPS analysis performed on the untreated

nanocomposite (as is shown in Figure 5.9) and by the EDS analysis performed on the untreated nanocomposite (see Table 5.1), where the sample was found to be quite free of impurities. The nanocomposite dissolved in chloroform (see Table 5.1) instead presented traces of impurities, in according with EDS-TEM graph.

The HAADF-STEM micrograph on a single crystal allows of identifying the crystal size, which was of ca. 5 nm. Simulated diffraction analysis was also performed (see Figure 5.15). The Fourier transform of the HAADF-STEM image on a single nanocrystal revealed spots corresponding to the lattice spacings of 110 and 002 at 200 kV, indicated with a green and yellow circles respectively, which was assigned of hexagonal magnesium particle. Thanks to this analysis was possible to identify a core-shell structure in which a magnesium metallic core was coated by a layer made of oxygen and others impurities, coming from the solvent selected. The Fourier transform of the HAADF-STEM (see Figure 5.16), performed both in the core and in the shell of the structure, confirm the presence of a Mg-core structure, covered by a shell made of Mg, O, Na, Ca and Cl. The sample resulted to be very sensitive to the electronic beam and it is easily charged. The sample vibration makes quite difficult to find the better conditions for aligning the beam and correcting the astigmatism. However, the images captured are useful representative for the material composition identification.

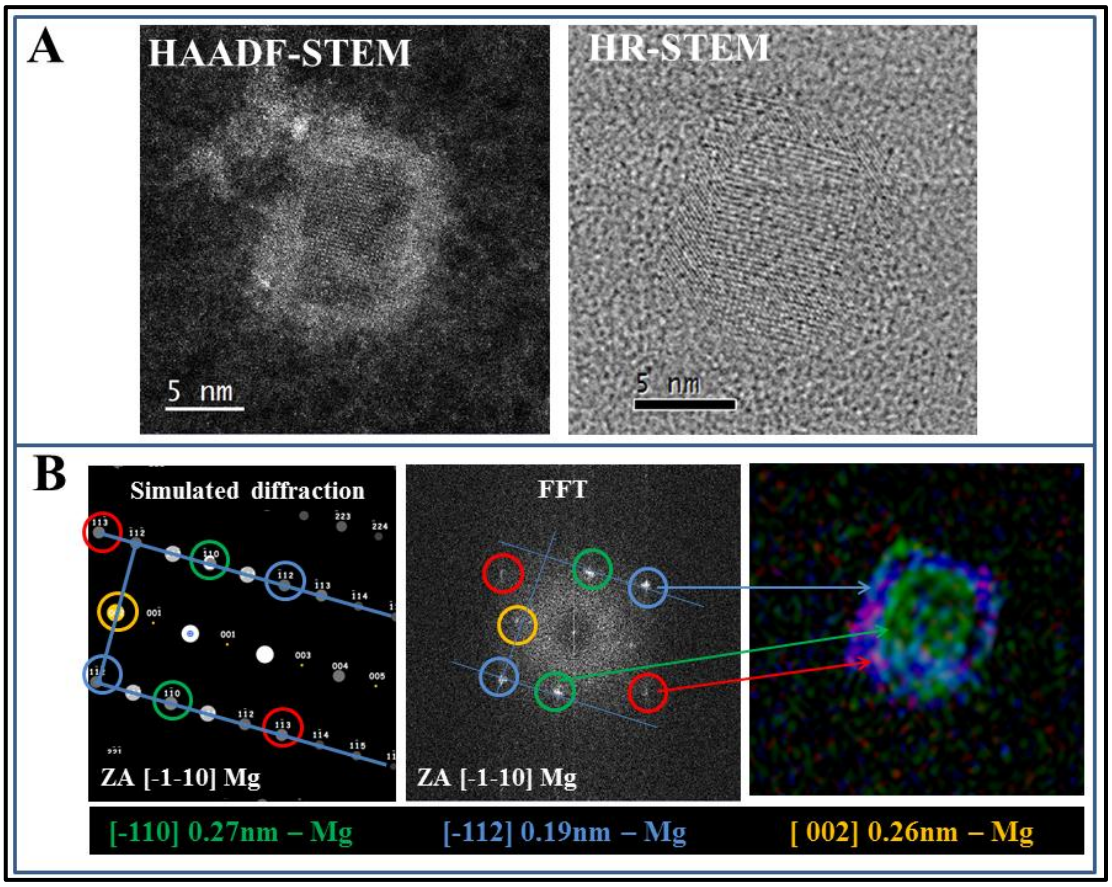

Figure 5.15 HAADF and HR-STEM micrographs (A) and corresponding Fourier transform of the HAADF-STEM image (B) of Mg nanocrystal in PEI, performed by STEM at 200KeV

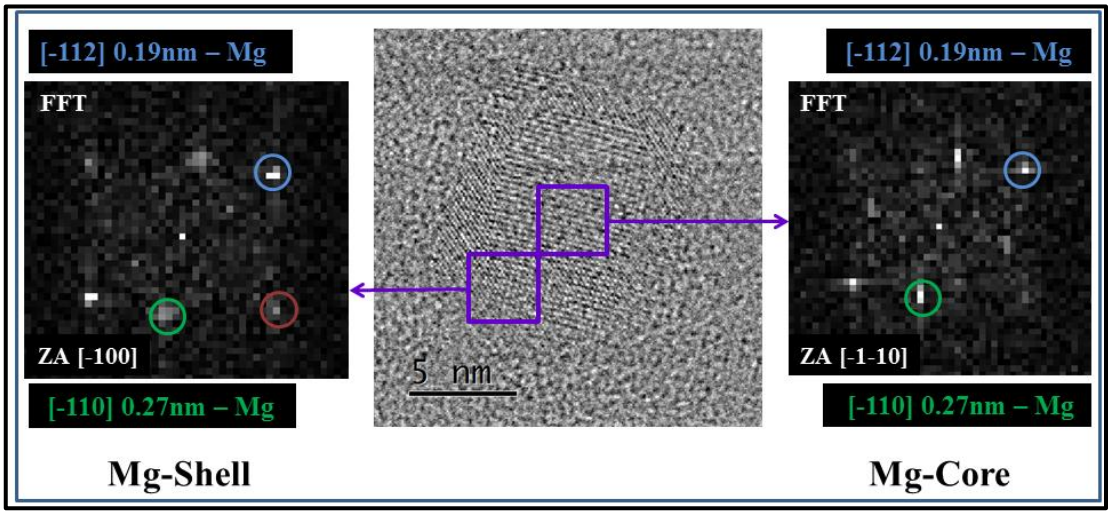

Figure 5.16 HR-STEM micrograph and simulated diffraction profile of the single Mg-nanocrystal in PEI, performed at 200KeV

5.3.3.6. Low temperature and pressure gas-sorption measurements in Mg/PEI nanocomposites

The adsorption–desorption isotherms of 8%wt Mg/PEI nanocomposites were measured for N_2 and H_2 gas at 77K, from 0 up to 1bar, by using a Micromeritics ASAP 2020 analyzer. All gases used were of 99.999% purity. The sample was sealed in an aluminum bag under nitrogen, opened just before the measurements. The sample was degassed at 120°C under vacuum (P < 10−5 mbar) for 10 hours, before testing. All the results are collected in the Table 5.2. The surface area was determined by using the Brunauer-Emmett-Teller (BET) equation, taking the data in the range P/P_0 = 0.05 – 0.3 (BET). The N_2 gas uptake was taken at 750mmHg, and the H_2 gas uptake was evaluated at 77K and 1bar.

Compound	BET surface area [m^2g^{-1}]	N_2 uptake [cm^3g^{-1}]	H_2 uptake [wt%]
8%wt Mg/PEI	4.57±0.05	13.09	0.05

Table 5.2 The BET surface area, N_2 and H_2 gas uptake of the 8%Mg/PEI nanocomposite, performed at 77K and from 0 up to 1bar

As it is evident, the measurements of gas sorption performed at low pressure and temperature has shown low BET surface area and N_2 gas uptake. Unlike other materials, such as MOFs, or carbon nanotubes, etc., having good intrinsic porosity, the PEI exhibited a very low surface area and poor adsorption properties in physisorption conditions. Moreover, the Mg nanocrystals embedded into the polymer probably occupies the surface and the space of the pores, according with some literature woks [8], affecting absorption properties of the nanocomposites. The H_2 sorption isotherms were monitored at 77K up to 1bar. The linear absolute isotherm plot, and the pressure-composition isotherm plot are reported in Figure 5.17, A and B, respectively. As it is visible the quantity of H_2 adsorbed at 77 K and 1 bar is very low, of ca. 6cm^3/g, as visible in Figure 5.17, A. Also the corresponding H_2 uptake capacity is very low (Table 5.2). Despite the small dimensions of the produced metal, the Mg/PEI nanocomposite has shown very poor hydrogen adsorption in the physisorption conditions. The chemisorption capacities will be evaluated in future.

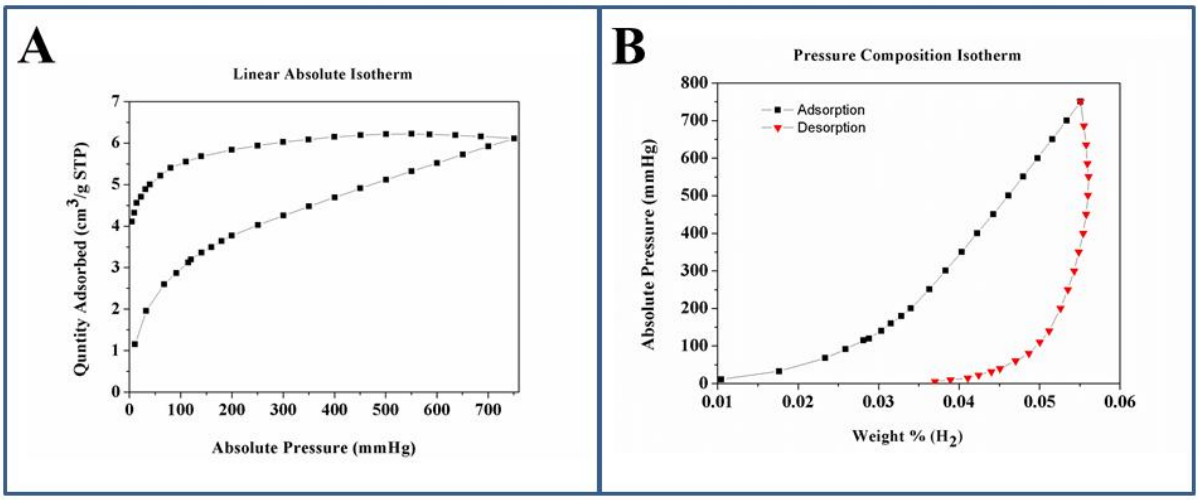

Figure 5.17 Physical H_2 adsorption/desorption measurement of 8wt%Mg/PEI

5.4. Conclusion

The synthesis and characterization of nanostructured magnesium into a polyetherimide (PEI) were performed. The PEI is a high performance polymer having good oxygen barrier properties. In according with the reaction mechanism proposed, the presence of metallic and oxidized magnesium phases were found by X-ray photoelectron spectroscopy (XPS) analysis. The scanning transmission electron microscopy (STEM) micrographs also revealed the presence of smaller Mg nanocrystals of ca. 5 nm forming large aggregates of ca. 20 nm. The Fourier transform of the HAADF-STEM image revealed the presence, for each single crystal, of a typical core-shell structure in which a magnesium metallic core was coated by a layer made of oxygen and other impurities coming from the solvent selected. The presence of a metallic core coated by an oxide shell indicates that magnesium originally consisted of pure zero-valent magnesium phase. This result can be expected because the magnesium is an “active” metal and probably, during the sample preparation for the microscopy observations, it can be easily oxidized. Also the small sizes of the produced metal and hence the nanostructuring effects, amplifies the interface phenomena and therefore the oxidation process. Several surface oxygen removal processes, such as hydrogen fluorination or hydrogenation processes, can be used for re-activating the metal nanoparticles and make them suitable for the storage application.

5.5. References

[1] G. Scherillo, M. Petretta, M. Galizia, P. La Manna, P. Musto, G. Mensitieri, Thermodynamics of water sorption in high performance glassy thermoplastic polymers, Front Chem. 2 (2014) 25. doi:10.3389/fchem.2014.00025.

[2] H.M. Relles, Synthesis and Properties of Polyetherimide Polymers, in: Contemp. Top. Polym. Sci., Springer US, Boston, MA, 1984: pp. 261–279. doi:10.1007/978-1-4613-2759-2_11.

[3] R.O. Johnson, H.S. Burlhis, Polyetherimide: A new high-performance thermoplastic resin, J. Polym. Sci. Polym. Symp. 70 (2007) 129–143. doi:10.1002/polc.5070700111.

[4] A.Y. Alentiev, Y.. Yampolskii, Free volume model and tradeoff relations of gas permeability and selectivity in glassy polymers, J. Memb. Sci. 165 (2000) 201–216. doi:10.1016/S0376-7388(99)00229-X.

[5] R.W. Baker, Membranes for vapor/gas separation, Membr. Technol. Res. Inc. (2006) 25.

[6] R. Scarlet, L.R. Manea, I.O.N. Sandu, L. Martinova, O. Cramariuc, Study on the Solubility of Polyetherimide for Nanostructural Electrospinning, Rev. Chim. 63 (2012) 688–692. http://www.revistadechimie.ro.

[7] K.L. Mittal, H. Electrochemical Society Symposium on Metallized Plastics (4th : 1993 : Honolulu, Metallized plastics : fundamentals and applications, Marcel Dekker, 1998.

[8] D.-W. Lim, J.W. Yoon, K.Y. Ryu, M.P. Suh, Magnesium Nanocrystals Embedded in a Metal-Organic Framework: Hybrid Hydrogen Storage with Synergistic Effect on Physi- and Chemisorption, Angew. Chemie. 124 (2012) 9952–9955. doi:10.1002/ange.201206055.

[9] P. Rizzo, A. Spatola, A. De Girolamo Del Mauro, G. Guerra, Polymeric films with three different uniplanar crystalline phase orientations, Macromolecules. 38 (2005) 10089–10094. doi:10.1021/ma051247p.

[10] C. Daniel, G. Guerra, P. Musto, Clathrate phase in syndiotactic polystyrene gels, Macromolecules. 35 (2002) 2243–2251. doi:10.1021/ma011531q.

[11] M.S. V Chã, P.P. Bittencourt, M.E. Sena, M.L.L. Paredes, G.F. Moreira, R.A. Reis, Synthesis and characterization of sulfonated poly(ether imide) with higher thermal stability and effect on CO2, N2, and O2 permeabilities, Mater. Res. 17 (2014) 714–

719. doi:10.1590/S1516-14392014005000012.

[12] M.S. V. Chã, P.P. Bittencourt, M.E. Sena, M.L.L. Paredes, G.F. Moreira, R.A. Reis, Synthesis and characterization of sulfonated poly(ether imide) with higher thermal stability and effect on CO2, N2, and O2 permeabilities, Mater. Res. 17 (2014) 714–719. doi:10.1590/S1516-14392014005000012.

[13] J.I. Langford, D. Louër, Powder diffraction, Reports Prog. Phys. 59 (1996) 131–234. doi:10.1088/0034-4885/59/2/002.

[14] L.S. Birks, H. Friedman, Particle Size Determination from X- Ray Line Broadening, J. Appl. Phys. 17 (1946) 687–692. doi:10.1063/1.1707771.

[15] H.R. Moon, J.J. Urban, D.J. Milliron, Size-Controlled Synthesis and Optical Properties of Monodisperse Colloidal Magnesium Oxide Nanocrystals, Angew. Chemie Int. Ed. 48 (2009) 6278–6281. doi:10.1002/anie.200902056.

[16] Q. Wang, X. Wang, X. Li, Y. Cai, Q. Wei, Surface modification of PMMA/O-MMT composite microfibers by TiO2 coating, Appl. Surf. Sci. 258 (2011) 98–102. doi:10.1016/j.apsusc.2011.08.013.

[17] S. Agarwal, N.S. Saxena, V. Kumar, Temperature Dependence Thermal Conductivity of ZnS/PMMA Nanocomposite, in: 2014: pp. 737–739. doi:10.1007/978-3-319-03002-9_190.

[18] C. Eaborn, Purification of Laboratory Chemicals, 1981. doi:10.1016/S0022-328X(00)82974-5.

[19] M. Kaba, N. Raklaoui, M. Françoise Guimon, A. Mas, Improvement of the water selectivity of ULTEM poly(ether imide) pervaporation films by an allylamine-plasma-polymerized layer, J. Appl. Polym. Sci. 97 (2005) 2088–2096.

[20] H.B. Yao, Y. Li, A.T.S. Wee, An XPS investigation of the oxidation /corrosion of melt-spun Mg, Appl. Spectrosc. 158 (2000) 112–119. doi:10.1016/S0169-4332(99)00593-0.

[21] O. Friedrichs, J.C. Sánchez-López, C. López-Cartes, M. Dornheim, T. Klassen, R. Bormann, A. Fernández, Chemical and microstructural study of the oxygen passivation behaviour of nanocrystalline Mg and MgH2, Appl. Surf. Sci. 252 (2006) 2334–2345. doi:10.1016/j.apsusc.2005.04.018.

Conclusion

The development of new materials represents the recent frontier in hydrogen storage technologies. In the last few decades the preparation of nanostructured materials has had an increasing interest, because the hydrogen storage capacity is closely linked to the material dimensions, and increases considerably with the reduction of the particles sizes. The chemical synthesis plays an important role in the development of new materials for hydrogen absorption because it allows a good control of the hydride phase sizing, and thus of the kinetics/ thermodynamics of such materials. The aim of the work concerns the synthesis by chemical techniques of metals nanoparticles. Nanostractured metals embedded into a polymeric matrix are prepared. The polymer was used for achieving nanoparticles with tailored properties.

In the first part of this work, the synthesis of Pd clusters embedded into poly-(N-vinyl-2-pyrrolidone) (PVP) is presented. Nanostructured palladium is one of the most investigated model system for understanding the hydrogen interaction with metal surfaces. Then nanostructured Mg composites generated both into a poly(methyl methacrylate) (PMMA) and polyetherimide (PEI) matrix are also presented.

At the beginning a very simple way for Pd clusters synthesis has been investigated. The chemical reduction process of a palladium salt (potassium tetrachloropalladate(II), K_2PdCl_4, reduced by the ethylene glycol, (EG)) in presence of surface stabilizers, was investigated. Thanks to this chemical approach and an appropriate control of the process conditions, extremely small crystals of about 2.6 nm, uniformly distributed in the polymer, have been obtained. Despite the low hydrogen storage capacity of palladium, the study of the processes involved in the nanoclusters production allowed to understand the general approach to be used for the nanostructured H_2-storage materials preparation. In addition, the palladium plays an important role in the H_2-dissociative adsorption on its surface, followed by H atoms diffusion to the support on which it is deposited (spillover mechanism). Smaller particles increase the hydrogen storage capabilities. Future work will focus on depositing Pd clusters on nanostructured magnesium for increasing the magnesium H_2 absorption capacity.

In the second part of this work, it has been proposed an innovative method for the Mg-based nanocomposites materials preparation, which is based on the thermolysis of an organometallic compound, the bis(η^5-cyclopentadienyl)magnesium(II) (Cp_2Mg), dissolved

in two different polymers. Firstly, the synthesis and the characterizations of nanostructured magnesium composites into a poly(methyl methacrylate) (PMMA) matrix is presented. This preparation involves two steps, the first step is used for the Cp_2Mg/PMMA solid solution preparation, and the second step consist of a thermal annealing treatment, which is used for the precursor (Cp_2Mg) decomposition and nanostructured Mg-composites precipitation. Since the magnesium compounds are air-sensitive materials, all the synthesis procedures were performed in inert atmosphere using a glove box. Early results performed by X-ray photoelectron spectroscopy allowed to establish that the magnesium produced in PMMA resulted oxidized by ca. 30%. The structural and morphological investigations performed by scanning transmission electron microscopy at high voltage, highlighted the presence of partially oxidized magnesium nanocrystals, of ca. 2nm.

In the last part of this work some strategies used to prevent the Mg nanocrystals oxidation are presented. The synthesis of nanostructured magnesium into a polyetherimide (PEI) matrix is described with the characterizations procedures. The PEI is a new high performance amorphous thermoplastic polymer with high oxygen permeation barrier properties. Different process conditions were used, like different annealing temperatures and a new thermolysis apparatus design. A novel design for the thermolysis apparatus was developed. The spectroscopic characterization of the Mg/PEI nanocomposites performed by X-ray photoelectron spectroscopy showed the presence of Mg and MgO mixture on the nanocomposite surface. Very interesting results are achieved with the structural and morphological investigations performed by the scanning transmission electron microscopy at high voltage. In particular, smaller Mg nanocrystals of ca. 5 nm, forming large aggregates of ca. 20 nm, were observed. Each crystal shows a typical core-shell structure in which a magnesium metallic core is coated by a layer made of oxygen and others impurities. The presence of a metallic core and an oxide shell indicates that nanocrystals were originally made of zero-valent magnesium. In fact magnesium is an “active” metal and probably, during the sample preparation for the analysis, it undergoes an oxidation process. It must be pointed out that the small dimensions of the produced metal, and hence the nanostructuring, enhance interface oxidation phenomena. However, some oxygen surface removal techniques, like hydrogen fluorination or hydrogenation treatments, can be used for re-activating the metal nanoparticle surface making them as suitable for the storage application. A possible future research activity in this field can be related to the removal of the oxide layer and testing the hydrogen adsorption/desorption ability of developed materials.

Appendix A

Manipulation of air sensitive compounds

The manipulation of the air-sensitive compounds [1] is based on the use of an inert gas atmosphere to exclude the air. This approach may be further subdivided into those techniques which involve bench-top operations, with special glassware (often called Schlenk techniques) or the glove box techniques, in which manipulations are performed in a chamber filled with inert-atmosphere. The principal advantages of the dry box concern its use for complex manipulations of solids, and for compounds showing particular features, as high air reactivity (spontaneous ignition) and autocombustion.

The nanostructured magnesium composites preparation has implied the use of an air sensitive organometallic compound, the bis(η^5-cyclopentadienyl)magnesium(II) (Cp_2Mg). The raw materials obtained commercially were opened only after stocking in the glove box. Anhydrous solvents were selected, to avoid the water presence. The preparation of the nanostructured magnesium composites has involved two process steps: the first step concerns the polymer/precursor solid solutions preparation, and the second step concerns the thermal annealing of that solid solution. The first annealing tests were done using a ceramic hot plate, placed into the glove box. Since it was noted that the ceramic hot plate was unable to guarantee a good temperature control, the second class of nanocomposites materials were annealed in a tubular oven under nitrogen gas atmosphere. Some improvements on the thermolysis apparatus design were performed. A “sample transport device” system was designed to move the sample, under inert atmosphere, from the glove box in which the solid solutions were prepared to the tubular oven, and to come back in the glove box. The whole process apparatus will be described.

A.1. Glove Box

The glove box was a “LABmaster Up” glove box workstation[4] from MBraun (see Figure A.1) operating under nitrogen atmosphere, equipped with an oxygen and humidity controller working at <0.1ppm and <0.1ppm contents, respectively. The pressure in a dry box must be close to 1atm, for easy manipulation of the gloves. Significant deviation from 1atm for a non-evacuable glove box can damage the windows, gloves or box walls. A pressure controller helps to keep the desirable pressure, because large fluctuations in the dry box pressure can be result from running the gloves in and out during the manipulations. The chamber is also equipped by a pre-chamber having an autoclave-type closure, a centrally located screw and evenly distributed clamps and bolts. The pre-chamber is used for inserting and picking of the samples and reagents from the main chamber.

Figure A.1 Glove Box apparatus

Vacuum and nitrogen cycles are carried out to get and remove the materials from the glove box. Gas purification cycles have been periodically performed to keep oxygen and humidity values within the chamber sufficiently low.

[4] The glove box was supplied by the "***Nanomaterials and Devices Laboratory***" - SSPT-PROMAS-NANO Division of ***ENEA*** (National Agency For New Technologies, Energy and Sustainable Economic Development), under the Dr. Carmela Borriello supervision.

A.2. Thermolysis Apparatus Scale-up

An apparatus for thermolysis of the Mg/PEI nanocomposites was carried out. The thermolysis apparatus configuration is shown in Figure A.2. The tubular oven was connected to a nitrogen stream to guarantee the inert atmosphere during the heat treatment. The tubular oven from "Barnsted / Thermolyne" was equipped with a thermoregulator of the "Eurothterm" model 2116.

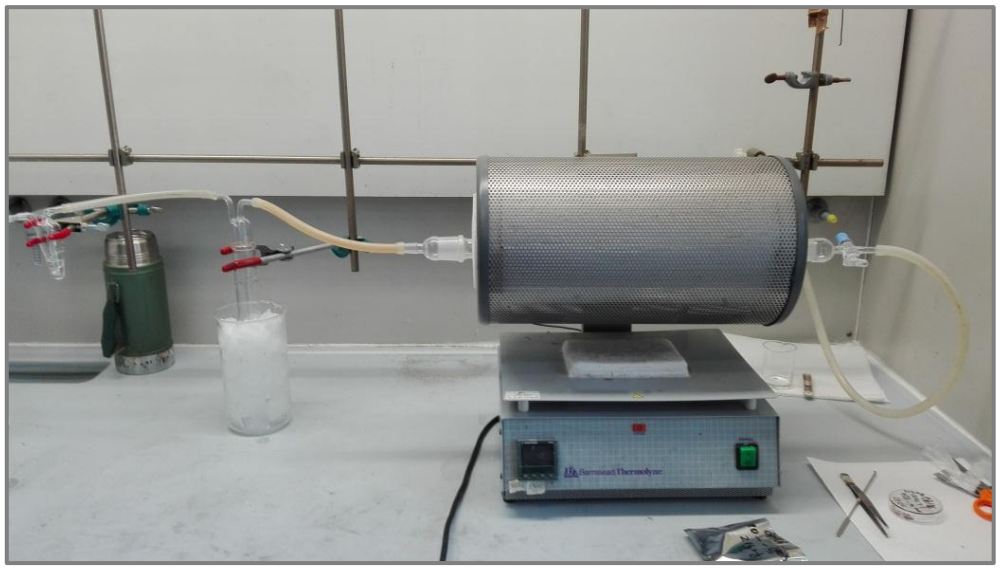

Figure A.2 Thermolysis apparatus configuration

The thermolysis apparatus configuration was constituted of a nitrogen stream connected to the oven input position. A "Glass Ice Cold Trap" partially filled with ethylene glycol, was placed in the output, and an oil bubbler was connected to it. The trap was immersed in an ice and salt bath (the NaCl salt was used to stabilize the temperature below 0 °C) for cooled down the gaseous phases produced during the reactions. The "Oil bubbler" partially filled with silicone oil, was used to check the nitrogen fluxing.

Preliminary temperature calibration tests were performed by using a K thermocouple. Type K Thermocouple (Nickel-Chromium/Nickel-Alumel) was used, working in range temperatures from –270 to 1260°C, with accuracy of +/- 2.2°C. The calibration was performed under nitrogen atmosphere. The thermocouple was put inside the tube, in the side of the out of the gas flow. A schematic representation of the tubular oven and the calibration plot are reported in Figure A. **3**. As visible in Figure A. **3**- A, the total oven length was of 49cm. The sample will be placed in a ceramic combustion boat of 9 cm length, thus the calibration was performed at 24.5cm, in the oven center. The side of the

output of the gas corresponds to the side of the inlet of the thermocouple (see Figure A. **3**-A). A temperature values, ranging from 50 to 600°C, were selected on the thermoregulator. After the oven thermal stabilization, the temperature values were read by both on the oven thermoregulator and on the thermocouple. The calibration plots were reported in Figure A. 3, B.

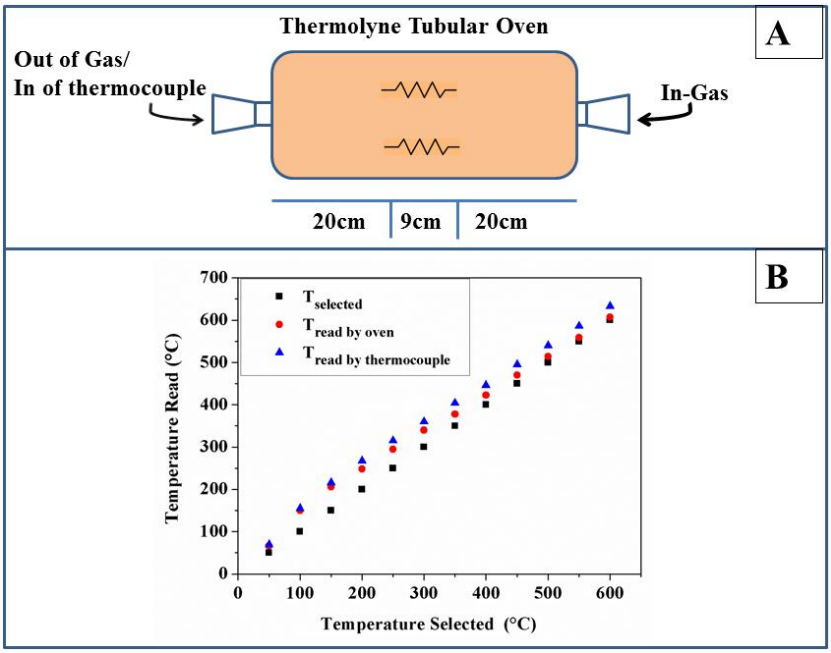

Figure A. 3 Schematic representation of the tubular oven (A) and calibration plots (B): the black points are the T selected, the red points are the T values read by oven and the blue points are the T values read by the thermocouple

As visible a little deviations by the "set point" temperature values was noted, by both for the oven and for the thermocouple plots values. The temperature overshoot was aligned selecting the running rate at 10°C/min. With this calibration was possible to determine the exactly temperature to the center of the oven, where will be placed the samples (at 24.5 cm).

A.3. Improvement made on the apparatus: sample transport device

A "***sample transport device***" system was designed to move the sample, under inert atmosphere, from the glove box, in which the solid solutions were prepared, to the tubular oven, and to come back in the glove box. A careful design of the sample transport device has been developed. The schematic representation and corresponding real picture of the sample transport device are reported in Figure A.4. The device was constituted by a tube of glass and two flow adapters, for the flux nitrogen gas. The In/Out of the gas flow are

shown in Figure A.4, A. The adapters distance must be higher than the ceramic boat length (of 9cm), to guarantee an in inert atmosphere to the sample. At the same time the total device length must be lower than to the glove box pre-chamber length, to allow the inlet of the device into the chamber (to put and take the samples from the glove box). One side of the tube has designed to be adapted to the quartz tube of the tubular oven, to be connected to it (see Figure A.4, B). The other side was used to move, by using an iron rod, the sample into the oven center.

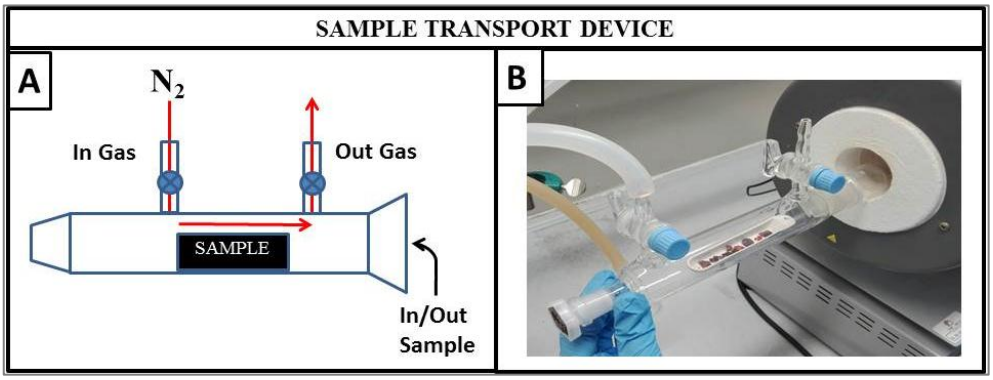

Figure A.4 Schematic representation (A) and real picture of the "sample transport device"

The reaction process was be the following: the solid solutions were prepared in glove box; then the sample transport device containing the ceramic boat was get into the glove box, to take the sample. After the sample placing in the ceramic boat, the flow adapters were closed, and the sample transport device was brought to the oven, for the nanocomposites thermolysis. Here a silicone tube was connected to the "In Gas" adapter (see Figure A.4) and the nitrogen flux opened. At the same time the "Out gas" adapter was opened, to allow the nitrogen fluxing. The sample transport device was connected to the quartz tube of the tubular oven (see Figure A.5, C), and the ceramic boat was put in to the oven center by using an iron rod (see Figure A.5, D). The thermolysis apparatus was reported in the configuration of Figure A.6. In this configuration the nitrogen gas flow in the inlet was splitted into two fluxes, one is used for the oven and the second flux of nitrogen is used for the sample transport device. After these preliminary procedures the thermolysis can be play. The nanostructured magnesium composites were annealed in a tubular oven for 10 minutes at 330°C. At the end of the process the nanocomposites were left in the oven, and then cooled down at room temperature. After that, the sample transport device was again connected to the oven, to take the sample. The second flux of nitrogen is opened. Taking the sample, the two flow adapters were closed, thus to guarantee the inert atmosphere to

the sample, and the device was placed into the glove box. Only when the device was in glove box was opened. Then the sample was sealed in aluminum bags, to be opened just before the characterizations.

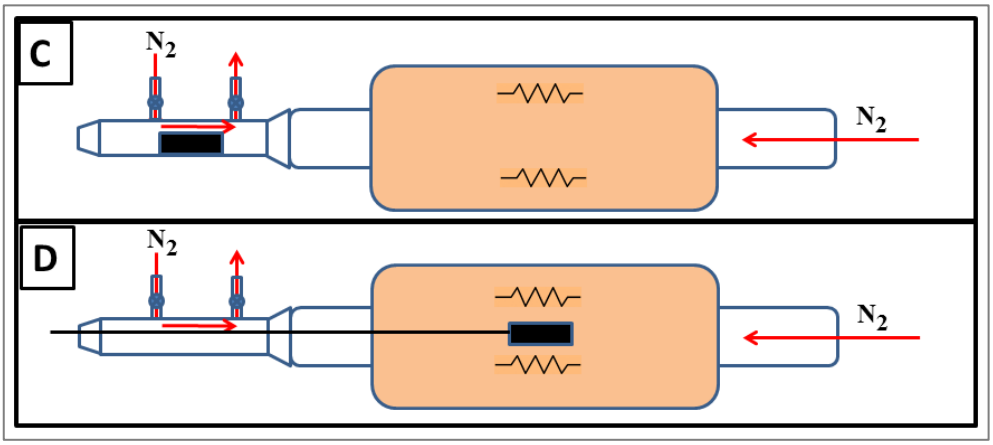

Figure A.5 Schematic representation of the nanocomposites placement in the oven (C and D)

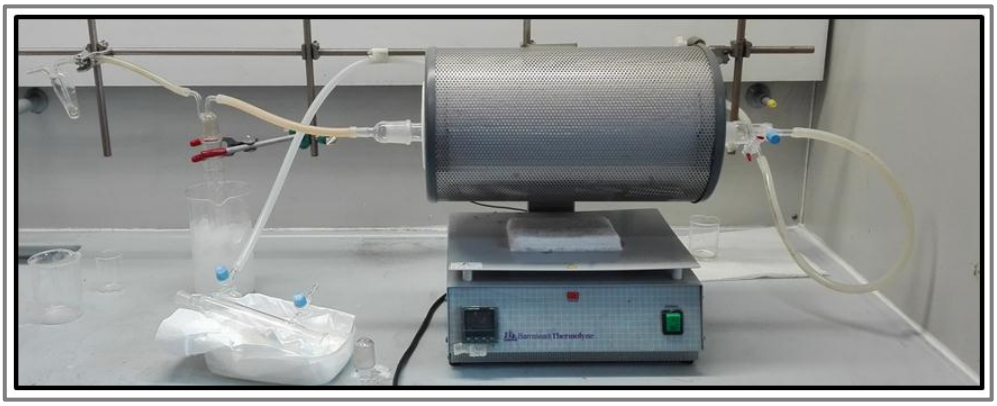

Figure A.6 Real picture of the complete thermolysis apparatus

A.4. References

[1] D.A. Shriver, M.A. Drezden, The manipulation of air-sensitive compounds, Wiley-Interscience, New York, 2nd Ed. (1986) 1–335. doi:10.1016/0022-328X(87)80317-0.

Appendix B

Characterization techniques

In this section the characterization techniques used for the palladium and magnesium crystals embedded into a polymer matrix are described. Characterization contains two main categories: structural analysis and property measurements. Morphological and structural analyses are carried out using a variety of microscopy and spectroscopy techniques, while the property characterization is performed by using specific measuring techniques.

B.1. Transmission Electron Microscopy (TEM)

The transmission electron microscopy (TEM) is a powerful technique for the direct detecting of nanoparticles because it can provide a real space image on the atom distribution in the nanocrystal and on its surface. TEM is versatile tool that provides not only atomic-resolution lattice image, but also chemical information at a spatial resolution of 1nm or better, allowing direct identification the chemistry of a single crystal [1]. A modern TEM can be schematically shown in Figure B.1, which is composed of an illumination system, a specimen stage, objective lens systems, the magnification system, the data recording system(s), and the chemical analysis system. The electron gun is the heart of the illumination system, which typically uses a LaB_6 thermionic emission sources or a field emission source. The LaB_6 gun gives a high illumination current but the current density and the beam coherence are not as high as those of the field emission source. Field emission source is unique for performing high coherence lattice imaging, electron holography and high spatial resolution microanalysis. The illumination system also includes the condenser lenses that are vitally important for forming a fine electron probe. Specimen stage is the key for carrying out structure analysis, because it can be used to perform in-situ observations of phenomena induced by annealing, electric field, or

mechanical stress, giving the possibility to characterize the physical properties of individual nanostructures. The objective lens is the heart of a TEM, which determines the limit of image resolution.

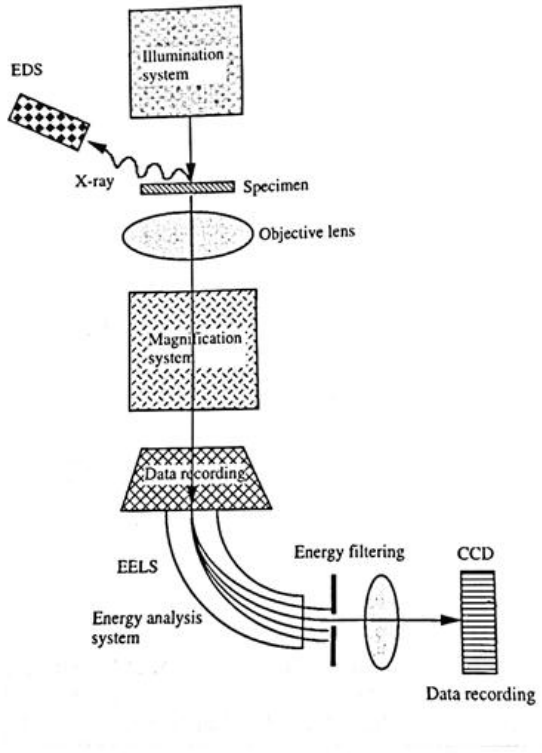

Figure B.1 Schematic structure of a transmission electron microscope

The magnification system consists of intermediate lenses and projection lenses and it gives a magnification up to 1.5 million. The data recording system tends to be digital with the use of a charge coupled device (CCD), allowing quantitative data processing and quantification. Finally, the chemical analysis system is the energy dispersive X-ray spectroscopy (EDS) and the electron-loss spectroscopy (EELS), both can be used complimentary to quantify the chemical composition of the specimen. EELS can also provide information about the electronic structure of the specimen.

A sample shaped as a thin film is transilluminated by a beam of accelerated electrons with an energy of 50-200keV in vacuum of ca. 10^{-6}mmHg.Those electrons that were deflected at small angles by atoms in a sample and passed through the sample get into a system of magnetic lenses to form a bright-field image of the sample internal structure on a screen and a film. A resolution of 0,1nm was achieved, which corresponds to a magnification

factor of 106. The resolution depends on the nature of the sample and the method of its preparation. Usually, film of 0,01-μm thickness are studied.

A transmission electron microscopy (TEM) "**FEI Tecnai G2 Spirit TWIN 120 kV with LaB_6 source**" was used for the morphological characterizations. The palladium and magnesium crystals embedded into a polymer matrix were usually dissolved in an appropriate solvent at room temperature, and a drop of such solution was placed on the Formvar-coated copper grid and successively observed. Only for the Mg/PMMA sample, a solid thin film using an ultramicrotome was prepared and observed, in order to compare the results with that prepared in solution. A part of this sample was embedded into liquid epoxy resin. The resin was degassed before its inlet into a glove box. A sample piece was placed in a silicon mold, and then the liquid resin was poured onto it. All the procedures were performed in inert atmosphere. The composite resin-Mg/PMMA was left for 4 days in glove box for curing, before its observation. A film of the resin-Mg/PMMA was prepared using an "ultramicrotome diamond knife" (DIATOME Ultra Diamond Knife). The ultra-knife (in the triangular holder) with a cutting range of 30nm-2μm for dry sectioning of epoxy resin embedded samples is used. The gliding of the sections on the dry knife surface allows to obtain sample of thickness between 30-150nm, that correspond to an optimal thickness range for TEM investigations (electron transparency). The sample sections (or film) were collected in water and deposited on a Formvar-coated copper grid and successively observed.

The nanostructured magnesium composites were also studied by means of atomic-resolution imaging and spectroscopic techniques like the low energy aberration-corrected scanning transmission electron microscopy (STEM) together with atomic-resolution electron energy-loss spectroscopy (EELS). The analyses were performed by using a "**sub-Angstrom JEOL JEM-ARM200F**" Transmission Electron Microscopes, installed at IMM-CNR5 of Catania, thanks to the Beyondnano project. This facilities has exceptional features which make one the most powerful analytic electron microscope in Europe. Its sophisticated hardware configuration combines spatial resolution and chemical contrast on a single image, allowing, element by element, the identification of the atomic structure of materials even at very low beam energy. The workstation, called "The Active Lab", is equipped with active suspension system, system for compensation of electromagnetic fields, radiant panel with control of the thermal stability of 0.06 °C/h, sound proof walls

[5]Istituto per la Microelettronica e Microsistemi (CNR-IMM), VIII Strada 5, I-95121 Catania, Italy.

able to reduce more 1000 times outside noise. The Transmission Electron Microscopes "JEOL JEM-ARM200F" picture is reported in Figure B.2. The microscope consists of a probe corrected STEM microscope equipped with a cold field emission gun (40-200kV C-FEG with 0.27eV energy spread) and a fully loaded GIF Quantum ER as EELS spectrometer.

Figure B.2 Transmission Electron Microscopes "JEOL JEM-ARM200F"

The spherical aberration correctors were STEM correctors of "Ceos sextupole Cs aberration corrector" on the probe for 0.64 Å STEM, for image-and probe-forming systems. This particular installation is capable of delivering a probe size of 0.68 Å at 200 kV and an energy spread better than 0.3eV. The microscope was aligned under diffraction mode, with parallel beam illumination. The EELS spectrometer was set to 0.025eV dispersion, yielding 0.5eV energy resolution. Such energy resolution is sufficient to reveal different features in the low loss region of the spectra. Each acquisition was obtained by averaging different aligned spectra. For each spectrum the exposure time was fixed at 0.02s.The atomic resolution STEM High-Angle Annular Dark-Field (HAADF) images and atomic EELS measurements were performed at 200 kV. The EELS spectra were taken by scanning the electron beam across the interface in the high angle annular dark field (HAADF) STEM images. The Fourier transforms of raw high angle annular dark field (HAADF) images are able to reveal the spots corresponding to the lattice index of the detected element. The energy-dispersive X-ray spectroscopy is performed to identify the chemical composition.

B.2. Scanning Electron Microscopy (SEM)

The scanning electron microscopy (SEM) is mainly useful for giving a three-dimensional image of the surface of the sample. Scanning electron microscopy is a high resolution microscopy technique based on using a focused beam of electrons to irradiate a sample material in order to investigate its surface, morphology and composition. Interaction of beam electrons with sample's atoms produces several signals containing information about the material. As with TEM, the samples are exposed by an electron beam, but instead of the electrons being transmitted through the sample, the beam is "scanned" by all, creating a sample surface image with exceptional depth of field. Figure B.3 shows a schematic representation of an SEM [2].

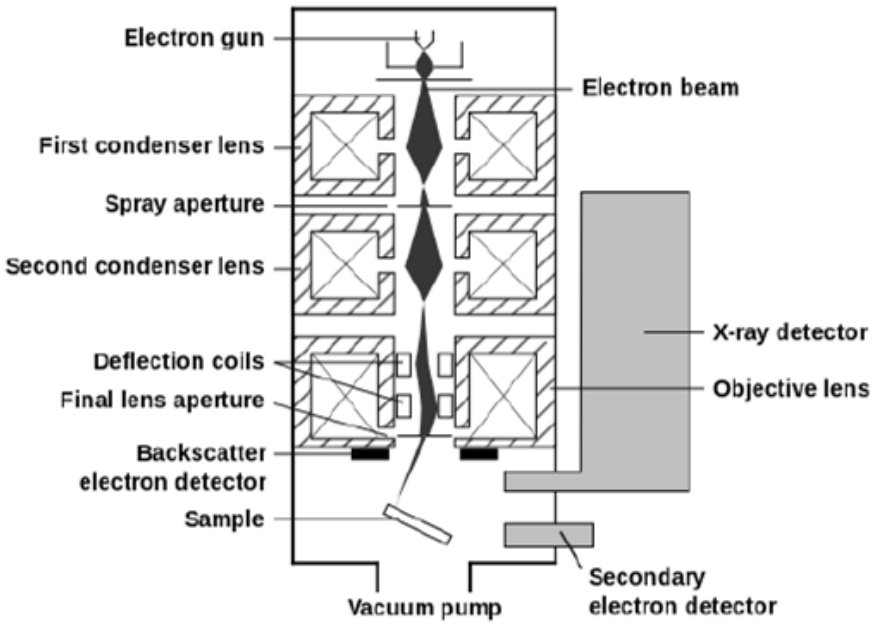

Figure B.3 Scheme showing the main components of a scanning electron microscope

The electron gun at the top of the column produces an electron beam that is accelerated and passes through a series of electromagnetic lenses and apertures. In this way, the electron beam is focused into a fine spot as small as 1 nm in diameter on the specimen surface. A final lens deflects the beam in the x and y axes so that it scans in a raster fashion over a rectangular area of the sample surface. Interaction of the electron beam with the sample results in the generation of a variety of signals: reflected electrons, secondary electrons,

Auger electrons, transmitted electrons, cathodoluminescence (photons) and X-rays. All these phenomena are interrelated and all of them depend to some extent on the topography, the atomic number and the chemical state of the specimen. Different types of signals can emerge from different volumes of interaction (see Figure B.4).

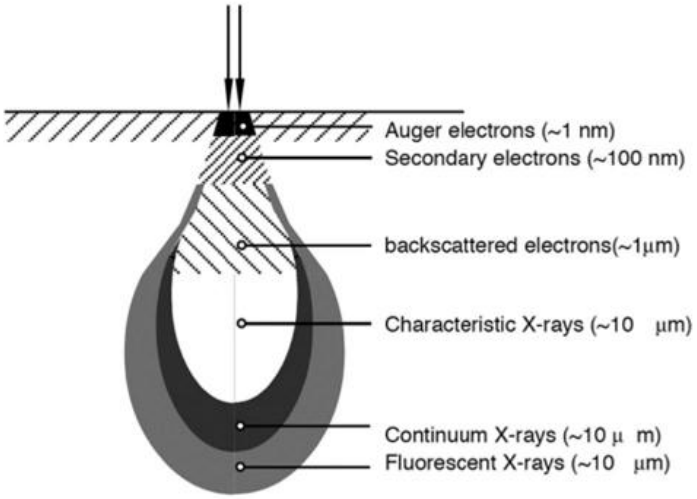

Figure B.4 Interaction volume for the various scattering types, and imaging modes. Backscattered electrons are seen to have a much larger interaction volume than secondary electrons.

The size and the shape of the volume depend on many factors, including beam energy and sample composition. The signals are stored in computer memory and then mapped as variations in brightness on the image display. The most commonly imaged signals in SEM are secondary electrons and back-scattered electrons. Characteristic X-rays are also widely used in SEM for elemental microanalysis (in this case a specific detector is required).

Secondary electrons (SEs) are produced as a result of the interactions between energetic beam electrons and the weakly bound conduction-band electrons in metals or valence electrons in semiconductors and insulators. Secondary electrons have low kinetic energy (< 50 eV) so only the electrons produced near the surface can escape from the sample. The signal of SEs varies with the topography of the sample surface much like an aerial photograph: edges are bright, recesses are dark. Indeed, the main cause of the image contrast is the existing angle between the incident beam and the surface. The ratio of the size of the displayed image to the size of the area scanned on the specimen gives the

magnification. Increasing the magnification is achieved by reducing the size of the area scanned on the specimen.

Backscattered electrons (BSEs) are elastically scattered electrons by the nuclei of the atoms in the specimen. BSEs exit from the surface with a high energy and contain information on chemical composition of the elements in the specimen. The number of BSEs increases with the atomic number Z of the atoms, so a material with a high Z will appear brighter on the image than a material having a lower Z.

The interaction volume for the various scattering types and imaging modes is illustrated in Figure B. 5 where BSE electrons are seen to have a much larger interaction volume than SE electrons. The larger interaction volume results in BSE mode having a lower resolution than SE mode.

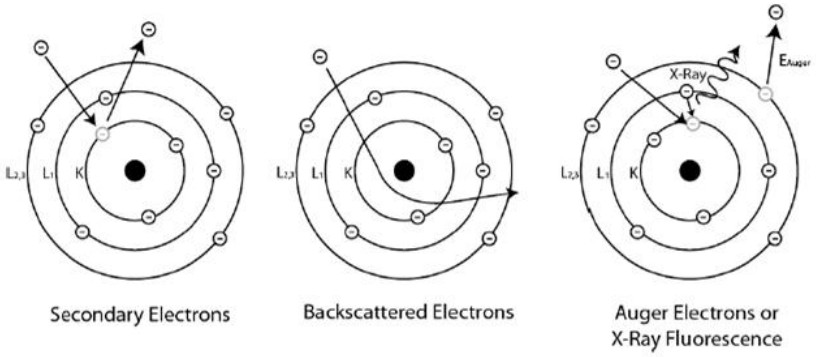

Figure B. 5 Various modes of electron emission from incident x-rays or electrons

During inelastic scattering of the beam electrons, x-rays can be formed by two distinctly different mechanisms: Bremsstrahlung and inner-shell ionization processes. In the first case, beam electrons undergo deceleration in the Columbic field of the atom and the lost energy is emitted as x-rays. Because of the random nature of this interaction, the electron may lose any amount of energy in a single deceleration event. This results in a continuum spectrum of x-rays, which is not useful for material's analysis. In the second case, a beam electron interacts with a tightly bound inner-shell electron, ejecting the atomic electron and leaving a vacancy in that shell; the atom is left as an ion in an excited state and relaxes to its ground state through a limited set of allowed transitions of outer-shell electrons to fill the inner-shell vacancy. The energies of the electrons in the shells are sharply defined, with values characteristic of the atomic species. The energy difference of the transition is therefore also a characteristic value, and this excess energy can be released from the atom in one of two ways:

1. in the Auger process, the difference in shell energies can be transmitted to another outer shell electron, ejecting it from the atom as an electron with specific kinetic energy;
2. in the characteristic x-ray process, the difference in energy is expressed as a photon of electromagnetic radiation that is sharply defined in energy, in contrast to the bremsstrahlung process, which produces photons spanning an energy continuum.

The number and energy of the characteristic x-rays can be measured by an energy-dispersive spectrometer (EDS), which provides information about the elemental composition of the sample and concentration of each element.

The SEM and the energy-dispersive X-ray spectroscopy (EDS-SEM) measurements were performed by using a Scanning Electron Microscopy "**FEI Quanta 200 FEG**". A small sample fragment was placed on a bi-adhesive graphite sticker, attached on an aluminum stub. Coating of samples is required in the field of electron microscopy to enable or improve the imaging of samples. Creating a conductive layer of metal on the sample inhibits charging, reduces thermal damage and improves the secondary electron signal required for topographic examination in the SEM. For the elemental composition analysis the sample was observed without using any coating.

B.3. X-ray diffraction (XRD)

X-ray diffraction (XRD) is a fundamental technique for both qualitative and quantitative analysis of crystalline solid materials. The diffraction phenomenon is based on the fact that the wavelength of X-rays (1 Å) is of the same order of magnitude as the interatomic distances (ca. 0.5-2.5 Å). Therefore, a crystal behave as a 3-D grating to an incident beam of X-rays and the resulting diffraction pattern can be used to determine the crystal structure of a material together with its composition. Diffraction is usually explained using Bragg's Law:

$$n\lambda = 2d\sin\theta$$

where λ is the wavelength of the incident beam, d is the perpendicular distance between lattice planes and θ, known as Bragg angle, is the angle of incidence. The n parameter is an integer number that represents the order of the reflection: when n = 1 the reflections are called first order, when n = 2 they are called second order and so on. As shown in Figure B.6, two parallel X-rays beam A and B with a certain wavelength λ and an incidence angle θ are 'reflected' by adjacent crystal planes.

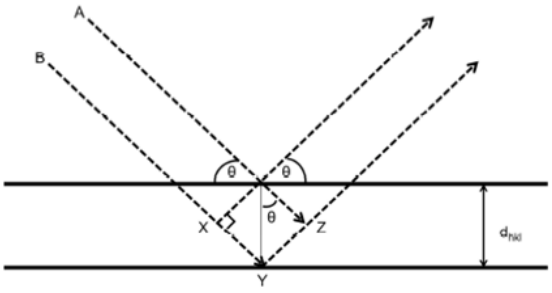

Figure B.6 Schematic of diffraction of a crystal used for deriving Bragg's law

In the case of powdered materials, the sample can be considered as a large number of small randomly oriented crystallites. In a crystal, the unit cell represents the simplest repeating unit of the crystal structure: it has the full symmetry of the crystal and it continuously repeats in all directions. The common way to describe it is by defining symmetry, shape and size, where a, b and c are the lengths and α, β and γ are the angles of the unit cell. The orientation of the crystal planes can be defined by the Miller indices (hkl) which indicate the reciprocal values of the positions where the plane intersects the a, b and c axes respectively. The Miller index values (hkl) can be positive, negative or null. The value of d_{hkl} can be determined for each of the crystal systems. The equations for calculating the interplanar distances can be combined with Bragg's law to determine the unit cell dimensions as part of the indexing process.

It is important to note that X-rays are scattered by electrons rather than by atomic nuclei and the active scattering centers are given by the electron density distributed in the crystal lattice. Therefore, how well an atom or a material diffracts depends upon the number of electrons present. Atoms with a greater number of electrons (with higher atomic number, heavier atoms) will scatter X-rays more effectively, resulting in a greater intensity of the observed diffraction peaks. On the other hand, materials containing lighter elements such as hydrogen or lithium (the atomic numbers are 1 and 3 respectively) or magnesium too, will not scatter strongly when in presence of heavier atoms.

X-ray powder diffraction (XRD) patterns were recorded on a "**Bruker D8 advance X-ray diffractometer"** employing CuKα radiation (λ =1.5406Å) with 40kV and 40mA. The specimen preparation was performed under N_2 atmosphere in the glove box. The sample was opened just before the measurements, and the test were performed in air. The crystalline structure of the material can be obtained by comparing the peak positions with those collected in the Power Diffraction Data File (JCPDS data collection).

The determination of Pd clusters embedded in PVP was determined by using the Scherrer's equation:

$$D = k \frac{\lambda}{\beta \cos\theta}$$

Where D is the mean size of the ordered (crystalline) domains, which may be smaller or equal to the grain size; K is a dimensionless shape factor, with a value close to unity. The shape factor has a typical value of about 0.9, but varies with the actual shape of the crystallite; λ is the X-ray wavelength; β is the line broadening at half the maximum intensity (FWHM), after subtracting the instrumental line broadening, in radians. This quantity is also sometimes denoted as Δ(2θ); θ is the Bragg angle (in degrees).

B.4. X-ray Photoelectron Spectroscopy (XPS)

X-ray photoelectron spectroscopy (XPS) is a surface-sensitive quantitative spectroscopic technique that measures the elemental composition at the parts per thousand range (0.1 at. %), chemical state and electronic state of the elements that are present within the first surface layers of a material. The sample is placed in an ultrahigh vacuum environment and exposed to a low energy, monochromatic x-ray source. The incident x-rays (of energy around 1.5 keV) cause the ejection of electrons from the atoms of the sample (photoelectric effect, Figure B.7).

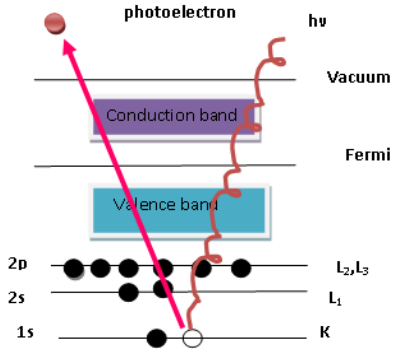

Figure B.7 The photoemission process involved in XPS. The discs represent electrons and the bars represent energy levels within the material being analyzed.

An electron energy analyzer is used to measure the energy of the emitted photoelectrons and a detector to count their number. The number of photoelectrons as a function of their

energy gives the XPS spectrum of the sample. The kinetic energy of the generated photoelectrons is given by:

$$Ke = h\nu - BE - \phi$$

where hν is the incident photon energy, BE the binding energy of the emitted electron in the atom and ϕ is the work function of the analyzed material. The kinetic energy of a photo-emitted electron is a function of its binding energy and thus is characteristic of the element from which it was emitted. For this reason, the energy corresponding to each peak in the XPS spectrum is characteristic of an element present in the sampled volume and can be used for composition analysis. The area under a peak in the spectrum is a measure of the relative amount of the element represented by that peak. The peak shape and precise position indicates the chemical state for the element. XPS is a surface sensitive technique because only those electrons generated near the surface escape without losing energy and are detected. The photoelectrons of interest have relatively low kinetic energy. Due to inelastic collisions within the sample's atomic structure, photoelectrons originating more than 20 to 50 Å below the surface do not contribute to XPS signals.

The X-ray Photoelectron Spectroscopy analyses were performed by using a "Surface spectroscopy facility" at IMEM-CNR[6] of Trento (see Figure B.8). The ultra-high vacuum (UHV) facility for surface spectroscopy is a μ-metal chamber, pumped by a main system constituted by a dry primary pump connected with a magnetic-levitation turbomolecular pump (Edwards STP451 MAGLEV), and equipped with different excitation sources. After the proper bake-out procedure this pumping system assures a base pressure of about $1x10^{-10}$ mbar. The sample holder is a VG XL25 type, made by a sample carrier with an on-board heater and a cooling system (-100/+1200°C temperature range), a thermocouple is present to monitor sample temperature. It is mounted on a 5 degrees of freedom manipulator, which besides assures the correct sample positioning for both surface analysis and film deposition. Moreover, UHV electrical feedthroughs provide electrical contact to bias the sample surface, as well as the needed wiring to resistively heat the sample and measure its temperature. The analysis chamber is connected in UHV with the Fast Entry system that permits the insertion of samples from air to vacuum. The core of the facility is the electron energy analyzer, an hemispherical type (VS WHA100), with a spheres' radius of 100mm. This analyzer acts as a narrow energy pass filter, letting pass only the electrons that have a

[6] Institute of Materials for Electronics and Magnetism (IMEM), National Research Council (CNR),Via alla Cascata 56/C, 38123 (Povo) Trento, Italy.

specific KE, and it is equipped with a five Channel Electron Multipliers (so called Channeltrons) to collect and reveal the electrons. Different surface electron techniques can be performed, namely X-ray and UV Photoelectron spectroscopies (XPS and UPS), Auger electron spectroscopy (AES), electron energy loss spectroscopy (EELS).

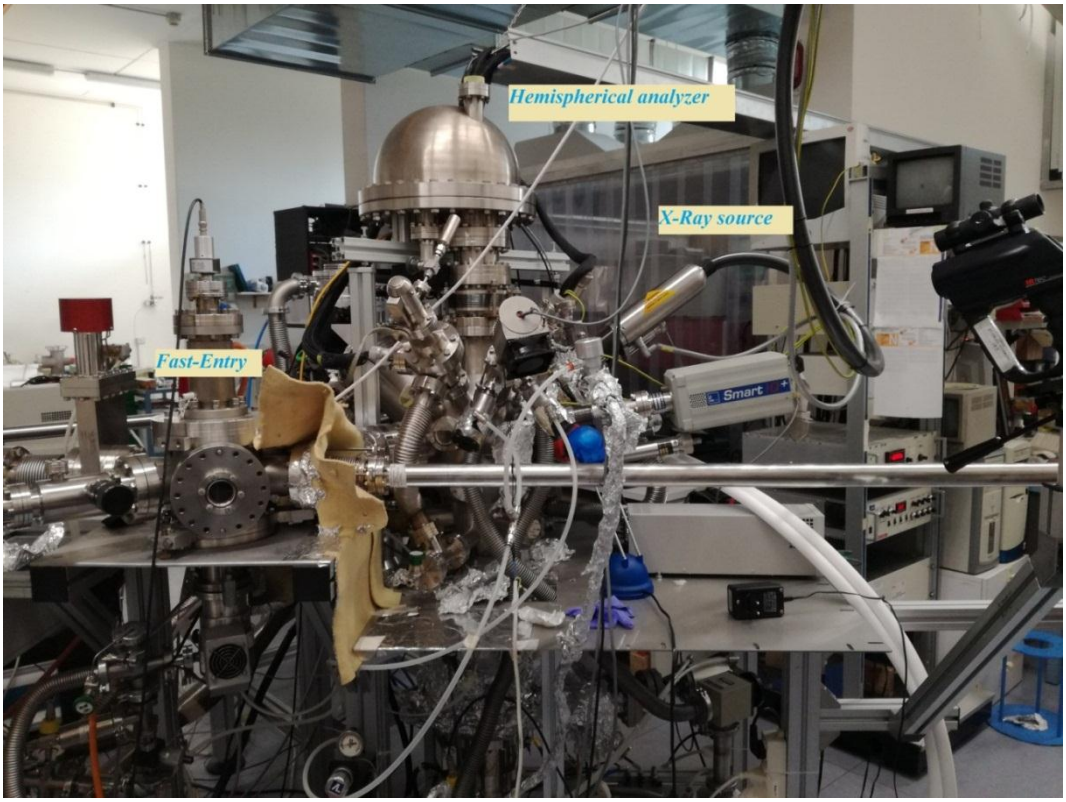

Figure B.8 Surface spectroscopy facility

Using this analyzer, the maximum energy resolution achieved for XPS and UPS techniques is 0.78 and 0.1eV, respectively, while for AES is 0.5eV. The collection geometry is such that the sample surface is typically normal to the analyzer in XPS, UPS and AES spectroscopies, while excitation sources are positioned at different angles with respect to the sample's surface. The chamber is also equipped with a reverse view type LEED (Low Energy Electron Diffraction), provided with an electron beam gun that operates at energies ranging from 10 to 1000eV (typically at 20-200eV), with high brilliance and small spot thanks to the LaB6 electron emitting filament.

X-Rays are produced by a double-anode Mg source, in which the excited emission is the line $K\alpha_{1,2}$ and the emission energy is 1253.6eV (phonon energy width ΔE=0.70eV). The continuum Bremsstrahlung spectrum is filtered by the insertion of a thin (1μm) aluminum

foil in correspondence of the exit aperture, which also acts as shield to the high voltage of the anode for the sample surface.

The electron source (LEG62 ThermoVG electron gun), used as excitation source for AES, has a maximum beam energy of 5keV and a maximum current of 20μA: spot size can be as small as 5μm. The UV source is a home-made He discharge lamp, with two-stages differential pumping employed to minimize gas load in the main chamber. Two UV photons can be produced: HeI ($h\nu = 21.22eV$) and HeII ($h\nu = 40.8eV$).

B.5. UV-Vis spectroscopy (UV-Vis)

UV-visible spectroscopy, also known as electronic spectroscopy, refers to the absorption of electromagnetic radiation by atoms or molecules that leads to valence electrons promotion from ground state to excited states. Generally, the explored range of wavelengths includes UV (10- 200 nm), near UV (200-380 nm) and visible (380-780 nm) light. Sometimes, also the near infrared region (>780 nm) is investigated. To encompass the majority of electron transitions the spectrum between 190 and 900 nm is usually considered. Valence electrons can be found in one of three types of electron orbital:

1. single, or σ, bonding orbitals;
2. double or triple bonds (π bonding orbitals); and
3. non-bonding orbitals (lone pair electrons).

Sigma bonding orbitals tend to be lower in energy than π bonding orbitals, which in turn are lower in energy than non-bonding orbitals. When electromagnetic radiation of the correct frequency is absorbed, a transition occurs from one of these orbitals to an empty orbital, usually an antibonding orbital, σ* or π*. For molecules, electrons are promoted from the highest occupied molecular orbital to the lowest unoccupied molecular orbital. There are different mechanisms of light absorption by semiconductors: interband (fundamental) absorption, dopant absorption, excitonic absorption, absorption by free charge carriers, absorption by crystalline lattice. The fundamental absorption leads to the generation of electron-hole pairs as a result of optical excitation of electrons from the valence band to the conduction band. Since the minimum quantum energy sufficient to electron excitation from the valence band to the conduction band is equal to the band gap, the threshold energy of the fundamental absorption is related to the band gap of the semiconductor.

The amount of absorbed light is expressed as either transmittance (T) or absorbance (A) of the material. Transmittance is given in terms of fraction or percentage and is defined as:

$$T(\lambda) = \frac{I(\lambda)}{Io(\lambda)} \text{ or } \quad \%T = \frac{I}{Io}$$

where I is the intensity of transmitted light and I_0 is the intensity of incident light. Absorbance is defined as:

$$A(\lambda) = -\log T(\lambda)$$

The intensity of the absorbed light follows the Lambert-Beer's law:

$$I(\lambda) = Io(\lambda)\, e^{-a(\lambda)d}$$

where d is the thickness of the sample and $\alpha(\lambda)$ is the absorption coefficient of the material.

A UV-Vis spectrometer (Figure B.9) [3] consists of a light source, a monochromator, a beam splitter, two holders (one for the sample and one for the reference), and two photodiode detectors.

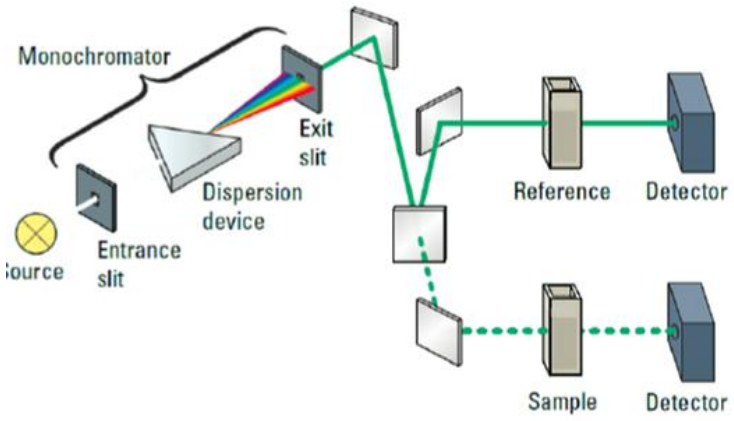

Figure B.9 Schematic optical system of a common double-beam spectrophotometer

The light source should be stable and should provide sufficient intensity over a large region of the electromagnetic spectrum. A combination of tungsten-halogen and deuterium arc bulbs provide visible and UV light, respectively. The monochromator separates the light emitted by the source into its component wavelengths. The beam is separated into two

beams with equal intensity: one beam is used as the reference and the other passes through the sample. The reference beam intensity is taken as 100% Transmission (or 0 Absorbance), and the measurement displayed is the ratio of the two beam intensities.

The absorption properties of the synthesized nanocomposites were studied by using an UV-Visible spectrophotometer "**Perkin Elmer, Lambda 850**" equipped by two lamps: a tungsten lamp for emissions in the visible region covering a range of wavelengths between 930 and 330 nm, and a deuterium lamp (a hydrogen isotope) which emits continuously below 400 nm to 175 nm. The beam from the source is sent to the monochromator, which breaks the polychromatic radiant bands as monochromatic as possible. The radius outgoing from the monochrome is split; the two rays are sent, one in the sample and one in the white. These double-ray spectrophotometers allow you to record the spectrum automatically and to compensate automatically the fluctuations of the lamp. The signal collected by the detector is then sent to the data processing system. The instrument is equipped with a special system for the housing of solid samples (see Figure B.10). This type of housing was particularly suitable for measurements on prepared nanocomposites, as it was possible to place the sample on one side and the matrix film on the other side. In this way it was possible to subtract the matrix's contribution while capturing the spectrum.

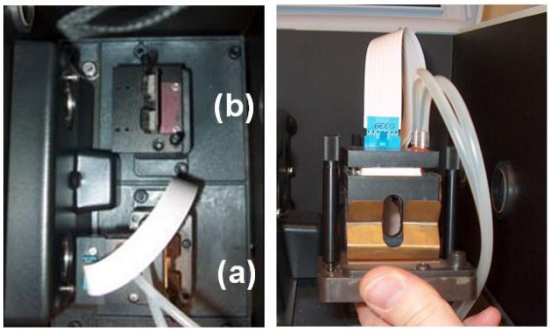

Figure B.10 The housing area: a) sample and b) reference

B.6. Fourier Transform Infrared Spectroscopy (FT-IR)

Fourier Transform-Infrared Spectroscopy (FTIR) is an analytical technique used to identify organic (and in some cases inorganic) materials. This technique measures the absorption of infrared radiation by the sample material versus wavelength. The infrared absorption bands identify molecular components and structures.

When a material is irradiated with infrared radiation, absorbed IR radiation usually excites molecules into a higher vibrational state. The wavelength of light absorbed by a particular

molecule is a function of the energy difference between the at-rest and excited vibrational states. The wavelengths that are absorbed by the sample are characteristic of its molecular structure. The FTIR spectrometer uses an interferometer (see Figure B. 11) to modulate the wavelength from a broadband infrared source.

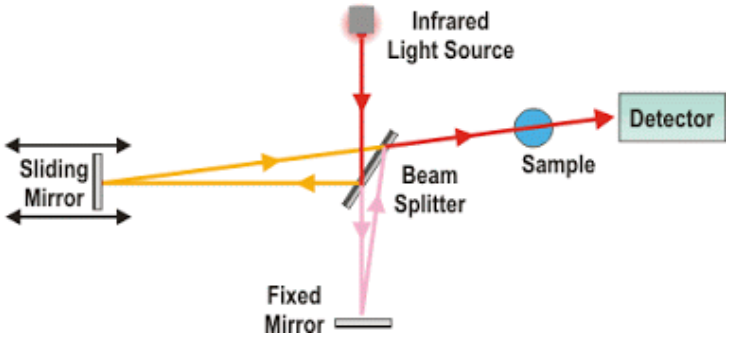

Figure B. 11 A schematic of an interferometer used in a Fourier Transfer Infrared Spectrometer (FTIR).

A detector measures the intensity of transmitting or reflected light as a function of its wavelength. The signal obtained from the detector is an interferogram, which must be analyzed by a computer using Fourier transforms to obtain a single-beam infrared spectrum. The FTIR spectra are usually presented as plots of intensity versus wavenumber (in cm-1). Wavenumber is the reciprocal of the wavelength. The intensity can be plotted as the percentage of light transmittance or absorbance at each wavenumber.

FTIR analyses were carried out at room temperature using a Nexus-Nicolet apparatus, and selecting a wavenumber from 2000 to 600 cm^{-1}. The FTIR spectra were collected in both in absorbance mode on transparent film obtained by dispersing the sample powders in vaseline (2% wt/wt) and spread between sodium chloride (NaCl) windows, commonly used for the FTIR spectroscopy and on thin film in transmittance mode. The samples preparation was done both in glove box under nitrogen atmosphere and in air, while the measurements were performed in air.

B.7. Thermogravimetric analysis (TGA)

Thermogravimetric analysis or thermal gravimetric analysis (TGA) is a method of thermal analysis in which the mass of a sample is measured over time as the temperature changes. This measurement provides information about physical phenomena, such as phase transitions, absorption and desorption; as well as chemical phenomena including chemisorptions, thermal decomposition, and solid-gas reactions (e.g., oxidation or

reduction). Thermogravimetric analysis (TGA) is conducted on an instrument referred to as a thermogravimetric analyzer. A thermogravimetric analyzer continuously measures mass while the temperature of a sample is changed over time. Mass, temperature, and time in thermogravimetric analysis are considered base measurements while many additional measures may be derived from these three base measurements. A typical thermogravimetric analyzer consists of a precision balance with a sample pan located inside a furnace with a programmable control temperature. The temperature is generally increased at constant rate (or for some applications the temperature is controlled for a constant mass loss) to incur a thermal reaction. The thermal reaction may occur under a variety of atmospheres including: ambient air, vacuum, inert gas, oxidizing/reducing gases, corrosive gases, carburizing gases, vapors of liquids or "self-generated atmosphere"; as well as a variety of pressures including: a high vacuum, high pressure, constant pressure, or a controlled pressure. The thermogravimetric data collected from a thermal reaction is compiled into a plot of mass or percentage of initial mass on the y axis versus either temperature or time on the x-axis. This plot, which is often smoothed, is referred to as a TGA curve. The first derivative of the TGA curve (the DTG curve) may plotted to determine inflection points useful for in-depth interpretations as well as differential thermal analysis.

Thermogravimetric analysis were performed by using a "**TGA Q5000, TA INSTRUMENTS**" thermobalance. Typical sample quantities were of about 5–10 mg. The samples were generally analyzed nitrogen atmosphere, in some case also under fluxing air, at rate of 10°C/min.

B.8. References

[1] Z.L. Wang, ed., Characterization of Nanophase Materials, Wiley-VCH Verlag GmbH, Weinheim, FRG, 1999. doi:10.1002/3527600094.

[2] J. Goldstein, D.E. Newbury, P. Echlin, D.C. Joy, A.D.R. Jr., C.E. Lyman, C. Fiori, E. Lifshin, Scanning Electron Microscopy and X-Ray Microanalysis: A Text for Biologists, Materials Scientists, and Geologists, Scanning Electron Microsc. X-Ray Microanal. - A Text Biol. | Springer. (2012) 840. doi:10.1 0071/978-1-4613-0491-3.

[3] T. Owen, Fundamentals of modern UV-Visible spectroscopy,agilent technologies., Germany, 2000.

Acknowledgments

I would like to express my gratitude to Prof. Antonio Miotello and Prof. Luigi Ambrosio, for constantly supporting me during my thesis work.

I would like to express my deepest gratitude to Dr. Carmela Borriello, researcher at ENEA (Centro Ricerche Portici), for giving me the opportunity to complete my thesis work in the ENEA laboratories, and for supporting me continuously both technically and emotionally.

Sincere thanks go to all the people who were involved, directly or indirectly, in my thesis work.

In particular, I would like to express special gratitude to the following people:

Dr. Gianfranco Carotenuto, senior researcher at IPCB-CNR, who followed me especially during the PhD first period. I'm grateful to him for his valuable suggestions and guidance of my research career.

Angela Longo, researcher at IPCB-CNR, with whom I had begun and, at beginning, nicely shared this experience.

Binetti Enrico and Pushkar Patil, ex CNR colleagues, for their advices and for the wonderful moments shared together.

I am grateful to the net of our collaborators from other institutions, which helped to improve the scientific quality of my work. In particular, I express my deepest gratitude to Dr. Lucrezia Aversa, researcher at IMEM-CNR of Trento and Dr. Giuseppe Nicotra researcher at IMM-CNR of Catania, for improving my dissertation thanks to the use of the advanced techniques available at their laboratories, and also for their constant availability.

I heartily thank Dr. Andrea Sorrentino, researcher at IPCB-CNR, for being always close to me, especially in the last period of my thesis work.

I thank Dr. Sergio De Nicola, senior researcher at SPIN-CNR, for his constant encouragement and technical support.

Finally, I would say thanks to:

Nicola Bazzanella, Orlandi Michele, Zakaria El koura and Alberto Mazzi, belonging to IdEA group, for their availability and for the nice time spent together.

I thank Giovanna Pintori and Maria Concetta Tringali, for their constant support and advices, but mainly for their friendship.

Gleniss Ciotola, Alessandra Longo, Matilda Sulmeta and Heshani Jayaratne for all the good times lived together in Trento. You will always be part of my life!

Then I would like to give my special thanks to all the IPCB-CNR and UNITN people, for helping and encouraging me during all the thesis period.

Un grazie dal profondo del cuore:

A mia madre, presenza costante e fondamentale della mia vita.

A mia sorella, per i suoi preziosi consigli. Non ne avrei potuta avere una migliore.

Ai miei nipoti, Daniele e Federica, che amo con tutto il mio cuore e sono per me ragion di vita.

A tutto il resto della mia famiglia che ha condiviso con entusiasmo questa mia esperienza.

A tutti gli amici e le persone con cui ho condiviso questo cammino.

Dedico questa tesi a mio padre, che non è più qui con me.